

A Thesis Submitted for the Degree of PhD at the University of Warwick

Permanent WRAP URL:

<http://wrap.warwick.ac.uk/99925>

Copyright and reuse:

This thesis is made available online and is protected by original copyright.

Please scroll down to view the document itself.

Please refer to the repository record for this item for information to help you to cite it.

Our policy information is available from the repository home page.

For more information, please contact the WRAP Team at: wrap@warwick.ac.uk

THE BRITISH LIBRARY DOCUMENT SUPPLY CENTRE

TITLE

Angle Resolved Collision Induced Decomposition
of Gaseous Ions

AUTHOR

Golin Moore

INSTITUTION
and DATE

University of Warwick 1987

Attention is drawn to the fact that the copyright of
this thesis rests with its author.

This copy of the thesis has been supplied on condition
that anyone who consults it is understood to recognise
that its copyright rests with its author and that no
information derived from it may be published without
the author's prior written consent.

THE BRITISH LIBRARY
DOCUMENT SUPPLY CENTRE
Boston Spa, Wetherby
West Yorkshire
United Kingdom

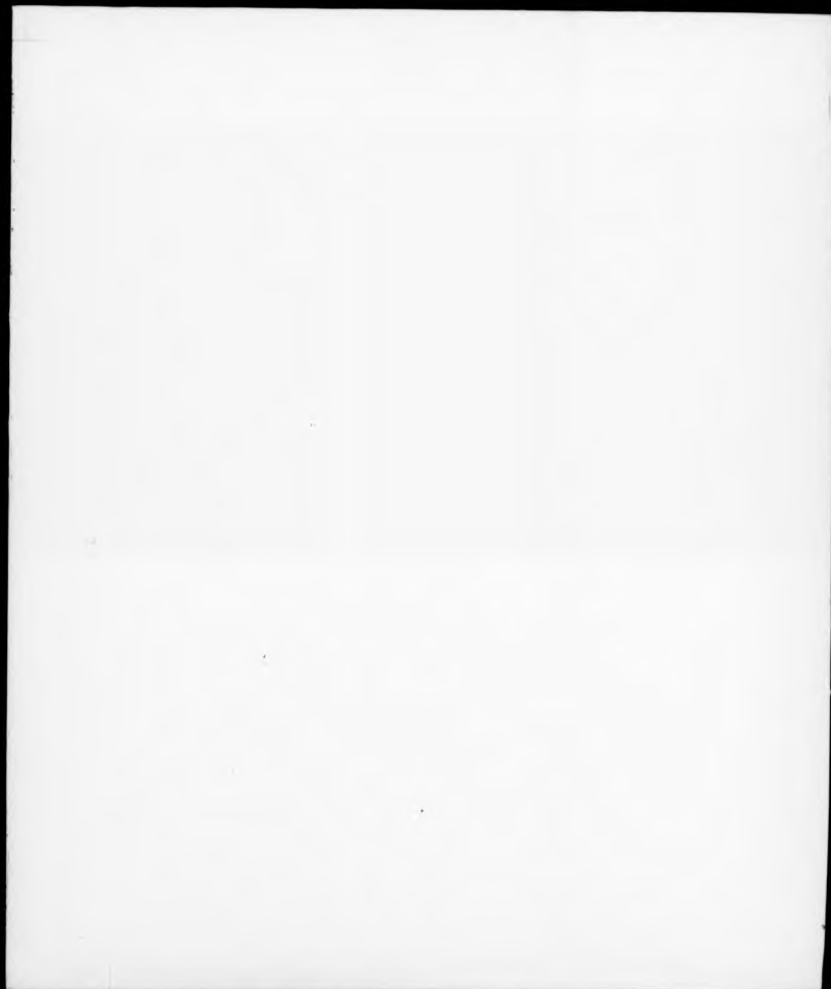
1	2	3	4	5	6
cms					

20

REDUCTION X

CAMERA

5



Angle Resolved Collision Induced Decomposition
of Gaseous Ions

by

Colin Moore

Submitted to the University of Warwick in partial
fulfilment of the degree of Doctor of Philosophy

Department of Chemistry and Molecular Sciences

University of Warwick

Coventry

CV4 7AL

December 1987

To Izzy,
and my parents,
and my sisters.

CONTENTS

	Page No.
Table of contents	iii
Acknowledgements	viii
Declaration	ix
List of Abbreviations	x
List of Figures	xi
List of tables	xxiv
Summary	xxvi
 CHAPTER 1	 GUIDE TO THE THESIS
1.1	Introduction 1
 CHAPTER 2	 GENERAL BACKGROUND
2.1	Introduction 5
2.2	The Mass Spectrometer 6
2.2.1	Ion Formation 6
2.2.2	Ion Separation 7
2.2.3	Ion Detection 11
2.3	Fragment Ions Formed Outside The Ion Source 12
2.3.1	Metastable Ions 12
2.3.2	Collision Induced Decompositions 15
2.4	Angle Resolved Mass Spectrometry 18
2.4.1	Scattering and CID 18
2.4.2	The History Of ARMS Studies 21

CONTENTS

	Page No.
2.4.3 Experimental Methods Of Obtaining ARMS Data	21
2.5 References	26
 CHAPTER 3	
EXPERIMENTAL DETAILS OF THE Z-DEFLECTION METHOD	
 3.1 Introduction	30
3.2 The Collision Chamber	30
3.3 Calculating θ And $\Delta\theta$	32
3.4 Data Collection	36
3.5 References	38
 CHAPTER 4	
RESULTS OBTAINED USING THE Z-DEFLECTION METHOD	
 4.1 Introduction	39
4.2 Collision Gas Pressure	39
4.3 E_{ion} Of The Parent Ions Before Collisional Activation	45
4.4 Parent Ion Lifetime Before Collisional Activation	60
4.5 Conclusions	60
4.6 References	63

CONTENTS

		Page No.
CHAPTER 5	DESCRIPTION OF THE SWINGING SOURCE	
5.1	Introduction	65
5.2	Description Of The Source	65
5.3	Operating Procedure	74
5.4	Initial Results	74
5.5	References	82
CHAPTER 6	RESULTS OBTAINED USING THE SWINGING SOURCE	
6.1	Introduction	84
6.2	Methanol	84
	6.2.1 The 29/31 Fragment Ion Ratio	85
	6.2.2 The Kinetic Energy Release As A Function Of θ	90
	6.2.3 Fragment Ion Abundances As A Function Of Collision Gas Pressure	109
6.3	o & p-Xylenes	117
	6.3.1 Kinetic Energy Release For $M = (N-15)$ As A Function Of θ	117
6.4	Breakdown Curves Of C_6H_{12} Isomers	122
	6.4.1 Cyclohexane	123
	6.4.2 Two Isomeric Pentenes	135
6.5	n-Butylbenzene	

CONTENTS

	Page No.
6.6 Conclusions	139
6.7 References	141
CHAPTER 7 MODIFYING THE SWINGING SOURCE COLLISION CHAMBER	
7.1 Introduction	144
7.2 The Modifications	144
7.3 Initial Results	146
7.4 Conclusions	153
7.5 References	154
CHAPTER 8 RESULTS OBTAINED USING THE MODIFIED SWINGING SOURCE	
8.1 Introduction	155
8.2 I_{in}/I_{out} Ratios	155
8.3 Fragment Ion Ratios	161
8.3.1 n-Butylbenzene	161
8.3.2 Benzyl Methyl Ether	168
8.4 General Conclusions	170
8.5 References	154

CONTENTS

	Page No.
APPENDIX 1	THE CALCULATION OF θ AND $\Delta\theta$
A1.1	Introduction 176
A1.2	Calculation Of θ 176
A1.3	Calculation Of $\Delta\theta$ 180
APPENDIX 2	THE OBSERVATION OF DAUGHTER IONS FORMED IN A FLOATING COLLISION CHAMBER
A2.1	Introduction 184
A2.2	Daughter Ion Coordinates On The BE Plane 184
A2.3	Calculation Of The Kinetic Energy Release 187
A2.4	References 191

Acknowledgements

First and foremost, I should like to thank Professor Keith Jennings for his encouragement, many fruitful discussions and for giving me the freedom to experiment. For his help with the swinging source, I thank Syd Evans from Kratos. I thank my friends in the Department of Chemistry for their encouragement and support, in particular, Martin Farncombe, Tony Parker, Aidan Harrison, Mol Passman, Jim Laramée and Rod Mason. My thanks go to Alex Coburn, Ron Fathers, Eric Burgess and their respective staffs for help with electronics, engineering and glassblowing. Thanks also go to my colleagues at Kratos Ltd., especially, Roger Brown, Roger Gratehead and Alison Ashcroft. Rootes Hall gave me three homes and a wealth of experience, for which I shall always be grateful.

Finally, I acknowledge the financial support of the Science and Engineering Research Council and Kratos Ltd. under the Co-operative Awards in Science and Engineering (CASE) Award scheme. I also thank the Department of Chemistry and Molecular Sciences for financial assistance during my first year of study.

Last, but by no means least, I thank Izzy for proof-reading the thesis and mounting the diagrams.

Declaration

Parts of the work in this thesis have been presented orally or in poster form at the following meetings:

British Mass Spectrometry Society, Thirteenth meeting,
University of Warwick, 1983

British Mass Spectrometry Society, Fourteenth meeting, Heriot-
Watt University, 1984

Tenth International Mass Spectrometry Conference, University
College of Swansea, 1985

British Mass Spectrometry Society, Fifteenth meeting,
University of Sussex, 1986

List of Abbreviations

ARMS	Angle Resolved Mass Spectrometry
b	Impact parameter
B	Magnetic sector field strength
CA	Collisional activation
CEMS	Charge Exchange Mass Spectrometry
CID	Collision Induced Dissociation
E	Electric sector field strength
E _L	Ion translational energy
ε	Energy gained during collisional activation
MS/MS	Mass Spectrometry/Mass Spectrometry
θ	Scattering angle
	Subscript s denotes due to scattering during collisional activation
	Subscript k denotes due to the release of kinetic energy during the fragmentation
T _ε	Kinetic energy release
	Subscript indicates percentage of peak height at which the width of the peak was measured.
V	Accelerating voltage
V _z	z-deflector voltage

List of Figures

Number Page No. Title

- | | | |
|-----|----|---|
| 2.1 | 10 | Diagram of a double focusing mass spectrometer showing how a monoisotopic dual energy ion beam (1) is separated into two energy resolved beams by the ESA (2) which are then focused by the magnet at the collector slit (3). |
| 2.2 | 14 | The relationships between the centre-of-mass and laboratory velocities for an ion m , fragmenting at point θ to give m_2 and m_1 . |
| 2.3 | 19 | Diagrammatic representation of the scattering and subsequent decomposition of an ion. |
| 2.4 | 22 | Block diagrams showing the many types of mass spectrometer which have been used to acquire ARMS data. Where; S is an ion source, E is an ESA, C is a collision chamber, B is a B-slit, M is a magnet, D is a detector, A is an angle-resolving slit, Z is the Z-deflectors and Q is a quadrupole mass filter. |
| 2.5 | 24 | A mass spectrometer with a moveable ion source, angle defining slits and collision chamber. |

List of Figures

Figure Page No. Title

- | | | |
|------|----|--|
| 3.1 | 31 | Cross-sectional view of the ball valve collision chamber which is described in detail in reference 3. |
| 3.2a | 33 | The collision region. |
| 3.2b | 33 | The gas introduction system. |
| 3.3 | 35 | Schematic diagram of the collision chamber, y and z-focus assemblies and the collector slit of the MS50. |
| 3.4 | 37 | Schematic diagram of the slits which alter the angular resolution obtained when using the z-deflection method. |
| 4.1 | 40 | The 91/92 fragment ion ratio of n-butylbenzene as a function of the collision gas (Argon) pressure (P) at θ_{max} . |
| 4.2a | 42 | The ratios of the abundances of the m/z 91 (*) and m/z 92 (O) fragment ions from n-butylbenzene at P=x, relative to P=0 for fragment ions detected when $\theta=0^\circ$. |

List of Figures

Figure Page No. Title

- 4.2b 43 The ratios of the abundances of the m/z 91 (*) and m/z 92 (●) fragment ions from n-butylbenzene at $P=x$, relative to $P=0$. The 91/92 fragment ion ratio (■), calculated using corrected fragment ion abundances (see text) is also plotted as a function of P for fragment ions detected when $\theta=0.1^\circ$.
- 4.2c 44 The ratios of the abundances of the m/z 91 (*) and m/z 92 (●) fragment ions from n-butylbenzene at $P=x$, relative to $P=0$. The 91/92 fragment ion ratio (■), calculated using corrected fragment ion abundances (see text) is also plotted as a function of P for fragment ions detected when $\theta=0.5^\circ$.
- 4.3 46 The 91/92 fragment ion ratio of n-butylbenzene parent ions formed in an electron impact ion source using electrons of 70 (*), 50 (●) and 20eV (▲), as a function of V_w .
- 4.4 48 The 91/92 fragment ion ratio of n-butylbenzene parent ions formed in an electron impact ion source using electrons of 25 (■), 23 (●), 20 (*) and 15eV (○), as a function of V_w .

List of Figures

Figure Page No. Title

- 4.5 53 The 91/92 fragment ion ratio of n-butylbenzene parent ions formed by charge exchange with $(Ar)^{+}$ (*) or $[COS]^{+}$ (●), as a function of V_w .
- 4.6 55 The 91/92 fragment ion ratio of benzyl methyl ether as a function of V_w .
- 4.7 56 The 91/92 fragment ion ratio of benzyl methyl ether parent ions formed in an electron impact ion source using electrons of 70 (*) , 30 (●) and 15eV (○), as a function of V_w .
- 4.8 57 Relative fragment ion abundances of ethyl phenylacetate as a function of V_w , for parent ions formed in an electron impact ion source using electrons of 10 and 30eV.
- 4.9 58 The origin of the M-27 and M-28 fragment ions of ethyl phenylacetate.
- 4.10 61 The 91/92 fragment ion ratio of n-butylbenzene parent ions produced when the ion source repeller voltage is -1.8V (*) or +19V (●) as a function of V_w .

List of Figures

Figure Page No. Title

- 5.1 66 Schematic diagram of the swinging source (not to scale).
- 5.2 68 The abundance of the methanol molecular ion as a function of the collision gas (Argon) pressure.
- 5.3 70 The abundance of the methanol molecular ion as a function of θ in the absence of collision gas. Pre-collision beam divergence set to $\pm 0.13^\circ$ and detector angular acceptance in the xz plane $\pm 0.11^\circ$.
- 5.4 73 The measured beam flag current and MS50 detector signal for different values of the einzel lens voltage.
- 5.5 76 The kinetic energy loss spectrum for Argon ions scattered by Argon atoms obtained when $\theta = 0.9^\circ$.
- 5.6 77 Kinetic energy loss spectra for Ar^+ scattered by Ar for $\theta=0.9^\circ$ and β -slit widths of 15 thou and 5 thou.

List of Figures

Figure Page No. Title

- | | | |
|-----|----|--|
| 5.7 | 78 | The relative intensities of the B A and C V peaks from Ar^+/Ar scattering as a function of θ at post-collision angular resolutions of $\pm 0.11^\circ$ and $\pm 0.06^\circ$. |
| 5.8 | 80 | Relative intensities of the A, B and C peaks for the scattering of Argon ions by Argon atoms as a function of θ . The crosses show the mean ion abundance (four separate measurements) and the bars indicate the maximum and minimum values obtained at each angle. |
| 5.9 | 81 | Two sets of data showing the variation in the relative abundances of the m/z 29 and m/z 31 fragment ions from methanol as a function of θ . |
| 6.1 | 86 | The 29/31 fragment ion ratio of methanol (R) as a function of θ° at two different ion translational energies (E_t). For θ E_t is 7kV and for \times E_t is 6.146kV. |

List of Figures

Figure Page No. Title

- 6.2a 87 The 29/31 fragment ion ratio of methanol (R) as a function of $E_0\theta$ at two different ion translational energies (E_t). For θ E_t is 7kV and for π E_t is 6.146kV.
- 6.2b 88 The 29/31 fragment ion ratio of methanol (R) as a function of $(E_0\theta)^2$ at two different ion translational energies (E_t). For θ E_t is 7kV and for π E_t is 6.146kV.
- 6.3 91 The thermochemistry of an ion's dissociation.
- 6.4 93 T_{90} as a function of θ for; $[\text{CH}_3\text{OH}]^+ \rightarrow [\text{CH}_3\text{OH}]^+ + \text{H}$
- 6.5 95 The relative abundances of the m/z 31 & m/z 29 fragment ions of methanol as a function of θ .
- 6.6 96 The relationship between the centre-of-mass scattering angle due to kinetic energy release (α) and the laboratory angle (θ_{lab}) shown diagrammatically and mathematically.
- 6.7 100 T_{90} as a function of θ for; $[\text{CH}_3\text{OH}]^+ \rightarrow [\text{HCO}]^+ + \text{H} + \text{H}_2$.

List of Figures

Figure Page No. Title

- 6.8 103 T_{base}/T_{90} and T_{22}/T_{90} as a function of θ for m/z 32 + m/z 31 (x) and m/z 32 + 29 (o) from methanol.
- 6.9 105 The shape of the fragment ion peak for m/z 31 + m/z 29 for methanol at $\theta = 0^\circ$ obtained by scanning the source voltage (V).
- 6.10 106 T_{90} as a function of θ for $[CH_3OH]^{+ \cdot} \rightarrow [HCO]^+ + H_2$.
- 6.11 107 T_{base}/T_{90} and T_{22}/T_{90} as a function of θ for $[CH_3OH]^{+ \cdot} \rightarrow [HCO]^+ + H_2$.
- 6.12 108 T_{base} , T_{22} and T_{90} as a function of θ for the unimolecular reaction: $[CH_3OH]^{+ \cdot} \rightarrow [HCO]^+ + H_2$.
- 6.13 110 Schematic diagram of the swinging source at an angle θ , showing how fragment ions produced by parent ions decomposing along XA will not be detected if $\alpha = 0^\circ$.
- 6.14 112 The \log_{10} of the abundance of the methanol molecular ion as a function of collision gas pressure at two different values of θ .

List of Figures

Figure Page No. Title

- 6.15 113 The \log_{10} of the abundance of m/z 32 = m/z 31 from methanol as a function of collision gas pressure at two different values of θ .
- 6.16 114 The \log_{10} of the abundance of m/z 32 = m/z 29 from methanol as a function of collision gas pressure at two different values of θ .
- 6.17 115 The \log_{10} of the abundance of m/z 31 = m/z 29 from methanol as a function of collision gas pressure at two different values of θ .
- 6.18 119 T_{10} for the fragment ion formed by loss of methyl from the molecular ions of ortho- (x) and para- (o) xylene as a function of θ .
- 6.19 121 The m^*/CID ratio for methyl loss from the molecular ion of p-xylene as a function of θ .
- 6.20 124 ARMS spectra at 0° and 0.53° compared to CEMS data obtained using internal energies of 3 and 5 eV.
- 6.21 125 Fragment ion abundances of cyclohexane as a function of θ .

List of Figures

Figure Page No. Title

- 6.22 129 θ_{max} as a function of T for a parent ion of mass 100 mass units losing 43, 29 and 15 mass units.
- 6.23 130 θ_{max} as a function of daughter ion mass for a parent ion of mass 100 mass units with T fixed at 10meV and 50meV.
- 6.24 131 T_{so} as a function of θ for three fragment ions from cyclohexane.
- 6.25 132 T_{so} as a function of θ for three more fragment ions from cyclohexane.
- 6.26 133 Corrected (as described in the text) fragment ion abundances of cyclohexane as a function of θ .
- 6.27 137 T_{so} as a function of θ for $[\text{C}_{10}\text{H}_{14}]^+ \rightarrow [\text{C}_7\text{H}_7]^+ + \text{C}_3\text{H}_7^+$. For parent ions produced either in a 'hot' source or a 'cold' source.
- 7.1 145 Schematic diagrams of the mounting of the swinging source collision chamber, modified so that a potential can be applied to it.

List of Figures

Figure Page No. Title

- 7.2a 147 The intensity of the 'B' peak as a percentage of (A+B+C+D) for Ar⁺ scattered by Argon atoms as a function of θ . The source and collision chamber voltages are given in Table 7.1.
- 7.2b 148 As Figure 7.2a, but for the 'C' peak.
- 7.3 152 T_{90} for propyl loss from n-butylbenzene molecular ions as a function of θ . Data obtained with the collision chamber either at ground potential ϕ or at a potential of -500V.
- 8.1 156 The abundance of m/z 31 as a function of Ar collision gas pressure when $\theta=0^\circ$ and $\theta=0.53^\circ$ for fragment ions produced inside ϕ and outside κ of the cell. $\{I_{i,n}/I_{m,n}\}$.
- 8.2 158 The abundance of m/z 29 as a function of He collision gas pressure when $\theta=0^\circ$ and $\theta=0.53^\circ$ for fragment ions produced inside ϕ and outside κ of the cell. $\{I_{i,n}/I_{m,n}\}$.
- 8.3 160 The abundance of m/z 69 as a function of Ar collision gas pressure when $\theta=0^\circ$ and $\theta=0.27^\circ$ for fragment ions produced inside ϕ and outside κ of the cell. $\{I_{i,n}/I_{m,n}\}$.

List of Figures

Figure Page No. Title

- | | | |
|-----|-----|---|
| 8.4 | 163 | The 91/92 ratio for n-butylbenzene as a function of θ . Total fragment ion abundance data from the swinging source compared with data from reference 12. |
| 8.5 | 164 | The 91/92 ratio for n-butylbenzene as a function of θ . Ratios calculated from total fragment ion abundance data from the swinging source compared with fragment ion abundance ratios from inside the collision chamber θ . |
| 8.6 | 165 | The CID/ m^+ ratios of two n-butylbenzene fragment ions as a function of θ . |
| 8.7 | 167 | The 91/92 ratio for n-butylbenzene as a function of θ . Ratios calculated from CID only fragment ion abundance data from the swinging source compared with ratios from reference 16. |
| 8.8 | 169 | The 91/92 ratio for benzyl methyl ether as a function of θ . Ratios calculated from total fragment ion abundance data from the swinging source compared with CID only ion abundance ratios. |

List of Figures

Figure Page No. Title

- | | | |
|-------|-----|--|
| 8.9 | 172 | Theoretical rate constants k as a function of parent ion internal energy E for two hypothetical reactions of parent ion M^+ giving fragment ions A^+ and B^+ . |
| I. 1a | 177 | Schematic diagram of the source when $\theta=0^\circ$. |
| I. 1b | 177 | Schematic diagram of the source when $\theta \neq 0^\circ$. |
| I. 2 | 181 | The linear relationship between x (the micrometer setting) and θ . |
| I. 3 | 183 | Two slits of length AB and CD , separated by the distance XY will transmit an ion beam having a divergence half-angle of α . |

List of Tables

Table Page No. Title

4.1	47	Comparing 91/92 ratios obtained from photoexcitation experiments with collisional activation of molecular ions ionised by electrons of different energies.
4.2	49	The m^+ 91/92 ratio of n-butylbenzene molecular ions ionised by electrons of energies 70, 15, 13 & 11eV.
4.3	54	The origin of four of the fragment ions of ethyl phenylacetate.
5.1	69	Changes in the pre-collision beam divergence with the z-restrictor length.
5.2	69	The angular acceptance of the detector at various source and collector slit lengths.
6.1	89	Values of θ at which the 29/31 fragment ion ratio of methanol is unity obtained by various groups on different designs of mass spectrometer.
6.2	98	θ_{max} as a function of T_{so} , for m/z 32 & 31 in methanol

List of Tables

Table	Page No.	Title
6.3	99	θ_{max} as a function of T_{ion} , for m/z 32 = 29 in methanol
6.4	101	The variation in the ratio of the kinetic energy releases for m/z 32 = 31 and 32 = 29 as a function of θ
6.5	126	Comparison of fragment ion abundance crossover points in CEMS and ARMS results.
6.6	134	T_{ion} and θ_{max} for the major fragment ions of cyclohexene at different values of θ .
6.7	135	Fragment ion ratios at three values of θ .
7.1	146	Source and collision chamber voltages used when acquiring the data in Figure 7.2
8.1	170	E_{ion} values obtained by comparing 91/92 ratios in ARMS data with CEMS data.
1.1	180	The micrometer reading x needed to give θ values between 0 and 1.5° in increments of 0.1°.
1.2	182	The possible lengths of the apertures which alter the size of the ion beam in the xz plane.

Summary

This thesis describes a series of experiments undertaken to collect Angle Resolved Mass Spectra (ARMS) in order to investigate the scattering of ions during collisional activation. In particular, data were obtained to see if the angle resolved mass spectra of the scattered ions could be explained by assuming that the scattering angle θ was directly related to the energy gained by the ions during collisional activation.

Initially data were obtained on a slightly modified commercially available mass spectrometer using the z-deflection method. The inherently poor angular resolution of this method limited the scope of these experiments to an investigation of the effect of experimental variables on ARMS data.

To overcome the problems of the z-deflection method a swinging source was designed and fitted to the mass spectrometer. The major advantages of this source were that θ was selected mechanically and that the pre- and post-collision angular resolutions of the experiments could be varied, but were independent of the masses of the ions. Using the source, data similar to those published by other groups were obtained. Interpreting these data, however, was difficult because fragment ion abundances contained contributions from decompositions occurring outside the collision chamber. A modification was made to the source which enabled these ions to be excluded from the data and the effect of this modification on the ARMS spectra obtained is discussed.

CHAPTER 1

1.1 INTRODUCTION

ARMS is the acronym for Angle Resolved Mass Spectrometry which may be simply defined as the study of ions scattered during collisional activation as a function of the observed scattering angle θ . The mass spectra of the scattered ions vary with θ in such a way that the internal energy gained by the ion during CA appears to depend upon θ . This has meant that ARMS has been seen as either a means of studying the mechanism of collisional activation or as a way of investigating the behaviour of ions as a function of their internal energy.

In Chapter 2 of this thesis, the theory underlying the operation of a mass spectrometer is described and the advantages of studying ions which decompose outside the ion source are stated. Finally, a history of ARMS studies and a description of the experimental methods used to acquire these data are given. The implementation of the 'z-deflection' method on an MS50 and the improved collision gas introduction system which the method required are described in Chapter 3. This method, although it has the advantage that it does not require the user to modify the spectrometer, suffers from limited angular resolution which depends upon θ . It is also difficult to relate the z-deflector voltage V_z to θ . For these reasons the method was not used to try to determine exactly the variation in a fragment ion's abundance with θ , but the influence of some of the many experimental variables on ARMS was investigated. One such variable is the internal energy of the parent ion before collisional activation. This was changed using one of the following techniques;

CHAPTER 1

- 1) Varying the energy of the electrons ionising the compounds.
- 2) Preparing molecular ions by charge exchange ionisation in a 'high' pressure source.
- 3) By varying the residence time of the ion in the ion source with the repeller voltage.

The energy gained during collisional activation was altered by changing the collision gas pressure and/or θ . These data are discussed in Chapter 4. While the z-deflection method was being used to obtain ARMS data, a special 'swinging' source was under construction. It was designed so that the selection of θ and $\Delta\theta$ (the range of scattering angles detected at a particular angle) is entirely mechanical and therefore precisely known and easily repeated. The calculation of θ and $\Delta\theta$ for the swinging source is explained in Appendix I. In Chapter 5, the source is described in detail and preliminary results are compared with those reported by other researchers. In Chapter 6, ARMS data for methanol, ortho- and para-xylenes, three C_6H_{10} isomers and n-butylbenzene are discussed. The methanol data were obtained in an attempt to provide answers to the following questions;

- 1) What is the relationship between the energy gained during CA at a given value of θ and the translational energy of the ion before CA (E_u) ?
- 2) Why does changing θ cause the kinetic energy released when an ion fragments to alter and can this be related to changes in the relative abundances of fragment ions ?
- 3) What does the pressure dependence of a fragment ion's abundance as a function of θ tell us about the importance of

CHAPTER 1

scattering to ARMS ?

The possible use of ARMS as an alternative to photoexcitation is investigated by attempting to distinguish between ortho- and para-xylene from measurements of T_{10} as a function of θ instead of as a function of photon energy. The ARMS data on three C_6H_{12} isomers are essentially those of two separate studies: (i) a detailed comparison of breakdown curves for cyclohexane generated from Charge Exchange Mass Spectrometry (CEMS) data with those produced from ARMS data, and (ii) a more limited comparison of CEMS and ARMS data on 2-methyl-1-pentene and 2-methyl-2-pentene. Finally in Chapter 6, the influence of the ion source temperature on the angular dependence of T_{10} for propyl loss from the molecular ion of n-butylbenzene is discussed.

By definition ARMS results should not include contributions from fragment ions which are not formed inside the collision chamber. This can easily be achieved if the collision chamber is not at ground potential but has a small voltage applied to it. The modification of the swinging source to accomplish this is described in Chapter 7. The effect of this voltage on the operation of the swinging source is discussed using data on the scattering of argon ions by argon atoms and the CID of n-butylbenzene. The voltage also affects the measurement of T values and the values of B (the magnetic field strength) and E (the electric sector field strength) at which a fragment ion is detected; this is discussed in Appendix II. In Chapter 8 fragment ion abundances inside (I_{in}) and outside (I_{out}) the cell are reported as a function of θ for methanol, n-butylbenzene and

CHAPTER I

benzyl methyl ether. Fragment ion ratios calculated purely from I_{rel} data are compared to published data and the usefulness of these data is questioned.

CHAPTER 2

2.1 INTRODUCTION

The mass spectrum of a compound is a plot of the abundance of the ions normalised to the abundance of the most intense ion as a function of its mass to charge ratio. In its most easily interpreted form the spectrum contains a peak due to a molecular ion formed by direct ionisation of sample molecules which gives the relative molecular mass of the compound. Fragment ions with masses less than that of the molecular ion are formed in competing consecutive unimolecular reactions within the ion source and are important because they give structural information. The entire spectrum is characteristic of a particular molecule and can therefore be compared to entries in a library of mass spectra for quick identification of the spectra of unknown samples. Problems arise when the unknown sample is not a single compound but a mixture of one or more components, since it is difficult to determine which peaks should be ascribed to molecular ions and which fragment ion is derived from a particular parent ion. For such cases it has become common to use techniques such as gas chromatography (GC) (1) or high performance liquid chromatography (HPLC) (2) to separate the mixture prior to mass spectral analysis. By direct coupling of these techniques to the mass spectrometer the total analysis time can be reduced in effect to the time necessary for chromatographic separation of the components since complete mass spectra of the individual components can then be acquired many times a second. Even shorter analysis times are possible if the whole mixture is ionised simultaneously and then the mass spectra of the collision-

CHAPTER 2

induced product ions from selected precursor ions are obtained using tandem mass spectrometry (3). Collisional activation of the precursor ion is usually affected by using a collision gas such as helium and because scattering of the parent and daughter ions occurs, the relative abundances of these ions vary with the observed scattering angle θ .

2.2 THE MASS SPECTROMETER

A basic mass spectrometer consists of an ionisation chamber, a means of separating ions according to their mass to charge ratios and an ion detector.

2.2.1 ION FORMATION

Ionisation of gas phase sample molecules is usually affected by bombardment with electrons of 70eV energy (electron ionisation EI), produced by electrically heating a metal filament. As approximately 15 to 20eV energy is usually transferred to the sample molecules upon ionisation, which is large when compared to the typical ionisation energy of an organic molecule, e.g. 10eV, the molecular ion is formed with a large excess of energy and will therefore fragment to give characteristic fragment ions (4). Indeed, for some molecules fragmentation is such a facile process that a molecular ion is not observed in the EI mass spectrum. This has led to the development of 'softer' ionisation techniques such as chemical ionisation (CI) (5), field desorption (FD) (6,7) and fast atom bombardment (FAB) (8,9).

The ion source of a high resolution mass spectrometer is held at

CHAPTER 2

a potential V and therefore ions accelerate upon leaving the source to a velocity v_0 , such that;

$$zeV = \frac{m_i(v_0)^2}{2} \quad (1)$$

where z is the number of charges on the ion and m_i is its mass.

2.2.2 ION SEPARATION

Separation of a beam of ions of differing mass to charge ratios can be accomplished using a magnetic field because ions passing through such a field experience a force perpendicular to the field and to the initial direction of motion of the ions. If r_b is the radius of the ions' path through a magnetic field of strength B , then:

$$r_b = \frac{m_i v_0}{Bez} \quad (2)$$

The magnetic sector, besides being able to separate ions of different mass to charge ratios, will bring an angularly divergent ion beam to a focus at a single point (10), i.e. it is direction-focusing. It follows, however, from equation 2, that its ability to separate ions having different mass to charge ratios, depends upon all ions of the same mass having the same velocity, v_0 . When designing a magnetic sector mass spectrometer the resolving power of the instrument i.e. its ability to separate an ion of mass M from $(M+\Delta M)$, is a very important parameter. The factors which determine the resolution of the sector are:

- 1) The radius of the ions' path, r_b .
- 2) Aberrations in the ion optical system.

CHAPTER 2

3) The dimensions of the slits immediately before and after the sector.

4) The energy spread of the ion beam.

Both 1 & 2 are intrinsic properties of the spectrometer and, therefore, are not easily changed. Closing down slits (point 3) does improve resolution, but at the expense of sensitivity. The energy spread of the ion beam can, however, be reduced by placing an electric sector between the ion source and the magnetic sector, or between the magnetic sector and the detector. An electric sector consists of two sector-shaped coaxial cylindrical electrodes which have equal but opposite potentials on them. Ions travelling through such a sector experience a centripetal acceleration dependent upon their kinetic energy. All ions having the same kinetic energy will be brought to focus at the same point, irrespective of their mass. Ions having more or less kinetic energy have different focal points and can therefore be prevented from entering the magnetic sector by a slit. The radius of the electric sector r_e is related to the ion source voltage and the field strength between the electric sector plates E by:

$$r_e = \frac{2V}{E} \quad (3)$$

The combination of electric and magnetic sectors to give a double focusing mass spectrometer capable of high resolution with good sensitivity, is possible because the electric sector focuses ions having different velocities on a plane orthogonal to the ions' direction of motion. As long as all the ions focused on this

CHAPTER 2

plane have the same mass they will also be brought to a focus by the magnetic sector at the detector (see Figure 2.1). The instrument used for this work was a double focusing mass spectrometer of Nier-Johnson (11) geometry and therefore the electric sector preceded the magnetic sector. It is also possible to build double focusing mass spectrometers where the magnetic sector precedes the electric sector and these so-called reverse geometry spectrometers have a number of advantages for MS-MS studies.

Combining equations 1 to 3 above, gives the following equation to describe the effect of B and V on singly charged ions formed in the ion source:

$$\frac{m}{e} = \frac{(Br_m)^2}{2V} \quad (4)$$

To bring ions of different mass-to-charge ratios to a focus at the detector B is scanned while V and r_m are held constant.

A number of other mass-analysers have been developed for use in mass spectrometers the most popular for low resolution mass spectrometers being the quadrupole mass filter (12). This is used in conjunction with an ion source at a low potential and consists of two opposite pairs of cylindrical or hyperbolic rods. The rods have on them d.c. and r.f. potentials, the magnitude of which determine the range of masses of ions that can pass from one end of the rods to the other in a stable cyclic trajectory. The main advantages of the quadrupole mass spectrometer compared with magnetic sector machines are that it is robust, can scan very quickly and is well suited to computerisation. Limited

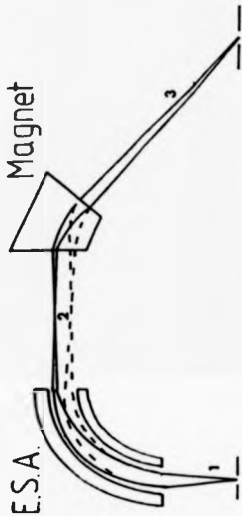


Figure 2.1 Diagram of a double focusing mass spectrometer showing how a monoisotopic dual energy ion beam (1) is separated into two energy resolved beams by the ESA (2) which are then focused by the magnet at the collector slit (3).

CHAPTER 2

resolution and mass range, however, are its most serious disadvantages.

Another means of determining the mass of an ion is to measure the time it takes to travel from the ion source to the detector. All ions accelerated from an ion source have the same kinetic energy, but only ions of the same mass-to-charge ratio have the same velocity and will therefore reach the detector at the same time. The time-of-flight mass spectrometer (13) has a very large mass range but limited resolution.

Finally, the Ion Cyclotron Resonance spectrometer (14) has been shown to be capable of very high resolution i.e. $> 10^6$. An ion will absorb energy from an radio-frequency (r.f.) electric field perpendicular to a magnetic field (B) when its frequency is equal to the cyclotron frequency of the ion (ω). Since $\omega = eB/m$, a mass spectrum can be produced by measuring the r.f. absorbance while scanning B. The development of this analyser has been accelerated by the availability of powerful computers and Fourier transform techniques.

2.2.3 ION DETECTION

The most common form of ion detector in mass spectrometers is the electron multiplier. Positive ions impinging on a curved electrode held at a negative potential initiate the emission of a number of electrons which strike a second electrode and cause more electrons to be emitted. In this way the small current produced by the ions impinging on the first dynode can be amplified to a million times its original value. One

CHAPTER 2

disadvantage of the electron multiplier is that its output depends upon the kinetic energy of the ion and this is particularly important when considering MS-MS data. An alternative detector which is much less sensitive to the ions' kinetic energies is the photomultiplier. Ions hit a scintillator plate which emits photons and these then cause a cascade of electrons to be detected. Such a detector was used in this study.

2.3 FRAGMENT IONS FORMED OUTSIDE THE ION SOURCE

It takes an ion of mass 100 daltons approximately fifteen microseconds to reach the detector of an MS-50 when the ion source is at a potential of 8kV. Ions which leave the ion source without fragmenting have internal energies which depend upon the magnitude of $AE_i - IE$, where AE_i is the appearance energy of the lowest energy fragment ion and IE is the ionisation energy of the molecule. Typically this internal energy range is between 0.1 and 1eV (4) and therefore there is a finite probability that the ion may fragment before reaching the detector. Those ions which do undergo unimolecular fragmentation before reaching the detector are known as metastable ions.

2.3.1 METASTABLE IONS

A double-focusing forward geometry mass spectrometer such as the MS50, has three field free regions (F.F.R). The first of these is between the ion source and ESA, the second is between the ESA and the magnet and the third is between the magnet and detector. Daughter ions produced by metastable ions in the

CHAPTER 2

second F.F.R. are seen in a normal magnet scan as broad peaks at non-integral masses and their existence was first correctly explained by Hipple and Condon (15) in 1946. If the mass of the parent ion is m_1 and the daughter ion mass is m_2 , then the apparent mass of the daughter ion m^* can be calculated using equation 5.

$$m^* = \frac{(m_2)^2}{m_1} \quad (5)$$

It follows directly from this that the observation of a metastable ion can be used to identify daughter-parent ion pairs in the normal mass spectrum which assists in the interpretation of the spectrum. The peaks are broad because some of the excess internal energy of the metastable ion is released as translational energy of the ionic and neutral fragments and therefore fragment ions of the same mass have a range of momenta. Although the magnitude of the kinetic energy release is usually less than 1 eV, it occurs in the centre-of-mass coordinate system, whereas the fragment ions are observed in the laboratory coordinate system (Figure 2.2). When converting between the two systems there is an amplification factor A which for singly charged ions is given by (16);

$$A = \left| \frac{eV}{T} \right|^{1/2} \frac{(m_2(m_2 - m_1))^{1/2}}{m_1} \quad (6)$$

As A is inversely proportional to T, peak broadening caused by very small releases of translational energy can be measured very accurately.

Fragment ions produced by unimolecular dissociation of metastable ions are also formed in the first F.F.R., but these will only be

CHAPTER 2

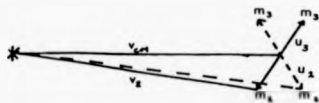


Figure 2.2 The relationships between the centre-of-mass and laboratory velocities for an ion m , fragmenting at point $*$ to give m_2 and m_3 . Where;

v_{cm} is the centre-of-mass velocity of m .

u_2 and u_3 are the centre-of-mass velocities of m_2 and m_3 .

v_1 is the laboratory velocity of m_1 .

CHAPTER 2

detected if both E (the electric sector voltage) and B are scanned. Depending upon the exact relationship between E and B (17), the resulting mass spectrum can contain;

- 1) All the daughter ions from a given parent ion, $B/E = \text{const.}$
- or 2) All the parent ions which fragment to give a particular daughter ion, $B^2/E = \text{const.}$
- or 3) All ions which fragment by loss of a constant neutral fragment, $(B^2/E)(E_0/E) - 1 = \text{const.}$

The information which can be gained from these scans is extremely useful when one is trying to identify an unknown sample and increasing the internal energy of 'stable' ions so that they will fragment in a F.F.R. is therefore highly desirable in structural studies. A number of different methods of activating ions have been reported including photoexcitation (18), irradiation with electrons (19), collisions with a metal surface (20) and collisions with an inert gas (21).

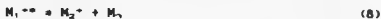
2.3.2 COLLISION INDUCED DECOMPOSITIONS

The collision induced decomposition (CID) of an ion may be split into two distinct stages, collisional activation (CA) followed by unimolecular dissociation of the activated ion. When an ion having a high translational energy (a few hundred eV or more) collides with a stationary gas molecule some of the ion's translational energy is converted into internal energy and the loss in translational energy ΔE_t is approximately equal to the endothermicity Q of the activation step. The process is usually represented by the following equation:

CHAPTER 2



Unimolecular dissociation of the excited ion to a daughter ion and neutral will then occur, provided that the ion has gained enough internal energy during activation i.e.



It is expected that there will be some correlation between the activation energy for reaction 8 when it occurs in the ion source i.e. AP-IP, with Q, and this has been found to be so (22). The introduction of a collision gas into the F.F.R. of a mass spectrometer not only causes reactions 7 and 8 to occur but also a number of competing reactions, as shown below.



Reactions 9 and 10 are examples of charge stripping reactions (23) and Q for these reactions is large, typically 20 - 30 eV and therefore the reaction cross sections are smaller than for CID. Charge exchange (24) (reaction 11) becomes more competitive with

CHAPTER 2

CID if the collision gas is changed to one having a lower IP and therefore because He has a high IP it is frequently used as a collision gas. Finally, reaction 12 (25), represents scattering of ions such that they are excluded from entry into the mass analyser of the mass spectrometer by the slit assemblies. These ions may also undergo one of the other reactions but the product ions will not be detected.

Collisional activation is a particularly useful tool in structural studies since the resulting spectra are very similar to the EI spectra of the same ion. This analytical potential of the technique was first noted by Jennings (21) and developed further by McLafferty with numerous co-workers in a series of studies (26,27).

One drawback of CA is that, unlike e.g. photoexcitation, the exact energy deposited is not known or easily changed. This is not to say that the degree of excitation is not affected by the collision gas (28), the translational energy of the ion (26) and the collision gas pressure (29), but altering these variables does not allow one to study CID as a continuous function of ϵ .

The energy gained during CA of an ion (ϵ) increases if the impact parameter b decreases. Although b is not experimentally accessible, it does affect the scattering angle of the ion θ , and therefore if fragment ion abundances are measured as a function of their observed scattering angle θ , it may be possible to study CA spectra as a function of b and ϵ . These ideas are the cornerstone upon which angle resolved mass spectrometry (ARMS) is founded.

CHAPTER 2

2.4 ANGLE RESOLVED MASS SPECTROMETRY

2.4.1 SCATTERING AND CID

Figure 2.3 is a cross-sectional view of the scattering of an ion and its subsequent unimolecular dissociation. It describes a special case of this type of process since the scattering event and the kinetic energy released upon dissociation of the activated ion both act to deflect the ion in the same plane and are additive. In reality, isotropic dissociation of the ion will produce a conical distribution of fragment ions for each value of θ_0 . For a monatomic ion and target it has been proven (30) that under some conditions the reduced scattering angle τ ($\tau = E_0 = \theta_0$) is a function of b . As b is reduced θ_0 and τ both increase and therefore if θ_0 is zero, θ and τ are directly related to each other. Obviously if θ_0 is $\neq \theta_0$, then this relationship will not be apparent in experimental data which simply gives fragment ion abundances as a function of θ . Note also that the relationship between τ and b has not been proven for polyatomic ions and monatomic targets.

In Figure 2.3 activation and dissociation are shown as two separate events and this separation is easily justified for high energy CID. If one assumes an ion-target interaction distance of 20\AA , then fragmentation must occur when the ion and target are separated by at least this distance. The fastest fragmentation reactions occur in 10^{-14} sec (one bond vibration) and therefore the ion must travel 20\AA in 10^{-14} sec i.e. a centre-of-mass velocity of 2×10^7 cm sec $^{-1}$ or greater is required. As the ions'

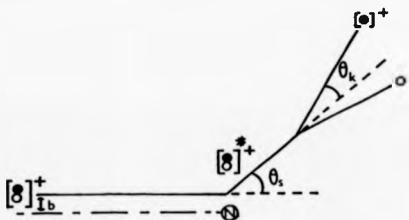


Figure 2.3 Diagrammatic representation of the scattering and subsequent decomposition of an ion. Where;

b is the impact parameter.

θ_s is the laboratory scattering angle.

θ_k is the angle of deflection due to kinetic energy release.

CHAPTER 2

mass is usually α than that of the target, this translates into a velocity in the laboratory system of 2×10^7 cm sec $^{-1}$ or less. Since an ion of mass 100 daltons is accelerated to a velocity of just over 10^7 cm sec $^{-1}$ after leaving an ion source at a potential of 8kV, the separation of activation and dissociation into two independent reactions is shown to be valid for high kinetic energy ions and thermal energy targets.

2.4.2 THE HISTORY OF ARMS STUDIES

The earliest ARMS data obtained on commercially available spectrometers were concerned with the non-dissociative scattering of ions by gas molecules (31,32). The spectrometers were initially used without modification and therefore had limited angular resolution. It was soon found however that the addition of angle resolving slits greatly improved the quality of these data (33). The study of CID as a function of θ was pioneered by Cooks with various co-workers, who suggested that because of the relationship between α and θ , ARMS could be used to produce breakdown curves (34). Later papers from his group and others have tried to show that ARMS can be used for;

- 1) The study of the mechanism of CID.
 - a) Collision gas effects (25,26).
 - b) Changes in CID spectra with the kinetic energy of the ion (35).
- 2) Isomer differentiation by the study of an ions' fragmentation pattern as a function of its internal energy. Giving comparable data to that obtained from;

CHAPTER 2

- a) Breakdown curves (34).
- b) Field ionisation kinetics (36).
- c) Charge exchange mass spectrometry (37,38).
- d) Photoexcitation (39 & 44).
- e) Low energy collisional activation (45).

For all these data it is assumed that θ is made up almost entirely of θ_+ with only a very small contribution, if any, from θ_- . The alternative view that θ is determined by θ_- with only a small contribution from θ_+ was first suggested by Todd et al. (46) in a paper in which calculated fragment ion abundances as a function of θ from kinetic energy release data were compared with published experimental data. The uncertainty surrounding the relative importance of θ_+ and θ_- has encouraged Beynon and various co-workers to study not fragment ion abundances, but the kinetic energy released when an ion fragments as a function of θ (43,47,48). One exception to this is a paper on fragment ion abundances of n-butylbenzene and methanol as a function of θ (44), but this includes calculations of ion abundances from T values using an expanded form of the calculations of Todd et al. Beynon et al have also published theoretical papers on the physics of high energy collisions (49), experimental requirements for obtaining ARMS data on commercial mass spectrometers (50) and possible mechanisms of excitation of ions during CA (47).

2.4.3 EXPERIMENTAL METHODS OF OBTAINING ARMS DATA

The experimental arrangements which have been used to obtain ARMS data are shown schematically in Figure 2.4 and they

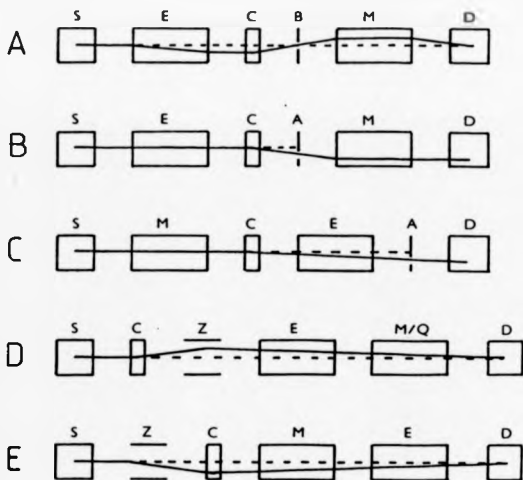


Figure 2.4 Block diagrams showing the many types of mass spectrometer which have been used to acquire ARMS data. Where; S is an ion source, E is an ESA, C is a collision chamber, B is a β -slit, M is a magnet, D is a detector, A is an angle-resolving slit, Z is the Z-deflectors and Q is a quadrupole mass filter.

CHAPTER 2

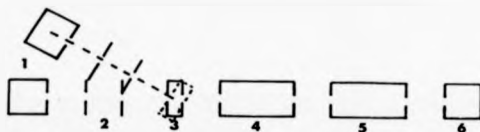
may be broadly split into two groups. The first group (A, D, E) uses pre- or post-collision electrical deflection of the ion beam to determine θ while the second group (B, C) uses movable angle resolving slits. The principal problems with the former methodology are:

- 1) The deflection potential V_m must be converted to θ by calculation.
- 2) At a given value of V_m , θ depends upon the mass of the fragment ion.
- 3) θ_{max} changes with the ion source tuning and alignment.

The use of movable slits has the advantage that θ is directly measurable and independent of fragment ion mass but it does mean that the fragment ions travel through one or more of the sectors of the mass spectrometer off the ion optical axis which affects the angular resolution which can be obtained. All of these methods rely on scattering occurring at a well defined point in space and therefore a very small collision region is essential if good angular resolution is to be obtained.

Possibly the best means of obtaining ARMS data would be that shown schematically in Figure 2.5, where the parent ions could be directed at an angle into the collision chamber and the fragment ions would travel along the normal ion optical axis of the spectrometer. Pre- and post-collision angular resolution would be adjusted by suitable slits and θ determined by the angle of the source. The construction and use of such an experimental apparatus is described in Chapters 5 to 8 of this thesis.

This method still has the problem that one cannot separate the



KEY

- 1) Ion source.
- 2) Angle defining slits.
- 3) Collision chamber.
- 4) ESA
- 5) Magnet.
- 6) Detector

Figure 2.5 A mass spectrometer with a moveable ion source, angle defining slits and collision chamber.

CHAPTER 2

effects of θ_+ and θ_- . This can be overcome using translational spectroscopy (51) where both the neutral and the fragment ion are detected. The application of this technique to ARMS has been reported for studying the scattering of acetone ions by helium atoms (52) and the data suggest that θ_+ is of comparable importance to θ_- .

CHAPTER 2

2.5 REFERENCES

- 1) C.J.W.Brooks, B.S.Middletich, in "Mass Spectrometry", Vol. 5, R.A.W.Johnstone, The Chemical Society, London, p142 (1979)
- 2) G.Guiochon, P.J.Arpin, *Anal. Chem.*, **52**, 51 (1979)
- 3) "Tandem Mass Spectrometry", F.W.McLafferty, Ed, John Wiley & Sons (1983)
- 4) K.Levsen, "Fundamental Aspects of Organic Mass Spectrometry", Verlag Chemie, Weinheim, 1975
- 5) M.S.B.Munson, F.H.Field, *J. Am. Chem. Soc.*, **88**, 2621 (1966)
- 6) H.D.Beckey "Principles of Field Ionization and Field Desorption Mass Spectrometry", Pergamon Press, 1977
- 7) H.R.Schullin, *Int. J. Mass Spectrom. Ion Phys.*, **32**, 97 (1979)
- 8) R.S.Lehrie, J.C.Robb, D.W.Thomas, *J. Sci. Instrum.*, **39**, 458 (1962)
- 9) M.Barber, R.S.Bordoli, R.D.Sedgewick, A.N.Tyler, *Chem. Commun.*, **325** (1961)
- 10) J.Roboz, "Introduction to Mass Spectrometry", Wiley-Interscience, New York, 1968
- 11) E.G.Johnson, A.O.Nier, *Phys. Rev.*, **91**, 10 (1953)
- 12) W.Paul, H.P.Reinhard, U. von Zahn, *Z. Phys.*, **152**, 143 (1958)
- 13) R.S.Lehrie, J.E.Parker, in "MTP International Review of Science : Vol. 5" ed. A.Maccoll, Butterworth, London, 1972
- 14) C.J.Drawery, G.C.Goodie, K.R.Jennings, in ref. 13

CHAPTER 2

- 15) J.A.Hipple, R.E.Fox, E.U.Condon, *Phys. Rev.*, **69**, 347 (1946)
- 16) J.H.Beynon, R.G.Cooks, R.M.Caprioli, G.R.Lester, *Metastable Ions*, Elsevier, Amsterdam, 1973
- 17) K.R.Jennings, R.S.Mason, in ref. 3
- 18) E.S.Mukhtar, I.W.Griffiths, F.M.Harris, J.H.Beynon, *Int. J. Mass Spectrom. Ion Phys.*, **37**, 159 (1981)
- 19) S.Tajima, S.Tobita, K.Ogino, Y.Niwa, *Org. Mass Spectrom.*, **21**, 236 (1986)
- 20) R.G.Cooks, D.T.Terwilliger, T.Ast, J.H.Beynon, T.Keough, *J. Am. Chem. Soc.*, **97**, 1583 (1975)
- 21) K.R.Jennings, *Int. J. Mass Spectrom. Ion Phys.*, **1**, 227 (1968)
- 22) R.G.Cooks, L.Hendricks, J.H.Beynon, *Org. Mass Spectrom.*, **10**, 625 (1975)
- 23) T.Ast, C.J.Proctor, C.J.Porter, J.H.Beynon, *Int. J. Mass Spectrom. Ion Phys.*, **40**, 111 (1981)
- 24) R.G.Cooks, "Collision Spectroscopy", R.G.Cooks, Ed., Plenum Press, New York, 1978
- 25) J.A.Laramée, D.Cameron, R.G.Cooks, *J. Am. Chem. Soc.*, **103**, 12 (1981)
- 26) F.W.McLafferty, P.F.Bente, III, R.Kornfeld, S.C.Tsai, I.Howe, *J. Am. Chem. Soc.*, **95**, 2120 (1973)
- 27) F.W.McLafferty, R.Kornfeld, W.F.Haddon, K.Levsen, I.Sakai, P.F.Bente, III, S.C.Tsai, H.D.R.Schuddemage, *J. Am. Chem. Soc.*, **95**, 3886 (1973)
- 28) P.H.Hemberger, J.A.Laramée, A.R.Mubik, R.G.Cooks, *J. Phys.*

CHAPTER 2

- Chem.*, **85**, 2335 (1981)
- 29) F.M.Bockhoff, F.W.McLafferty, *J. Am. Chem. Soc.*, **101**, 1793 (1979)
- 30) F.T.Smith, R.P.Marchi, K.G.Dedrick, *Phys. Rev.*, **150**, 79 (1966)
- 31) R.G.Cooks, K.C.Kim, J.H.Beynon, *Chem. Phys. Lett.*, **23**, 190 (1973)
- 32) T.Ast, D.T.Terwilliger, R.G.Cooks, J.H.Beynon, *J. Phys. Chem.*, **79**, 708 (1975)
- 33) V.Frenchetti, J.J.Carmody, D.A.Krause, R.G.Cooks, *Int. J. Mass Spectrom. Ion Phys.*, **26**, 353 (1978)
- 34) J.A.Laramée, P.H.Hemberger, R.G.Cooks, *Int. J. Mass Spectrom. Ion Phys.*, **33**, 231 (1980)
- 35) A.R.Hubik, P.H.Hemberger, J.A.Laramée, R.G.Cooks, *J. Am. Chem. Soc.*, **102**, 3997 (1980)
- 36) D.J.Burinsky, G.L.Glish, R.G.Cooks, J.J.Zwinselman, W.M.M.Hibbering, *J. Am. Chem. Soc.*, **103**, 465 (1981)
- 37) J.J.Zwinselman, A.G.Harrison, *Int. J. Mass Spectrom. Ion Processes*, **62**, 167 (1984)
- 38) J.J.Zwinselman, S.Macdon, A.G.Harrison, *Int. J. Mass Spectrom. Ion Processes*, **67**, 93 (1985)
- 39) E.E.Kingston, A.G.Brenton, R.K.Boyd, J.H.Beynon, *Int. J. Mass Spectrom. Ion Phys.*, **47**, 117 (1983)
- 40) S.A.McLucky, S.Verma, R.G.Cooks, M.J.Farncombe, R.S.Mason, K.R.Jennings, *Int. J. Mass Spectrom. Ion Phys.*, **48**, 423 (1983)
- 41) S.Verma, J.D.Ciupak, R.G.Cooks, A.E.Schoen, P.Dobberstein,

CHAPTER 2

- Int. J. Mass Spectrom. Ion Phys.*, 52, 311 (1983)
- 42) R.S. Mason, M.J. Farncombe, K.R. Jennings, R.G. Cooks, *Int. J. Mass Spectrom. Ion Phys.*, 43, 327 (1982)
 - 43) S. Singh, M.S. Thacker, F.M. Harris, J.H. Beynon, *Org. Mass Spectrom.*, 20, 156 (1985)
 - 44) D.S. Waddell, R.K. Boyd, A.G. Brenton, J.H. Beynon, *Int. J. Mass Spectrom. Ion Processes*, 68, 71 (1986)
 - 45) S. Verma, J.D. Ciupak, R.G. Cooks, *Int. J. Mass Spectrom. Ion Processes*, 62, 219 (1984)
 - 46) P.J. Todd, R.J. Vermack, E.H. McBay, *Int. J. Mass Spectrom. Ion Phys.*, 50, 299 (1983)
 - 47) S. Singh, F.M. Harris, R.K. Boyd, J.H. Beynon, *Int. J. Mass Spectrom. Ion Processes*, 66, 131 (1985)
 - 48) S. Singh, F.M. Harris, R.K. Boyd, J.H. Beynon, *Int. J. Mass Spectrom. Ion Processes*, 66, 151 (1985)
 - 49) R.K. Boyd, E.E. Kingston, A.G. Brenton, J.H. Beynon, *Proc. R. Soc. Lond.*, A392, 59 (1984)
 - 50) R.K. Boyd, E.E. Kingston, A.G. Brenton, J.H. Beynon, *Proc. R. Soc. Lond.*, A392, 107 (1984)
 - 51) D.P. de Bruijn, J. Los, *Rev. Sci. Instrum.*, 53, 1020 (1982)
 - 52) W.J. Van der Zande, D.P. de Bruijn, J. Los, P.G. Kistemaker, S.A. McLuckey, *Int. J. Mass Spectrom. Ion Processes*, 67, 161 (1985)

3.1 INTRODUCTION

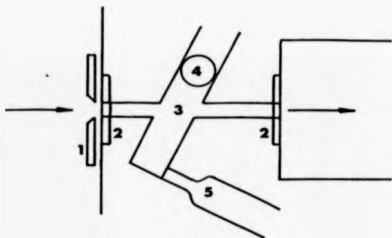
Preliminary studies of the use of the z-deflection method for the study of angle resolved mass spectrometry had previously been carried out at the University of Warwick (1). A working system was therefore ready for use but it was far from ideal and very little work had been done to identify those experimental variables which had the greatest effect on the ARMS data. In this chapter details of the implementation of the z-deflection method on the MS50 are given and a new collision system is described.

3.2 THE COLLISION CHAMBER

The first z-deflection experiments which had been undertaken on the MS50 (1,2) had utilized the ball valve between the ion source and ESA housings as a collision chamber (3), Figure 3.1. This method of introducing collision gas had a number of disadvantages which were particularly limiting when acquiring ARMS data. The first of these was that the collision region was long and badly defined which limited the possible angular resolution obtainable. Secondly, no direct or indirect measurement of collision gas pressure was possible and therefore the only methodology for obtaining repeatable gas pressures was to set a particular attenuation of the parent ion. Finally, a significant rise in the pressure in the ESA housing was observed when collision gas was admitted leading to tailing of peaks in linked scans because of decompositions occurring in the ESA.

To try and overcome these problems a new collision gas inlet

CHAPTER 3



KEY

- 1) Source slit.
- 2) Boundary slits.
- 3) Collision region.
- 4) Ball valve.
- 5) Gas inlet / Pumping line.

Figure 3.1 Cross-sectional view of the ball valve collision chamber which is described in detail in reference 3.

CHAPTER 3

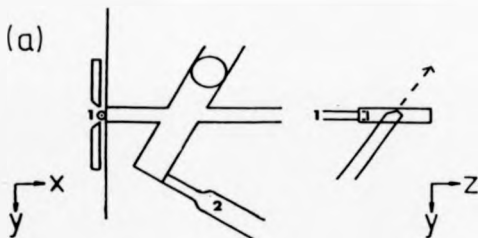
system was built for the MS50, the design aims were that:

- 1) The collision region should be short.
- 2) The presence of collision gas should not adversely affect pressures in the rest of the mass spectrometer.
- 3) The collision gas pressure should be reproducible, but not necessarily known absolutely.
- 4) The collision gas pressure should be stable for a long period of time.

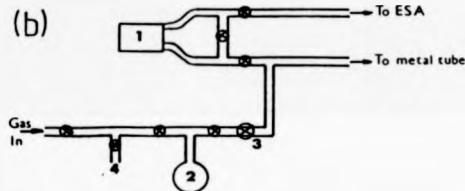
The system used is shown in Figures 3.2a and 3.2b. The region of highest collision gas pressure is at the end of the tube and only 1mm long in the direction of ion beam travel. Excess collision gas is pumped away by the source housing diffusion pump (6" pump, originally fitted for high pressure source studies (4)). Although the pressure in the collision region is not known, it is set by opening the needle valve until the required reading is obtained at the Baratron head and is therefore easily repeated. Most of the results described in the following chapter were obtained at Baratron readings of 1.3mmHg pressure i.e. ≈ 1.3 torr. As the collision gas is stored in a reservoir it is also possible to use a mixture of gases.

3.3 CALCULATING θ and $\Delta\theta$

In the MS50, ions are accelerated out of the ion source which is at a potential V , and brought to a focus at the continuously variable source slit which lies behind a slotted earth plate. After travelling a short distance the ions pass through a three position z-restrictor into y- and z-deflectors

**KEY**

- 1) 1mm diameter metal tube.
2) Pumping line.

**KEY**

- 1) Baratron head. 3) Fine needle valve.
2) Glass reservoir. 4) Rough pumping line.

Figure 3.2a The collision region.

Figure 3.2b The gas introduction system.

CHAPTER 3

which are used to align the ion beam along the ion optical axis before the beam enters the electrostatic analyser (ESA). Between the z-deflectors and the ESA is a cylindrical earthed tube, of length 96mm. Ions scattered during collisional activation at a point between the source slit and the z-restrictor are brought back on to the ion optical axis at the detector by the field produced by the z-deflector voltage (V_z). The y- and z-deflector voltages are produced within the MS50 source supply chassis and then carried by a multistrand cable to a connector on the outside of the monitor housing. At this point a voltmeter was connected in parallel with one of the cables leading to a z-deflector. The potential difference between one of the plates and ground (V_z), was therefore continuously displayed.

By altering V_z , ions which have been scattered through different angles can be detected and θ calculated using the following equation (2);

$$\theta = \sin^{-1} \left[\frac{(pqz)}{4s} = \frac{V_z}{V} \cdot \frac{m_1}{m_2} \right] \quad (1)$$

where from Figure 3.3;

p is the distance between the y & z-deflectors (6mm)

s is the separation of the z-deflectors (6mm)

q is the extent to which the field from the z-deflectors penetrates the earthed cylinder (assumed to be 11mm)

V_z is the potential difference between each z-deflector and ground (equal magnitude but opposite polarity on the two deflectors)

m_1 is the parent ion mass and m_2 is the daughter ion mass



Figure 3.3 Schematic diagram of the collision chamber , y and z-focus assemblies and the collector slit of the MSSO.

CHAPTER 3

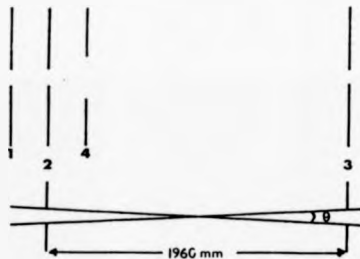
The method is very simple to implement on the MS50. With the source and collector z-restrictors set to their minimum widths, the source and deflector voltages are set to give the largest signal for the parent ion at the detector. The value of V_s at which this occurs is by definition $V_{s,max}$. The slits are then opened to the desired width and V_s set to give the value of θ at which daughter ions are to be observed.

The angular resolution obtainable using this method is difficult to calculate, since as can be seen from Figure 3.4, the z-deflectors are between the two adjustable slits used to define the ion beams' width in the yz plane. From the distance between the two z-restrictors (1960mm), it is possible to calculate a maximum spread in θ ($\Delta\theta$) of $\pm 0.11^\circ$ when the z-restrictors are fully open. This is much worse than the best reported angular resolution of 0.01° obtained in a similar study by Laramée et al. (5).

3.4 DATA COLLECTION

Data were collected by one of two methods depending upon the magnitude of the mass difference between the fragment ions under study. If the mass difference was small then a limited mass range B/E scan was performed, the scan law having been generated by analogue electronics. For fragment ions of widely different mass the appropriate E value was selected using a Fluke 720A voltage divider and then small magnet scans were performed about the required B value. In both cases data were acquired using a Biomat 1000 signal averager to improve the signal to noise ratio.

CHAPTER 3



KEY

	z-length / mm
1) Source slit	2.5
2) Source z-restrictor	2.5 ± 0.5
3) Collector z-restrictor	5 ± 0.5
4) z-deflector	

Figure 3.4 Schematic diagram of the slits which alter the angular resolution obtained when using the z-deflection method.

CHAPTER 3

3.5 REFERENCES

- 1) R.S. Mason, M.J. Farncombe, K.R. Jennings, R.G. Cooks, *Int. J. Mass Spectrom. Ion Phys.*, **43**, 327 (1982)
- 2) M.J. Farncombe, Ph.D Thesis, Warwick University, 1983
- 3) R.S. Stradling, K.R. Jennings, S. Evans, *Org. Mass Spectrom.*, **13**, 429 (1978)
- 4) D.K. Bohme, J.A. Stone, R.S. Mason, R.S. Stradling, K.R. Jennings, *Int. J. Mass Spectrom. Ion Phys.*, **37**, 283 (1981)
- 5) J.A. Laramée, J.J. Carmody, R.G. Cooks, *Int. J. Mass Spectrom. Ion Phys.*, **79**, 708 (1975)

CHAPTER 4

4.1 INTRODUCTION

While the swinging source was under construction, data were obtained on the MS50 using the z-deflection method (1) and the aims of the experiments were therefore restricted by the limitations of this method which were discussed in detail in Chapter 3 and are given briefly below:

- 1) A poorly defined collision region.
- 2) The angular resolution depends upon θ .
- 3) θ_{min} changes with ion source tuning and alignment.
- 4) The z-deflector voltage (V_z) is a function of θ dependent upon the mass of the fragment ion.

Data were therefore obtained primarily to discover which experimental variables had the greatest influence on angle resolved mass spectra.

4.2 COLLISION GAS PRESSURE

In Figure 4.1 the 91/92 fragment ion ratio of n-butylbenzene is plotted as a function of the collision gas (Argon) pressure (P) at θ_{min} . These data do not agree with the results of Beynon et al. (2) which show the 91/92 ratio to be invariant with P (He and N₂ collision gases) at low gas pressures, but rising at higher pressures because of either:

- a) Closer and therefore more energetic ion/neutral interactions.

and/or

- b) Multiple collisions.

Their data however do not include metastable ions whereas the

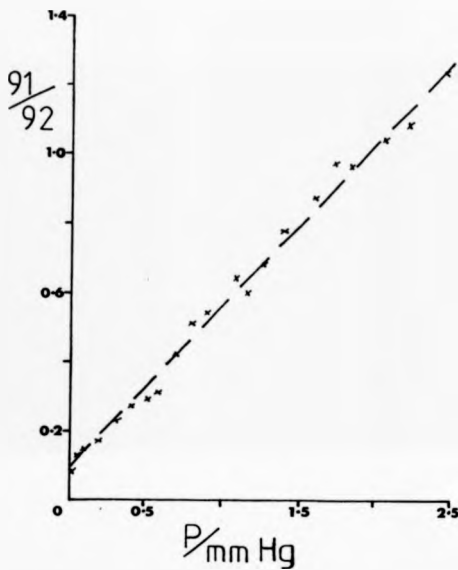


Figure 4.1 The 91/92 fragment ion ratio of n-butylbenzene as a function of the collision gas (Argon) pressure (P) at

9 eV.

CHAPTER 4

data given in Figure 4.1 do and therefore show that the abundance of the m/z 91 fragment ion is more pressure dependent than the m/z 92 ion. This can clearly be seen from Figures 4.2a, 4.2b and 4.2c, where the abundances of the two fragment ions are plotted as a function of P normalised to their abundances at P_0 (0.028 mmHg on the Baratron gauge, see Chapter 3) for $\theta=0^\circ$, $\approx 0.1^\circ$ and $\approx 0.5^\circ$ i.e. $V_a = 95V$, $50V$ and $-50V$ respectively. To try to compensate for the effect of metastable ions on the fragment ion abundances, corrected fragment ion abundances were calculated using the following equation:

$$I_{p-x} = i_{p-x} - (i_{p=0} \times T_{p-x}) \quad (1)$$

where

I_{p-x} is the corrected fragment ion abundance at $P=x$

i_{p-x} is the raw fragment ion abundance at $P=x$

$i_{p=0}$ is the raw fragment ion abundance at $P=0$

T_{p-x} is the percentage transmission of the *n*-butylbenzene molecular ion at $P=x$

Figures 4.2b and 4.2c also include data on the variation of the 91/92 ratio (calculated using the corrected ion abundances) as a function of P . The ratios are larger than those in Figure 4.1 and show less of a dependence upon pressure, which is more in keeping with the data in later chapters of this thesis. The change in the 91/92 ratio which occurs when m^+ ions are removed is apparently not allowed for in references 3 & 5, but may radically affect the interpretation of these ARMS data. Also, when

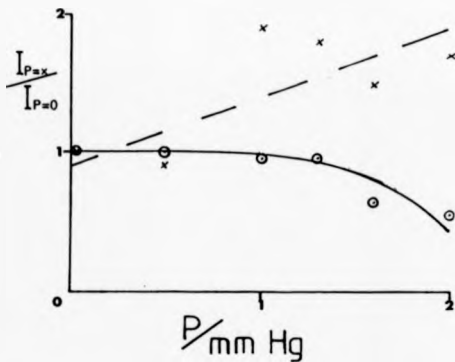


Figure 4.2a The ratios of the abundances of the m/z 91 (x) and m/z 92 (o) fragment ions from *n*-butylbenzene at $P=x$, relative to $P=0$ for fragment ions detected when $\theta=0^\circ$.

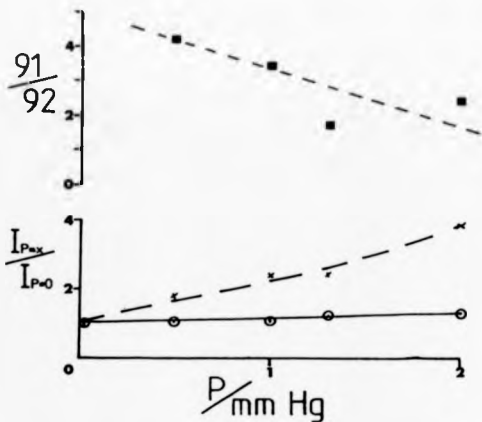


Figure 4.2b The ratios of the abundances of the m/z 91 (\times) and m/z 92 (\circ) fragment ions from *n*-butylbenzene at $P=x$, relative to $P=0$. The 91/92 fragment ion ratio (\blacksquare), calculated using corrected fragment ion abundances (see text) is also plotted as a function of P for fragment ions detected when $\theta=0.1^\circ$.

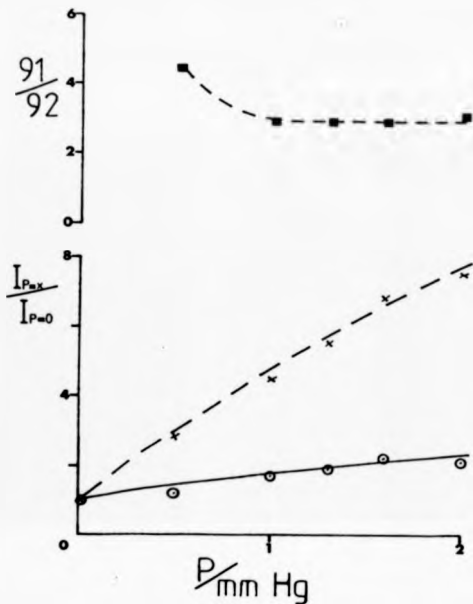


Figure 4 2c The ratios of the abundances of the m/z 91 (x) and m/z 92 (o) fragment ions from *n*-butylbenzene at $P=P$, relative to $P=0$. The 91/92 fragment ion ratio (■), calculated using corrected fragment ion abundances (see text) is also plotted as a function of P for fragment ions detected when $\theta=0.5^\circ$.

CHAPTER 4

comparing ARMS results obtained on different designs of mass spectrometer, the proportion of the total ion signal arising from unimolecular dissociations will be different because it depends upon many factors including:

- 1) The amount of collision gas which leaks into the field free regions either side of the collision chamber.
- 2) The lengths of the field free regions (F.F.R) of the spectrometer.
- 3) The position of the collision chamber i.e. which F.F.R., as this affects the average internal energy of the parent ions before collisional activation.

In view of these factors the angle resolved mass spectra will be different.

4.3 EFFECT OF THE PARENT IONS BEFORE COLLISIONAL ACTIVATION

If the 91/92 ratio depends upon the internal energy of the parent ion after collisional activation then this should change if either the amount of energy gained during CA changes (alter θ) or if the internal energy of the ion before the collision changes (alter energy of ionising electrons). The 91/92 ratio was therefore determined for n-butylbenzene parent ions which had been formed in an electron impact source, using electrons of energy 70, 60, 50, 30 and 20eV. The curves obtained when using electrons of 70, 50 and 20eV energy (the 30eV and 50eV data were very similar to each other) are given in Figure 4.3 and they confirm that E_{int} does affect ARMS data. A more detailed study over a smaller range of electron energies was then undertaken, the results of

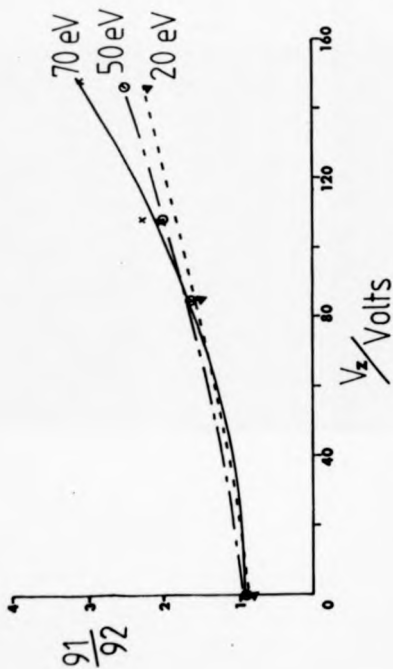


Figure 4.3 The 91/92 fragment ion ratio of n-butylbenzene parent ions formed in an electron impact ion source using electrons of 70 (\times), 50 (e) and 20eV (v), as a function of V_z/V_e .

CHAPTER 4

which are plotted in Figure 4.4. ARMS data on n-butylbenzene are often compared to the results from the photodissociation studies of Beynon et al. (6) and it is interesting to look at the 91/92 ratios obtained when eg V_m was 120V ($\theta = 0.4^\circ$) and note the photon energies needed to give the same ratios, as shown in Table 4.1. Not unreasonably the comparison suggests that changing the excitation energy in the field free region has a greater effect upon the finally observed product ion ratio than attempting to alter the energy deposited in the parent molecule upon ionisation.

TABLE 4.1 Comparing 91/92 ratios obtained from photoexcitation experiments with collisional activation of molecular ions ionised by electrons of different energies.

Electron Energy / eV	91/92 Ratio	Photon Energy / eV
15	2.4	2.85
20	2.55	2.9
23	3.0	3.0
25	3.5	3.1

There are a number of problems with the above comparison. Firstly the accuracy of the photodissociation data has recently been questioned in publications by other groups (7,8). This has prompted Beynon et al. to review published data on the fragmentation of n-butylbenzene (9). This review mentions a

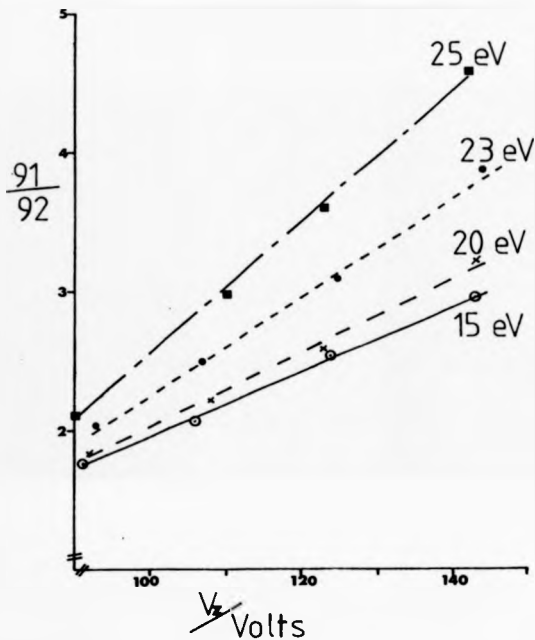


Figure 4.4 The 91/92 fragment ion ratio of n-butylbenzene parent ions formed in an electron impact ion source using electrons of 25 (■), 23 (●), 20 (*) and 15eV (○), as a function of V_0 .

CHAPTER 4

second possible problem with the comparison of ARMS and photodissociation data namely that the latter data do not include metastable ions whereas the former do. This is particularly important since the early studies on CA (10) from McLafferty et al. showed that as a rule except when considering unimolecular fragmentations the internal energy of the parent ions before CA did not affect fragment ion abundances. A few exceptions to this rule have been reported (11-13), but the data on benzoyl ions in reference 12 have been contradicted by later data from McLafferty et al. (14). Another problem with looking for internal energy effects in CID spectra is the expected poor repeatability ($\pm 5\%$, reference 14) of relative fragment ion abundances.

The data in Figures 4.3 & 4.4 include the products from unimolecular fragmentations and the 91/92 ratios can therefore be seen to depend upon four independent ion abundances;

$$\frac{91}{92} = \frac{91_{\text{un}} + 91_{\text{CA}}}{92_{\text{un}} + 92_{\text{CA}}} \quad (2)$$

Lowering the energy of the ionising electrons will tend to increase the m^+/CID ratio of each fragment ion. Changing the electron energy will also alter the $m^+ 91/92$ ratio i.e. $91_{\text{un}}/92_{\text{un}}$, as shown in Table 4.2 below.

Williams and Cooks (15) were the first to report that, for a variety of competing rearrangement and direct bond cleavage reactions, the abundance of the metastable ion for the rearrangement reaction increased relative to that for the direct bond cleavage as the electron energy was lowered. Similar results have been obtained by other workers and in particular

CHAPTER 4

Brown (16) studied eight compounds, including n-butylbenzene, and reported the results given below.

TABLE 4.2 The $m^+ 91/92$ ratio of n-butylbenzene molecular ions ionised by electrons of energies 70, 15, 13 & 11eV.

Electron Energy/eV	70	15	13	11
$m^+ 91/92$ ratio	0.16	0.10	0.09	0.07

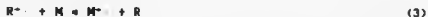
Given that the $m^+ 91/92$ ratio is reduced by lowering the electron energy, one would expect the ($m^+ + \text{CID}$) 91/92 ratio to decrease, particularly when θ is small as, from the data in Figure 4.2 the metastable contribution to the ratio is most significant at these small angles. As changing the electron energy has the greatest effect on the ($m^+ + \text{CID}$) 91/92 ratio at larger values of θ , were metastable ions are only a small part of the total fragment ion signal, the data in Figure 4.4 do suggest that the 91/92 ratio for collision induced dissociations depends upon the internal energy of the molecular ion before collisional activation. An analogous effect has been reported by Baynon et al. (17) when studying the photodissociation of n-butylbenzene. They found that, at a fixed photoexcitation energy the, 91/92 ratio depended upon the ion source temperature; their data do not include fragment ions resulting from unimolecular fragmentation because phase locked detection was used. Turning to low energy collisional activation however, Dawson (18) found that the 91/92 ratio was independent of electron energy on a triple quadrupole mass spectrometer

CHAPTER 4

(i.e. no metastable contribution to the fragment ion abundance).

Charge exchange has frequently been used by Harrison and co-workers to study the fragmentation of an ion as a function of its internal energy (19) i.e. to produce breakdown curves.

Experimentally the technique is relatively simple. The compound being investigated is introduced into a high pressure ion source containing one of a number of different gas mixtures which, when ionised by electron impact give, reagent ions of known recombination energy. So for;



the upper limit of the internal energy of M^+ is given by

$$E(M^+)_{\text{max}} = RE(R^+) - IE(M) + E_{\text{therm}} \quad (4)$$

where

$RE(R^+)$ is the recombination energy of the reactant ion R^+ .

$IE(M)$ is the ionisation energy of M

E_{therm} is the initial thermal energy of the molecules and assumes no E_{int} in R

By using a number of different reagent ions, $E(M^+)$ can be varied over quite a wide range, typically 1 - 6eV, and the relative abundances of fragment ions produced inside the ion source can be used to produce the breakdown curves. Obviously, if charge exchange ionisation could be used to produce n-butylbenzene

CHAPTER 4

molecular ions of known internal energy which could then undergo CID, then this would be another way of investigating the variation in the 91/92 fragment ion ratio with θ as a function of $E(M^+)$. Two different gas mixtures were tried, Ar and COS/CO, the reagent ions being Ar^{+} (RE = 15.8eV) and COS^{+} (RE = 11.2eV), since the ionisation energy of n-butylbenzene is 8.69eV (20), then $E(M^+)_{MAX}$ was 7.11eV and 2.51eV respectively. The data obtained are shown in Figure 4.5 and it is noticeable that;

- 1) The 91/92 ratios are much smaller than expected from the other data reported herein.
- 2) Changing the reagent ion seems to have much less effect on the 91/92 ratio than is expected from the data in Figures 4.3 and 4.4.

The explanation for both points may be the effect of deactivating collisions (21) occurring inside the ion source on the internal energy of ions which then fragment outside the ion source. When Bowers et al. (11) studied the CA mass spectra of NH_4^+ ions prepared by charge exchange they found that differences between daughter ion spectra resulting from changing the reagent ion were reduced as the source pressure was increased and with it the number of ion-molecule collisions. These were causing collisional deactivation of the molecular ions which reduced their internal energy so that E_{int} upon leaving the ion source was less than E_{int} after charge transfer ionisation.

Having apparently found a link between $E(M^+)$ and the fragment ion ratio after CA for n-butylbenzene, it was decided to try similar experiments on other compounds, the first of which was

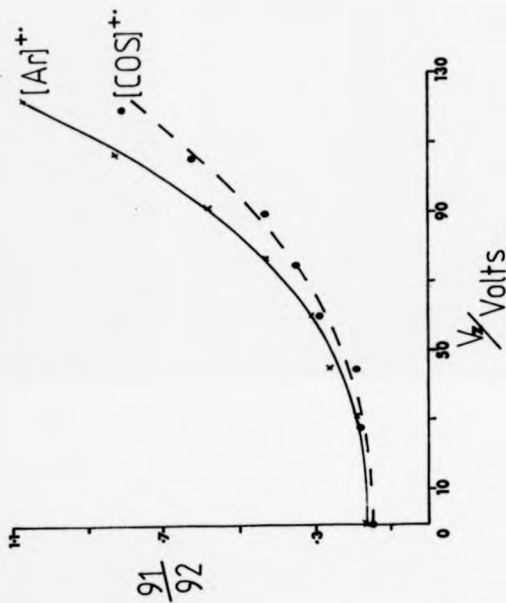


Figure 4.5 The 91/92 fragment ion ratio of n-butylbenzene parent ions formed by charge exchange with $[Ar]^{+\bullet}$ (x) or $[COS]^{+\bullet}$ (o), as a function of V_e .

CHAPTER 4

benzyl methyl ether. Todd and others (22,23) have suggested that fragment ions are observed off the ion optical axis of the spectrometer, because they are deflected by the kinetic energy released during their formation. So, for two fragment ions of similar mass, the one whose formation involves the greatest release of kinetic energy will be most abundant at large values of θ . For benzyl methyl ether T for $M^+ = 92^+$ > T for $M^+ = 91^+$, in contrast to n-butylbenzene for which the converse situation exists and therefore the change in the 91/92 ratio with θ cannot be explained from the kinetic energy release difference alone.

Figure 4.6 is the 70eV ARMS spectrum of benzyl methyl ether and this is directly comparable to the data of Cooks et al. in reference 4. Once again lowering the electron energy reduced the 91/92 ratio at a given angle as shown in Figure 4.7.

The data in Figure 4.8 shows how the intensities of four fragment ions from ethyl phenylacetate vary with θ . Once again measurements were made using electrons of 10 and 30eV energy to ionise the molecule and in each case the fragment ion ratios were different. The four fragment ions are formed by the reactions described in Table 4.3 and Figure 4.9:

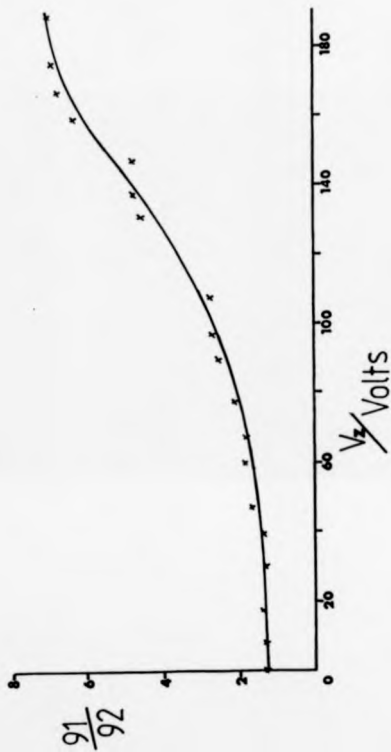


Figure 4.6 The $\frac{91}{92}$ fragment ion ratio of benzyl methyl ether as a function of V_z .

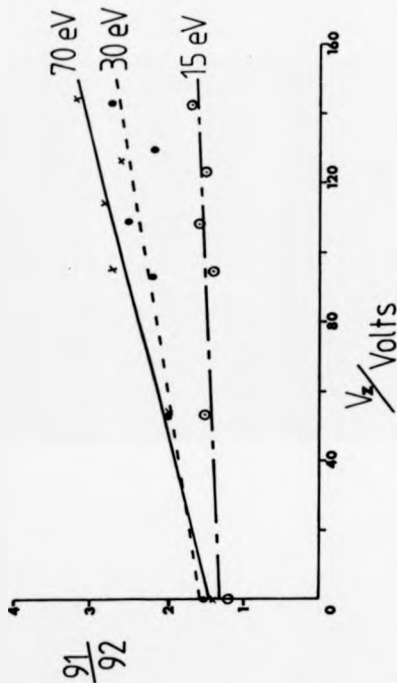


Figure 4.7 The 91/92 fragment ion ratio of benzyl methyl ether parent ions formed in an electron impact ion source using electrons of 70 (x), 30 (•) and 15 eV (○), as a function of V_z/V_0 .

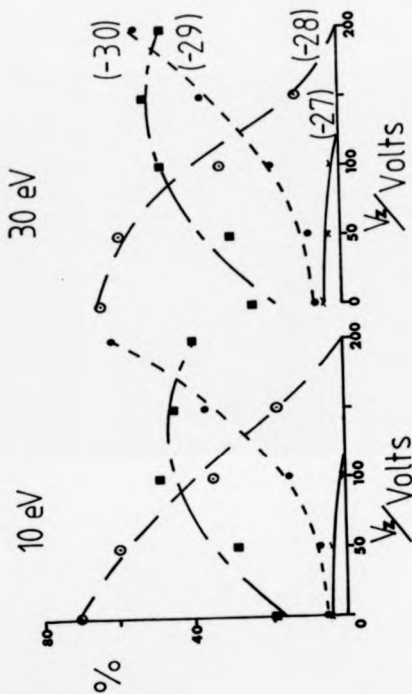
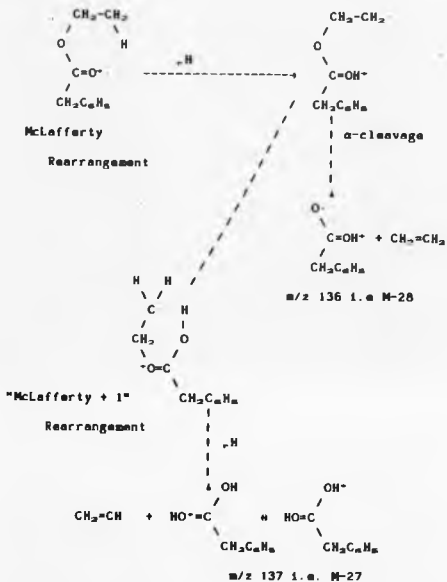


Figure 4.8 Relative fragment ion abundances of ethyl phenylacetate as a function of V_e , for parent ions formed in an electron impact ion source using electrons of 10 and 30 eV.

FIGURE 4.9 The origin of the M-27 and M-28 fragment ions of ethyl phenylacetate.



CHAPTER 4

TABLE 4.3 The origin of four of the fragment ions of ethyl phenylacetate.

LOSS/mass units	NEUTRAL	FRAGMENTATION TYPE (24)
27	C_7H_5	"McLafferty + 1" rearrangement
28	C_7H_4	McLafferty rearrangement
29	C_7H_3	α -cleavage
30	CH_2CO ?	rearrangement + cleavage ?

These losses are characteristic of esters but the loss of 30 mass units is usually only found for methyl esters. Qualitatively these data are similar to the n-butylbenzene data because simple cleavage reactions dominate at large values of θ . Using a B^2/E scan it was found that the fragment ion of mass 134 had two parents i.e. m/z 164 (loss of 30 mass units) and m/z 162 (loss of 28 mass units), but as θ increased loss of 30 mass units was the dominant process. The relative magnitude of the kinetic energy released during the loss of 28, 29 & 30 mass units was calculated from a small metastable map (25) and found to be $28 < 29 < 30$. In part the increased abundance of (M-29) and (M-30) (relative to (M-27) and (M-28)) with increasing θ may be a consequence of the relatively large kinetic energy release associated with their formation.

CHAPTER 4

4.4 PARENT ION LIFETIME BEFORE COLLISIONAL ACTIVATION

The next experimental variable to be investigated was the ion repeller voltage which alters the residence times of the parent ions in the ion source; this effect has been used by some workers when studying metastable ion lifetimes (23). Those parent ions which had spent the greatest time in the ion source fragmented in the field free region to give the largest 91/92 ratios, Figure 4.10. Making the repeller voltage more negative, affects the 91/92 ratio in two ways. Firstly, if an ion spends more time in the ion source then the probability that it will undergo fragmentations having lower rate constants increases i.e. rearrangement reactions will occur in the ion source and not in the field free region. The metastable contribution to the m/z 92 ion will therefore be reduced and the ($m^+ + \text{CID}$) 91/92 ratio should increase. Secondly, parent ions that do leave the ion source must have low internal energies and therefore must gain more internal energy during CA before they can fragment. At a particular value of θ therefore the 91/92 ratio would decrease as the repeller voltage became more negative. The data in Figure 4.10 suggests that the first effect is dominant.

4.5 CONCLUSIONS

The data in this chapter illustrate the following points;

- 1) If ARMS data obtained on different instruments are to be compared then rigorous control of experimental conditions is essential.
- 2) Changes in CA spectra are difficult to rationalise if the

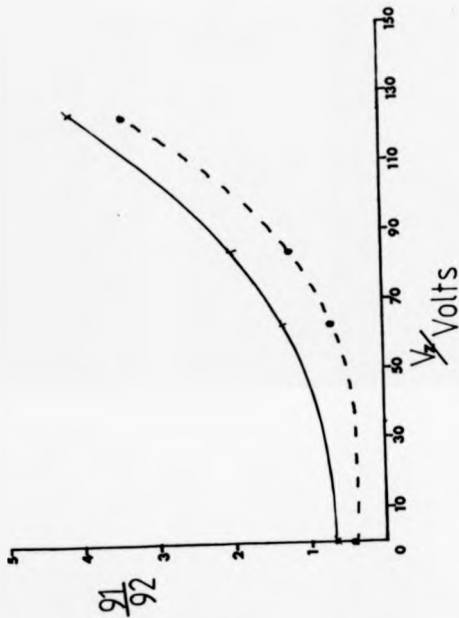


Figure 4.10 The 91/92 fragment ion ratio of n-butylbenzene parent ions produced when the ion source repeller voltage is -1.8V (+) or +19V (•) as a function of

V.

CHAPTER 4

unimolecular contributions to the spectra have not been removed.

Remembering the importance of point 2 above, the following tentative conclusions can be drawn from the data;

3) ARMS spectra are affected by the internal energy of the parent ion before CA.

4) The internal energy gained during collisional activation of an ion increases as θ increases.

CHAPTER 4

4.6 REFERENCES

- (1) R.S.Mason, M.J.Farncombe, K.R.Jennings, R.G.Cooks, *Int. J. Mass Spectrom. Ion Phys.*, **42**, 327 (1982)
- (2) I.W.Griffiths, E.S.Mukhtar, R.E.March, F.M.Harris, J.H.Beynon, *Int. J. Mass Spectrom. Ion Phys.*, **39**, 125 (1981)
- (3) E.E.Kington, A.G.Brenton, R.K.Boyd, J.H.Beynon, *Int. J. Mass Spectrom. Ion Phys.*, **47**, 117 (1983)
- (4) S.A.McLuckey, S.Verma, R.G.Cooks, M.J.Farncombe, R.S.Mason, K.R.Jennings, *Int. J. Mass Spectrom. Ion Phys.*, **48**, 423 (1983)
- (5) S.Verma, J.D.Cupek, R.G.Cooks, A.E.Schoen, P.Dobberstein, *Int. J. Mass Spectrom. Ion Phys.*, **52**, 311 (1983)
- (6) E.S.Mukhtar, I.W.Griffiths, F.M.Harris, J.H.Beynon, *Int. J. Mass Spectrom. Ion Phys.*, **37**, 159 (1981)
- (7) J.H.Chen, J.D.Mays, R.C.Dunbar, *J.Phys. Chem.*, **88**, 4759 (1984)
- (8) M.J.Welch, D.J.Perales, E.White,V., *Org. Mass Spectrom.*, **20**, 425 (1985)
- (9) R.K.Boyd, F.M.Harris, J.H.Beynon, *Int. J. Mass Spectrom. Ion Processes*, **66**, 185 (1985)
- (10) F.W.McLafferty, P.F.Bente III, R.Kornfeld, S.-C.Tsai, I.Howe, *J. Am. Chem. Soc.*, **95**, 2120 (1973)
- (11) P.A.M.van Koppen, A.J.Illas, S.Liu, M.T.Bowers, *Org. Mass Spectrom.*, **9**, 399 (1982)
- (12) C.J.Porter, R.P.Morgan, J.H.Beynon, *Int. J. Mass Spectrom. Ion Phys.*, **28**, 321 (1978)

CHAPTER 4

- (13) C.J.Porter, C.J.Proctor, J.H.Beynon, *Org. Mass Spectrom.*, 16, 62 (1981)
- (14) F.W.McLafferty, A.Hirota, M.P.Barbales, R.P.Pagues, *Int. J. Mass Spectrom. Ion Phys.*, 35, 299 (1980)
- (15) D.H.Williams, R.G.Cooks, *Chem. Commun.*, 663 (1968)
- (16) P.Brown, *Org. Mass Spectrom.*, 3, 1175 (1970)
- (17) I.W.Griffiths, E.S.Mukhter, F.M.Harris, J.H.Beynon, *Int. J. Mass Spectrom. Ion Phys.*, 43, 283 (1982)
- (18) P.H.Dawson, *Int. J. Mass Spectrom. Ion Processes*, 63, 339 (1985)
- (19) Y.H.Li, J.A.Herman, A.G.Harrison, *Can. J. Chem.*, 59, 1753 (1981)
- (20) P.Brown, *Org. Mass Spectrom.*, 3, 1175 (1970)
- (21) J.D.Lambert, *Vibrational and Rotational Relaxation of Gases* Clarendon Press, Oxford (1977)
- (22) P.J.Todd, R.J.Warmack, E.H.McBay, *Int. J. Mass Spectrom. Ion Phys.*, 50, 299 (1983)
- (23) D.S.Waddell, R.K.Boyd, A.G.Brenton, J.H.Beynon, *Int. J. Mass Spectrom. Ion Processes*, 68, 71 (1986)
- (24) F.W.McLafferty, "Interpretation of Mass Spectra", *University Science Books* (1980)
- (25) G.R.Warburton, R.S.Stradling, R.S.Mason, M.J.Farncombe, *Org. Mass Spectrom.*, 16, 507 (1981)
- (26) N.D.Coggeshall, *J. Chem. Phys.*, 37, 2167 (1962)

CHAPTER 5

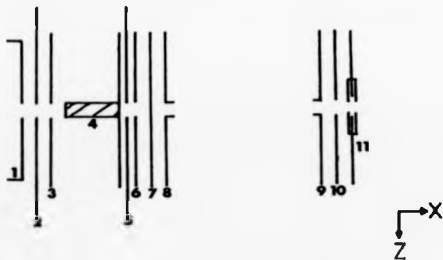
5.1 INTRODUCTION

In this chapter the 'swinging source' designed by Prof. K.R.Jennings, Dr. R.S.Mason (both of whom were at that time working at the University of Warwick) and S.Evans (employed by Kratos Ltd.) with assistance from Dr. J.A.Laramée (a post-doctoral assistant from Purdue University) is described. The source was built by Kratos Ltd. for use with their MS50 mass spectrometer, the prototype of which is in use at the University of Warwick.

5.2 DESCRIPTION OF THE SOURCE

The main components of the swinging source are shown schematically in Figure 5.1. They are bolted to a stainless steel sub-frame and insulated from it and each other by quartz spacers and vitresol tubing. The sub-frame is attached to a stainless steel ring (this ring has the ion source magnets fixed to it when a normal MS50 EI source is being used) by two pivots which lie along the y-axis bisecting the collision chamber. The sub-frame can therefore be moved so that the ion chamber describes an arc on a xz plane, whose origin is the centre of the collision chamber. To accommodate the swinging source a source housing extension (30cm long, 17.8cm outside diameter) is fitted and this is evacuated by an oil diffusion pump (Diffstat 100 Mk2M, 280l^s⁻¹) through a 4" diameter port which is directly below the ion chamber. The collision chamber is located inside the normal MS50 source housing which is pumped by a 6" oil diffusion pump (Edwards E06, 360l^s⁻¹) originally fitted to allow high pressure ion sources to be used (1). The ball valve region between the

CHAPTER 5



KEY

- 1) Ion Source
- 2) 1st Earth Plate
- 3) Aperture Plate
- 4) Y-deflectors
- 5) 2nd Earth Plate
- 6) High Voltage Plate
- 7) Y-deflectors
- 8) Z-deflectors
- 9) Beam Flag
- 10) Adjustable z-restrictor
- 11) Collision Chamber

Voltage on component / Volts

- | |
|-----------|
| 0 to 8000 |
| 0 |
| 0 |
| ± 60 |
| 0 |
| 0 to 3000 |
| ± 60 |
| ± 60 |
| 0 |
| 0 |
| 0 |

Figure 5.1 Schematic diagram of the swinging source (not to scale).

CHAPTER 5

source and electrostatic analyser housings may also be used as a collision chamber (2) and is pumped by a 2" oil diffusion pump (Edwards EO2, 801s-'') fitted with a water cooled baffle. The ball valve pumping line pressure is typically 2×10^{-7} torr, but when collision gas is admitted to the swinging source collision chamber this rises to e.g. 6×10^{-7} torr for 70% attenuation of the signal due to methanol molecular ions by argon collision gas. If the pressure inside the ball valve pumping line is directly related to the pressure inside the collision chamber, then an inverse linear relationship between it and the natural log of the primary ion beam intensity is expected (3). It can be seen from Figure 5.2 that such a relationship does exist for collision gas pressures up to that required to give 90% attenuation of the primary ion beam.

The source sub-frame is connected to a micrometer on the source housing extension by a hinged arm. The micrometer setting is directly proportional to the observed scattering angle and this changes approximately 1' when the micrometer setting is altered by 300 divisions (337.2 divisions = 1', see Appendix I).

The primary ion beam divergence in the xy plane is determined by the diameter of the first aperture and the length of the adjustable z-restrictor on the swinging source (see Figure 5.1 and Table 5.1 overleaf).

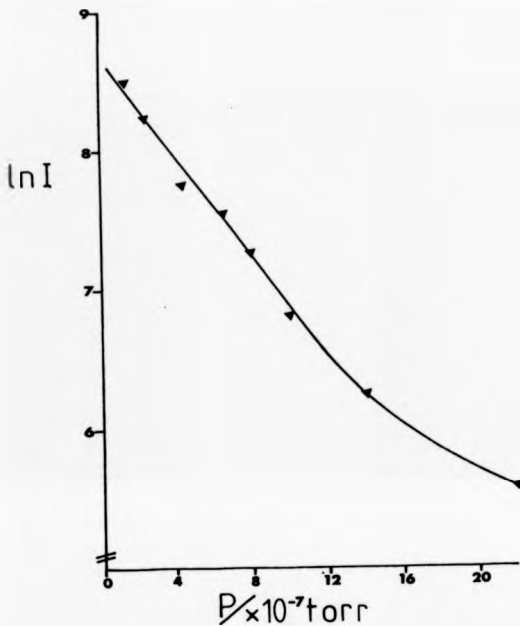


Figure 5.2 The abundance of the methanol molecular ion as a function of the collision gas (Argon) pressure.

CHAPTER 5

TABLE 5.1 Changes in the pre-collision beam divergence with the z-restrictor length.

Z-restrictor length / mm	Pre-collision beam divergence / degrees
2.54	+/- 0.39
0.508	+/- 0.13

The angular acceptance of the detector in the xz plane is determined by the MSSO source and collector slit lengths as detailed in the Table 5.2 below (for details of the calculations see Appendix I).

TABLE 5.2 The angular acceptance of the detector at various source and collector slit lengths.

Source slit length / mm	Collector slit length / mm	Detector angular acceptance / °
2.54	5.08	+/- 0.11
1.27	2.54	+/- 0.06
0.508	0.508	+/- 0.01

The range of scattering angles observed at any given angle is the sum of the primary beam divergence and the angular acceptance of the detector. These were usually set at +/- 0.13° and +/- 0.11° respectively, which gave an overall range of +/- 0.24° as evident from the beam profile in Figure 5.3.

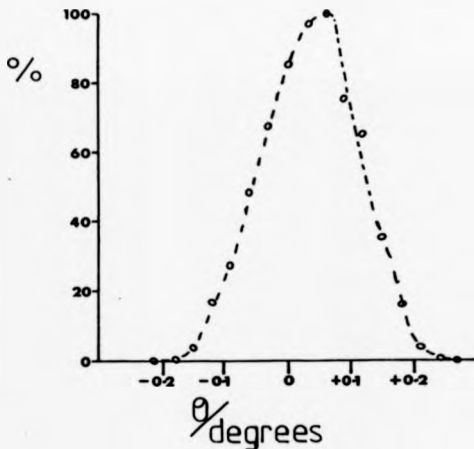


Figure 5.3 The abundance of the methanol molecular ion as a function of θ in the absence of collision gas. Pre-collision beam divergence set to $\pm 0.13^\circ$ and detector angular acceptance in the xz plane $\pm 0.11^\circ$.

CHAPTER 5

The angular acceptance of the detector in the yz plane is difficult to determine because of the focusing properties of the electrostatic analyser but a simple calculation indicates that it was always $< 0.5^\circ$.

Initially an electron impact ion source was used but as no source magnets could be fitted the resulting ion beam was of low intensity. An MS50 CI source fitted with an EI filament assembly was therefore tried and gave an order of magnitude more intense ion beam when used like an EI source (i.e. no reagent gas, electron energy $< 70\text{eV}$ and repeller voltage $> 0\text{V}$) but with a high sample pressure. Electrical connections to the source are made by sleeved nichrome wires via a standard MS9 source flange, which is bolted to the base of the source housing extension and vacuum sealed with a viton o-ring ($4.734\text{cm} \times 0.139\text{cm}$). Sample is admitted via a hollow feedthrough on the source flange which is connected to a modified inlet cup on the ion source by a length of $\frac{1}{4}$ " diameter teflon tubing.

Three millimetres forward of the ion source (see Figure 5.1) is an earthed plate with a central hole of diameter 3.6mm and 5mm and in front of this is the first beam defining aperture plate which is connected to an electrical feedthrough on the source housing extension. This can either be grounded directly, in which case the aperture plate is at ground potential, or via an electrometer which will measure the electric current produced when the ion beam hits the aperture plate i.e. the plate is being used as a beam flag. The ion beam then passes between a pair of y-deflectors which are used to correct for minor source alignment errors and/or

CHAPTER 5

to pulse the ion beam e.g. when using phase locked detection systems. Next is a pseudo einzel lens (4) assembly consisting of an earth plate followed by a high voltage plate and y- and z-deflectors. The lens is used to focus the ion beam onto the collision chamber which is 20mm forward of the high voltage plate. Before the collision chamber is an adjustable z-restrictor and the ion beam flag plate. As the lens voltage is increased, the focal point is moved back along the x-axis towards the ion chamber. When the focal point is inside the collision chamber, the detector signal is maximized and the beam flag current is at its minimum, as shown by the data in Figure 5.4. The pseudo einzel lens voltage is generated by a dedicated power supply (Wallis Electronics Ltd., Model R103/3/1P) the output of which is continuously variable between 0 and +10kV. The six deflector voltages are produced by dividing the output of two 0 to +/- 1kV power supplies (Wallis Electronics Ltd., Model 1PMR2) with a network of high stability resistors and potentiometers. With one power supply set at + 200V and the other at - 200V, the deflector voltages can be independently set at any voltage between + and - 60V.

The collision chamber is a cylinder of diameter 2.54mm and depth 0.4mm with rectangular ion beam entry and exit slits which are 16mm long (z-axis) and 0.26mm high (y-axis). It is connected to an inlet flange on the MS50 source housing by a piece of silicon tubing (1.5mm ID x 1.6mm wall). Gas is piped along copper tubing to the inlet flange and its flow is regulated by a needle valve (Whitay Co., Model SS 22 RS4).

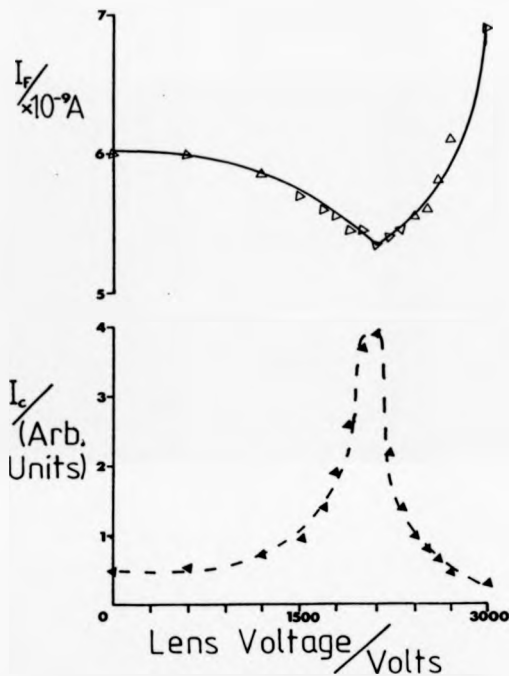


Figure 5.4 The measured beam flag current (upper trace) and MS50 detector signal (lower trace) for different values of the einzel lens voltage

CHAPTER 5

Correct alignment of source components is ensured by the use of dowel rods during assembly.

5.3 OPERATING PROCEDURE

Zero angle (θ_{zero}) for the source is determined by the following procedure. First, all the z-restrictors are set at their minimum position then, with sample admitted to the ion source at the desired pressure, the source tuning controls are adjusted to maximize the beam flag current. The source micrometer is then used to change the angle of the source until the collector signal for the ion under investigation is maximized. The micrometer setting at which this occurs is by definition θ_{zero} and $\theta_{observed}$ is measured relative to this value. Voltages are now applied to the einzel lens and z-deflectors to enhance the detector signal. Finally, the z-restrictors are reset to give the required angular resolution. To minimize any errors caused by freeplay in the micrometer/link arm assembly, scattering angles are always selected by moving the ion source to the left of the centre marker which is seen through a window on the source housing extension and the chosen angle will always be larger than the one that preceded it.

5.4 INITIAL RESULTS

To test the performance of the swinging source, two systems for which ARMS data are readily available were used namely the scattering of Ar⁺ by Ar and [CH₃OH]⁺ by Ar.

The scattering of Argon ions by Argon atoms (5) is well known as

CHAPTER 5

a test system in ARMS studies (6×10). Energy loss spectra of the scattered ions for $\theta = 0.9^\circ$ and 1.0° , which were obtained by scanning the ion source voltage are shown in Figure 5.5. The four peaks have previously been explained (5) as follows:

Peak A: Elastically scattered Ar^+ .

Peak B: Excitation of target atoms such as $(3p^4s)$ up to the ionisation limit.

Peak C: Excitation of target atoms to autoionising levels and the production of excited Argon ions.

Peak D: Double ionisation of the target.

Better resolution of the four peaks is obtained by increasing the energy resolution of the MS50 through the use of a smaller β -slit width, as shown in Figure 5.6. Closing the β -slit also changes the relative intensities of the four peaks at the detector because it decreases the angular acceptance of the detector in the yz plane. Changing the z-slit lengths on the MS50 alters the angular acceptance of the detector in the plane of angle analysis (xz) and has a large effect on the observed peak ratios. In Figure 5.7, the intensities of the B and C peaks as a percentage of the total $(A + B + C + D)$ at angles between 0° and 1.5° are plotted for two different source and collector slit lengths. Increasing the angular resolution for example, by using shorter slits increases the minimum angle (θ_{min}) at which a particular process can be observed for example θ_{min} for peak C changes from $\approx 0.6^\circ$ to $\approx 0.8^\circ$ when the post-collision angular resolution is changed from $\pm 0.11^\circ$ to $\pm 0.05^\circ$. These data were acquired with an EI source mounted in the swinging source and therefore the

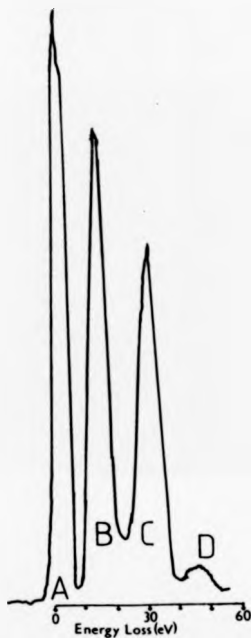


Figure 5.5 The kinetic energy loss spectrum for Argon ions scattered by Argon atoms obtained when $\theta = 0.9^\circ$.

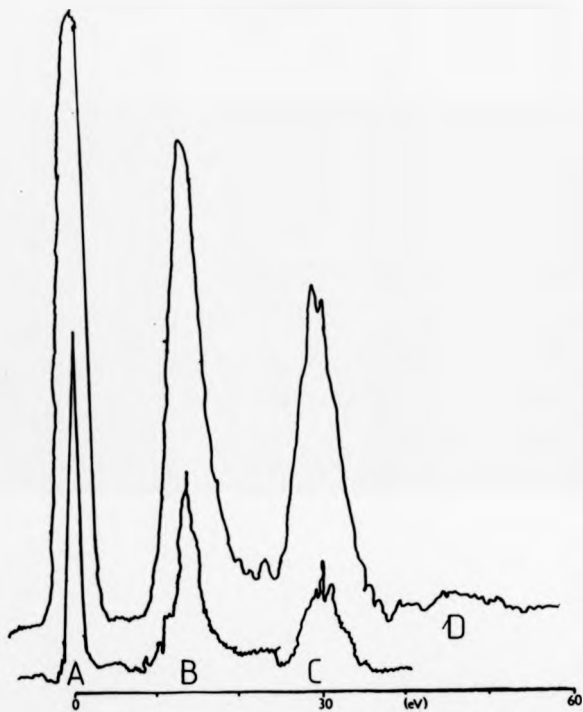


Figure 5.6 Kinetic energy loss spectra for Ar^+ scattered by Ar for $\theta=0.9^\circ$ and β -slit widths of 15 thou (upper) and 5 (lower) thou.

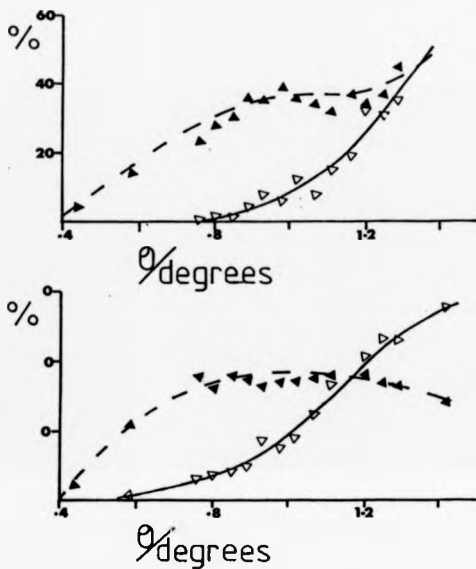


Figure 5.7 The relative intensities of the B Δ and C Δ peaks from Ar^+/Ar scattering as a function of θ at post-collision angular resolutions of $\pm 0.1^\circ$ (lower traces) and $\pm 0.06^\circ$.

CHAPTER 5

S/N ratio is not as good as was obtained when using a CI source. The data in Figure 5.8 were acquired using the CI ion source and relatively good repeatability is shown.

Methanol molecular ions can fragment by the following consecutive reactions:



Only molecular ions which have appreciable internal energy after collisional activation will fragment to give $[\text{COH}]^+$ because the second reaction has a high activation energy. As reported by Hemberger et al. (11-13), therefore this fragment ion increases in abundance relative to $[\text{CH}_2\text{OH}]^+$ as θ increases. The good agreement between the two data sets plotted in Figure 5.9 is notable because these data were acquired on two different days, separated in time by one calendar month, and during this time the ion source was dismantled, cleaned and then reassembled. Evidently the swinging source can be reproducibly aligned and set to produce ions scattered over a particular range of angles.

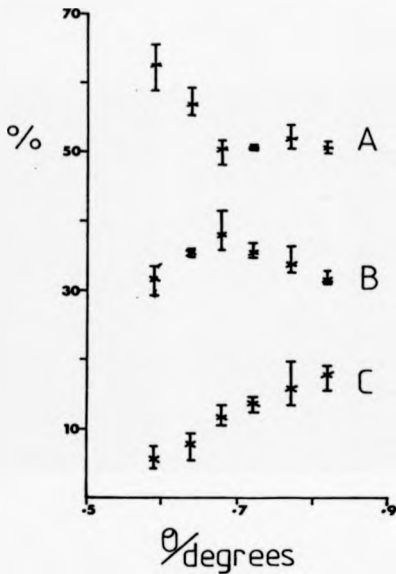


Figure 5.8 Relative intensities of the A, B and C peaks for the scattering of Argon ions by Argon atoms as a function of θ . The crosses show the mean ion abundance (four separate measurements) and the bars indicate the maximum and minimum values obtained at each angle.

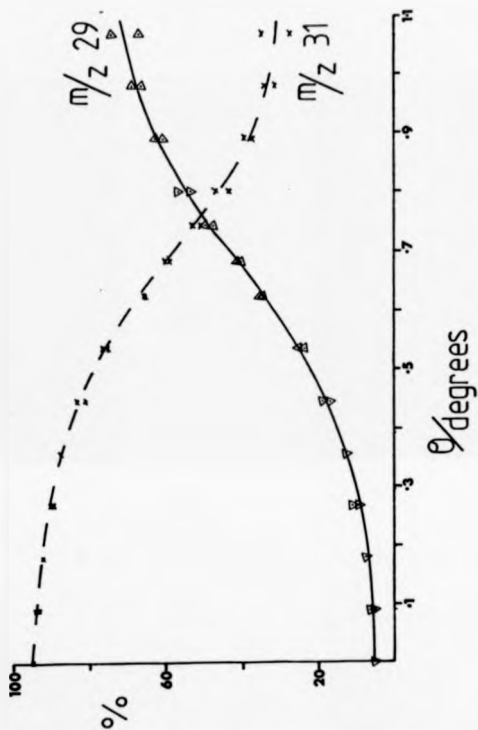


Figure 5.9 Two sets of data showing the variation in the relative abundances of the m/z 29 and m/z 31 fragment ions from methanol as a function of θ .

CHAPTER 5

5.5 REFERENCES

- 1) D.K. Bohme, J.A. Stone, R.S. Mason, R.S. Stradling, K.R. Jennings, *Int. J. Mass Spectrom. Ion Phys.*, **37**, 283 (1981)
- 2) R.S. Stradling, K.R. Jennings, S. Evans, *Org. Mass Spectrom.*, **13**, 429 (1978)
- 3) P.J. Todd, F.W. McLafferty, *Int. J. Mass Spectrom. Ion Phys.*, **38**, 371 (1981)
- 4) G.D. Archard, *Brit. J. App. Phys.*, **5**, 395 (1954)
- 5) M. Barat, J. Baudon, M. Abignola, J.C. Hoover, *J. Phys. B: Atom. Molec. Phys.*, **3**, 230 (1970)
- 6) V. Franchetti, J.J. Carmody, D.A. Krause, R.G. Cooks, *Int. J. Mass Spectrom. Ion Phys.*, **26**, 353 (1978)
- 7) T. Axt, D.T. Terwilliger, R.G. Cooks, J.H. Beynon, *J. Phys. Chem.*, **79**, 708 (1975)
- 8) R.S. Mason, M.J. Farncombe, K.R. Jennings, R.G. Cooks, *Int. J. Mass Spectrom. Ion Phys.*, **43**, 327 (1982)
- 9) R.K. Boyd, E.E. Kingston, A.G. Brenton, J.H. Beynon, *Proc. R. Soc. Lond.*, **A392**, 89 (1984)
- 10) J.A. Laramée, J.J. Carmody, R.G. Cooks, *Int. J. Mass Spectrom. Ion Phys.*, **31**, 333 (1979)
- 11) A.R. Hubik, P.H. Hemberger, J.A. Laramée, R.G. Cooks, *J. Am. Chem. Soc.*, **102**, 3997 (1980)
- 12) J.A. Laramée, P.H. Hemberger, R.G. Cooks, *Int. J. Mass Spectrom. Ion Phys.*, **33**, 231 (1980)

CHAPTER 5

- 13) P.H.Hemberger, J.A.Laramée, A.R.Hubik, R.G.Cooks, *J. Phys. Chem.*, **85**, 2335 (1981)

CHAPTER 6

6.1 INTRODUCTION

With the swinging source in operation, it was now possible to obtain ARMS data on a variety of systems and the experiments were no longer severely limited by the means of data collection as they had been when using the z-deflection method. Data were therefore obtained to determine the usefulness of ARMS in the study of;

- 1) Isomer differentiation from mass spectra.
- 2) The energetics of collisional activation.

6.2 METHANOL

ARMS data on methanol were first published by Laramée et al. (1), who compared their results with CEMS data and calculated breakdown curves. In later papers (2,3) the effect of different target gases on the ARMS data is reported and the authors conclude that the energy deposited in the methanol molecular ion during collisional activation is proportional to $\langle E_w \rangle^2$, where E_w is the translational energy of the ion before the collision. This conclusion is supported by a theoretical discussion and experimental results. These data are critically discussed by Boyd et al. in reference 4 and they conclude that the energy deposited is proportional to $E_w \theta^2$. As mentioned in the previous chapter, ARMS data on methanol obtained using the swinging source were in good agreement with published data. Once this was found to be so, experiments were undertaken to try and answer some of the questions raised by the debate in the literature about ARMS data on methanol.

CHAPTER 6

6.2.1 THE 29/31 FRAGMENT ION RATIO

In reference 3, the authors report a linear relationship between the 29/31 fragment ion ratio (R) and θ^2 , showing a plot of R vs. θ^2 to be a straight line. The same type of plot for data obtained using the swinging source is shown in Figure 6.1 where two sets of points are plotted to show the effect of the translational energy (E_w) of the parent ion before CA on the 29/31 fragment ion ratio. From Figure 6.1 a linear relationship between R and θ^2 exists over the angular range 0.5 to 1.0°, when $E_w = 6.146$ kV (correlation coefficient 0.998), and 0.5 to 0.9°, when $E_w = 7$ kV (correlation coefficient 0.992) but the relationship between E_w and R is not obvious. Therefore the results were replotted as R vs $E\theta^2$ (Figure 6.2a) and R vs $E^2\theta^2$ (Figure 6.2b), and from these plots it is apparent that these data best fit the equation:

$$R = \text{const.} \cdot (E_w\theta)^2 \quad (1)$$

Although the improved linearity of Figure 6.2b over Figure 6.2a is not immediately apparent, statistical analysis of these data gives the following results;

Figure 6.2a : Slope 0.46 ± 0.02

Intercept -0.52 ± 0.09

Correlation Coefficient 0.988

Figure 6.2b : Slope 0.069 ± 0.003

Intercept -0.5 ± 0.07

Correlation Coefficient 0.991

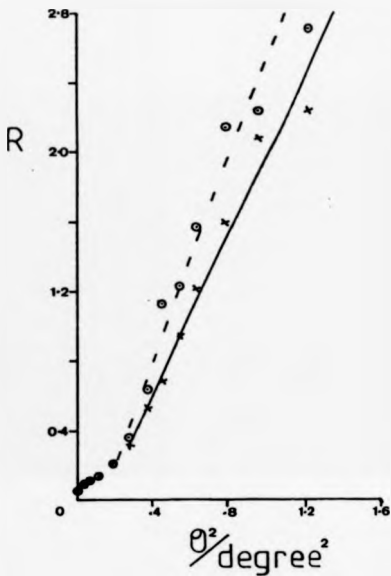


Figure 6.1 The 29/31 fragment ion ratio of methanol (R) as a function of θ^2 at two different ion translational energies (E). For O E_i is 7kV and for x E_i is 6.146kV.

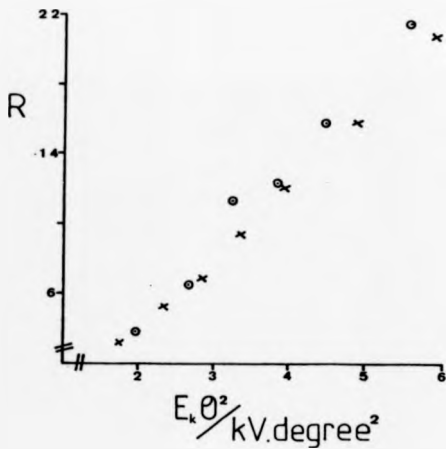


Figure 6.2a The 29/31 fragment ion ratio of methanol (R) as a function of $E_k \theta^2$ at two different ion translational energies (E_t). For \circ E_t is 7kV and for \times E_t is 6.146kV.

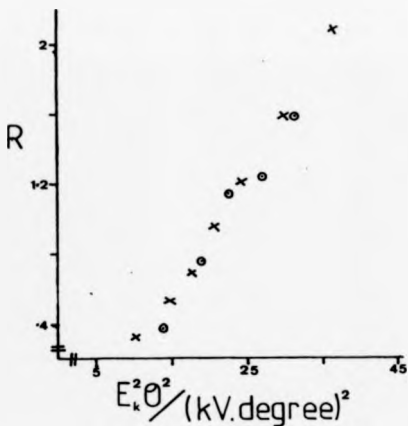


Figure 6.2b The 29/31 fragment ion ratio of methanol (R) as a function of $(E_k \theta)^2$ at two different ion translational energies (E_k). For θ E_k is 7kV and for \times E_k is 6.146kV.

CHAPTER 6

The significance of equation 1 is difficult to evaluate, particularly as its theoretical justification as proposed by Hemberger et al. (3) has been shown by Boyd et al. (4) to contain an error, which if corrected gives;

$$R = \text{const.} = E_0 \theta^2 \quad (2)$$

as the expected relationship. The constant in equations 1 and 2 is presumably in part dependent upon the design of the spectrometer used to acquire the data. In Table 6.1, published ARMS data on methanol are compared to the above data, using the angle at which $R=1$ as a common point of reference.

TABLE 6.1 Values of θ at which the 29/31 fragment ion ratio of methanol is unity obtained by various groups on different designs of mass spectrometer.

Spectrometer	θ	θ^2	$E_0 \theta^2$	$(E_0 \theta)^2$	Coll. Gas
and E_0 in KV	/deg.	/deg. ²	/ kV deg. ²	/(kV) ² deg. ²	
MS50 7	0.68	0.47	3.26	22.8	Argon
MS50 6.1	0.75	0.57	4.64	28.5	Argon
RMB2 7.5	0.54	0.29	2.19	16.4	Argon (a)
MAT212 3	4.95	24.50	73.50	220.5	Argon (b)
MS50 8	0.55	0.31	2.44	19.6	Argon (c)

Note: (a) Taken from reference 3, page 2338.

(b) Taken from reference 5, page 314 and assuming $0.9^\circ/100V$.

(c) Taken from reference 5, page 314 and assuming $1.0^\circ/180V$.

CHAPTER 6

It is immediately obvious from Table 6.1 that the results obtained on the MAT212 do not agree with any other published data. In reference 5 the authors do not comment on the magnitude of θ when $R=1$, but they do suggest that the data is better than previously obtained data for two reasons.

- 1) The data were obtained in a considerably shorter time.
- 2) Better angular resolution.

It follows from equation 1 that, at a constant R , E_{θ} is a constant and data have been published by Hufik et al. (2) to support this idea. Taking the results in the same order as in Table 6.1, E_{θ} for $R=1$ is 4.76, 4.61, 4.05, 14.85 and 4.4. Ignoring the MAT212 data, the remaining results are all consistent with E_{θ} being a constant at a particular value of R .

6.2.2 THE KINETIC ENERGY RELEASE AS A FUNCTION OF θ

The measurement of the kinetic energy released during an ion's fragmentation can be used to estimate the internal energy of the ion after collisional activation, but before it fragments (6). In Figure 6.3, which is based on Figure 59, page 105 of reference 6, some of the thermochemical quantities relevant to the discussion of kinetic energy release are defined. The total kinetic energy release T is given by $T = T^+ + T^-$, where T^+ and T^- are fractions of the non-fixed energy ϵ^+ and the reverse activation energy ϵ^+_0 respectively. It is of particular relevance to this study that T^+ is fixed for a given reaction, whereas T^- is expected to vary with the parent ions excess internal energy and is not an intrinsic property of a reaction.

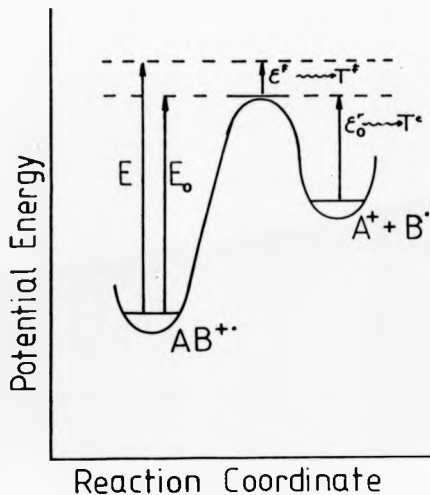


Figure 6.3 The thermochemistry of an ion's dissociation.

E_0 is the minimum energy for dissociation.

E is the internal energy of $(AB)^+$.

T^* is that part of the translational energy release which comes from the non-fixed energy ϵ' .

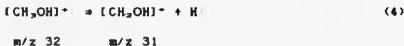
\bar{T}^* is that part of the translational energy release which comes from the reverse activation energy ϵ'_0 .

CHAPTER 6

If ϵ''_0 is negligible then $T = T''$ and T can therefore be related to the excess internal energy ϵ'' . This is expected to be the case for simple bond cleavage reactions and for such reactions Haney and Franklin (7) reported the following empirically determined relationship,

$$T'' = \frac{\epsilon''}{s} \quad (3)$$

where s is the number of oscillators in the parent ion and α is an arbitrary parameter of value 0.44. A more precise equation than 3 has been suggested by Klots (8), but equation 3 is adequate for this discussion. The kinetic energy released during the simple bond cleavage reaction given below has been measured at various values of θ ,



and these data are plotted in Figure 6.4 as T_{ao} vs θ . These data do not indicate that any simple correlation exists between T_{ao} and θ over the entire range of angles studied, but show that T_{ao} is almost linearly related to θ over the range $0.36^\circ < \theta < 0.62^\circ$. One concludes from these results that for $\theta < 0.36^\circ$, increasing θ has a very small effect on the energy deposited during collisional activation E , and therefore ϵ'' is effectively constant. However, at angles greater than 0.36° , E and therefore ϵ'' increase fairly rapidly resulting in a rapid increase in the magnitude of T_{ao} . An obvious consequence of E increasing is that the probability of

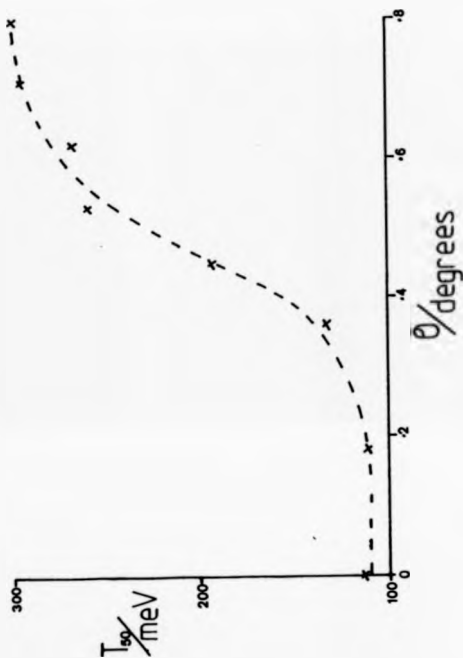
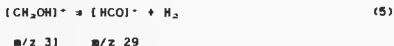


Figure 6.4 T_{\max} as a function of θ for: $[\text{CN}_2\text{OH}]^+ = [\text{CH}_2\text{OH}]^+ + \text{H}$

CHAPTER 6

$[\text{CH}_2\text{OH}]^+$ fragmenting is increased i.e.



This probably explains why the measured kinetic energy release does not continue to increase when $\theta > 0.6^\circ$. Most of the $m/z \ 31$ fragment ions scattered to these angles are presumably detected as fragment ions of $m/z \ 29$ having undergone the reaction described in equation 5 above. In Figure 6.5 the relative abundances of the $m/z \ 31$ & 29 fragment ions are plotted as a function of θ . These data are also consistent with E changing very little below $\approx 0.4^\circ$ and therefore the relative fragment ion abundances are almost constant, but above 0.4° the fragment ion ratio changes very rapidly, consistent with E changing rapidly.

It should be remembered that there exists a direct link between fragment ion abundances as a function of θ and kinetic energy release, as the release of kinetic energy orthogonal to the ion's direction of motion spreads fragment ions over a portion of a sphere, a cross section of which is shown in Figure 6.6. If an ion decomposes at point B then because dissociation is isotropic, the recoil velocity vector v_r can act at any angle between $\pm 90^\circ$ with respect to v_0 which is the mean velocity vector of the ion before dissociation i.e. $-90^\circ < \alpha < 90^\circ$.

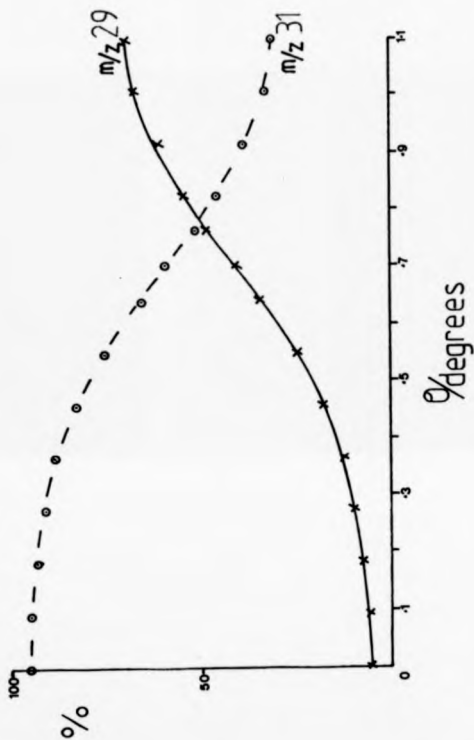
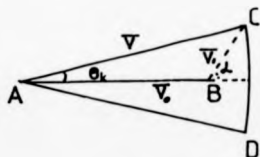


Figure 6.1 The relative abundances of the m/z 31 & m/z 29 fragment ions of methanol as

a function of θ .



$$\tan \theta_k = \left[\frac{(m_1 - m_2)}{m_2} \right]^{\frac{1}{2}} \left[\frac{I}{E_k} \right]^{\frac{1}{2}} \sin L$$

Figure 6.6 The relationship between the centre-of-mass scattering angle due to kinetic energy release (α) and the laboratory angle (θ_k) shown diagrammatically and mathematically.

v_0 is the mean velocity vector of the ion before its dissociation (at point B)

v is the recoil velocity vector

CHAPTER 6

The observed scattering angle due to kinetic energy release θ_o can be calculated using the following relationship (9):

$$\tan \theta_o = \left| \frac{(m_1 - m_2)}{m_2} \right| \left| \frac{T}{E_k} \right| \sin \alpha \quad (6)$$

The maximum deflection of fragment ions due to kinetic energy release $\theta_{o, \text{max}}$ will occur when α is 90° and therefore $\sin \alpha$ is unity. If scattering occurs during collisional activation such that parent ions are deflected through an angle θ_a , then the observed scattering angle of a fragment ion is given by,

$$\theta = \theta_o \pm \theta_a \quad (7)$$

Todd et al. (9) have used equation 6 and others to calculate angular distributions of fragment ions resulting purely from the kinetic energy released during their formation and assuming no scattering during collisional activation i.e. by assuming that $\theta = \theta_o$ and $\theta_a = 0$. By this means they were able to duplicate some of the experimental results reported by Cooks and various co-workers. The calculations used T values calculated from the fragment ion peak width at half height i.e. T_{50} , and using no angular selection. These calculations were extended by Boyd et al. (10) to allow for a distribution of kinetic energy release values based upon measurements of peak widths at 22% of peak height (giving T' - the most probable value) and near the baseline (giving T_m - the maximum value). When equation 6 is applied to the data in Figure 6.4, the divergence of the fragment ion beam due to the kinetic energy release $\theta_{o, \text{max}}$ can be calculated and the results are given

CHAPTER 6

in Table 6.2.

Table 6.2 $\theta_{L,max}$ as a function of T_{eo} for m/z 32 & 31 in methanol

T_{eo} /meV	$\theta_{L,max}$ /degrees	T_{eo} /meV	$\theta_{L,max}$ /degrees	T_{eo} /meV	$\theta_{L,max}$ /degrees
113	± 0.04	111	± 0.04	134	± 0.05
195	± 0.06	259	± 0.07	267	± 0.07
296	± 0.07	299	± 0.07		

For this fragmentation reaction $\theta_{L,max}$ is fairly small but because it changes with θ , it is difficult to determine how the abundance of the fragment ion varies with the scattering angle. When looking at the ratio of the abundances of two fragment ions as a function of θ the situation is even more complicated, since it is unlikely that the kinetic energy release associated with the formation of the two fragment ions will be identical. The divergence of the fragment ion beams will therefore be different. Indeed this fact is fundamental to the idea that variations in fragment ion ratios as a function of θ can be calculated from kinetic energy release values alone assuming no scattering of the parent ion during collisional activation. In reference 10 calculated fragment ion abundances as a function of θ are reported for the m/z 31 and 29 fragment ions of methanol. These were computed using the following kinetic energy release values which

CHAPTER 6

were determined from ions collected over a wide range of angles and therefore represent an attempt to allow for variations in T with θ :

$m/z\ 32 = 31$: $T' = 0.56\text{eV}$ and $T_{\infty} = 3.3\text{eV}$

$m/z\ 32 = 29$: $T' = 2.0\text{eV}$ and $T_{\infty} = 5.5\text{eV}$

The importance of averaging out such variations depends in part upon how different the angular variation in T is for the different fragment ions. In Figure 6.7, T_{∞} for $m/z\ 32 = 29$ is plotted as a function of θ and it is apparent that T_{∞} is only slightly dependent upon θ , which is in marked contrast to the data in Figure 6.4. Once again the divergence of the $m/z\ 29$ fragment ion beam due to kinetic energy release alone can be calculated from equation 6.

Table 6.3 $\theta_{L, \text{max}}$ as a function of T_{∞} , for $m/z\ 32 = 29$ in methanol

T_{∞} /meV	$\theta_{L, \text{max}}$ /degrees	T_{∞} /meV	$\theta_{L, \text{max}}$ /degrees	T_{∞} /meV	$\theta_{L, \text{max}}$ /degrees
512	± 0.17	533	± 0.17	533	± 0.17
561	± 0.18	561	± 0.18	567	± 0.18
526	± 0.17	550	± 0.17		

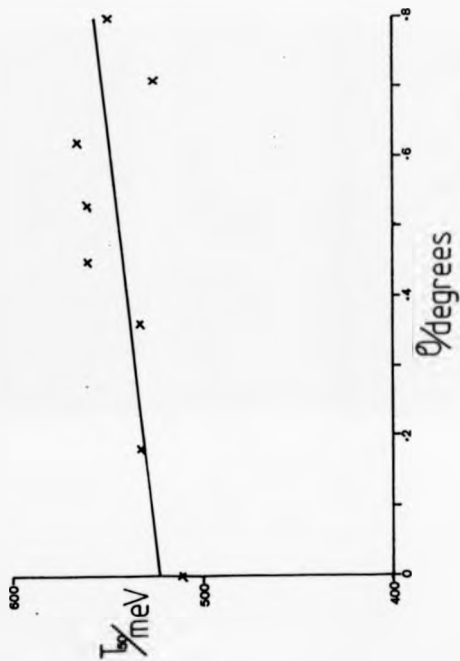


Figure 6.7 T_m as a function of θ for: $[\text{CH}_3\text{OH}]^- = [\text{HCO}_3]^- + \text{H}^+ + \text{H}_2\text{O}$.

CHAPTER 6

In reference 10, the authors note that for two competing fragmentation reactions,



the angular distributions of the two fragment ions will be similar if,

$$\frac{T_F}{T_{F'}} = \frac{m'_{N'} m_N}{m_N m'_{F'}} \quad (8)$$

If N is m/z 32, F is m/z 31 and F' is m/z 29, then using T_m values the ratio $T_F/T_{F'}$ can be calculated as a function of θ , i.e.

Table 6.4 The variation in the ratio of the kinetic energy releases for m/z 32 \rightarrow 31 and 32 \rightarrow 29 as a function of θ .

$\theta/\text{degrees}$	0	0.18	0.36	0.45	0.53	0.62	0.71	0.80
$T_F/T_{F'}$	0.29	0.25	0.28	0.36	0.43	0.44	0.57	0.53

Beynon and co-workers predict a cross-over in the 29/31 fragment ion ratio at 0.11' from calculations of fragment ion abundances using a constant $T_F/T_{F'}$ ratio of 0.6. This is a much smaller angle than that determined experimentally (see Table 6.1) and the difference may in part be explained by Table 6.4. As the kinetic energy release ratio increases, the angle at which the fragment ion abundances become equal decreases. By using a ratio which is higher than that found experimentally therefore, the calculated

CHAPTER 6

angle for the cross-over is lowered. Calculations of fragment ion abundances as a function of θ also assume a constant kinetic energy release distribution with θ . In order to check the validity of this assumption the width of the m/z 29 and 31 fragment ion peaks were measured at 50% peak height, 22% peak height and at their base and T_{50} , T_{22} and T_{base} values were calculated. Plots of the ratios T_{22}/T_{50} and T_{base}/T_{50} as functions of θ for the two fragment ions are given in Figure 6.8. These data show that the peak shape and therefore $f(T)$ is invariant with θ for m/z 32 \rightarrow 29, but not for m/z 32 \rightarrow 31. Interestingly, at large θ , the peak shapes and kinetic energy release distributions for both fragment ions are identical. The change in peak shape shown in Figure 6.8 is seen as a broadening of the peak which suggests that the average kinetic energy release is increasing, a not unexpected result of increased energy deposition during collisional activation.

Data were also obtained for the collision induced dissociation of m/z 31 ions to m/z 29 ions where the parent ions were formed inside the ion source. This fragmentation reaction also occurs in the absence of collision gas and is accompanied by a large release of kinetic energy giving a dish shaped peak because of z-axial discrimination in the spectrometer (6,11,12). It is one of only a few reactions for which the kinetic energy released during unimolecular dissociation is reduced when the parent ion has been collisionally activated; the converse is normally observed. Other examples of this are H_2 loss from the M^+ and $(M+H)^+$ ions of methanol (13). This difference from the usual behaviour has been

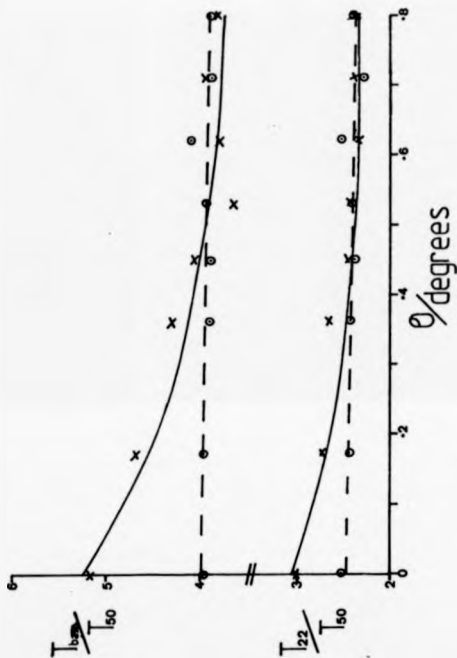


Figure 6.8 $T_{1,2,3...}/T_{100}$ and T_{22}/T_{150} as a function of θ for m/z 32 \times m/z 31 \circ and m/z 32

\times 29 \circ Iron methanol.

CHAPTER 6

explained by assuming that the collisionally activated ion dissociates from a different electronic state (6). Alternatively it may indicate that different products are formed under low and high energy conditions; eg hydrogen loss from the methanol molecular ion has been shown to give H-C-OH^+ at low energies and $\text{H}_2\text{C=O}^+$ at higher energies (14).

A composite peak was obtained for m/z 31 + m/z 29 at $\theta=0^\circ$ (Figure 6.9), the collision induced component sitting inside the horns of the unimolecular component and both components being of comparable intensity. This explains why, when T_{90} is plotted as a function of θ (Figure 6.10), the zero angle value is larger than for any other angle. Once again T_{90} for the reaction varies only slightly with θ and the data in Figure 6.11 show that the shape of the collision induced component is invariant with θ . It was also possible to look at the shape of the peak in the absence of collision gas as a function of θ for angles between 0° and 0.36° , and the T_{90} , T_{22} and T_{999} data are plotted in Figure 6.12. The peak became progressively more Gaussian in appearance as θ increased and the magnitude of all three kinetic energy release measurements was reduced. If a peak shape changes with θ then it may be an example of the effect of discrimination on ARMS data, a subject which is discussed in greater detail in later chapters of this thesis. Consider a fragment ion peak produced by scanning the accelerating voltage (V) of a mass spectrometer. The peak profile in such a scan is a record of the number of ions having a particular kinetic energy. At the extreme edges of the peak fragment ions which have gained and lost the maximum amount of

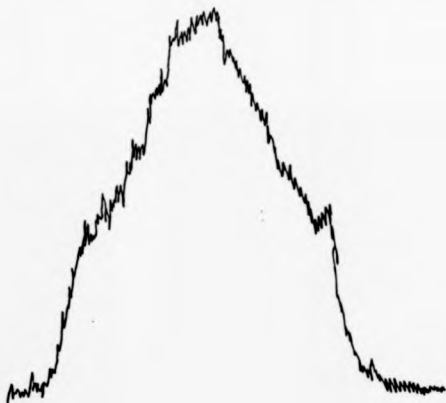


Figure 6.9 The shape of the fragment ion peak for m/z 31 \leftarrow m/z 29 for methanol at $\theta = 0^\circ$ obtained by scanning the source voltage (V).

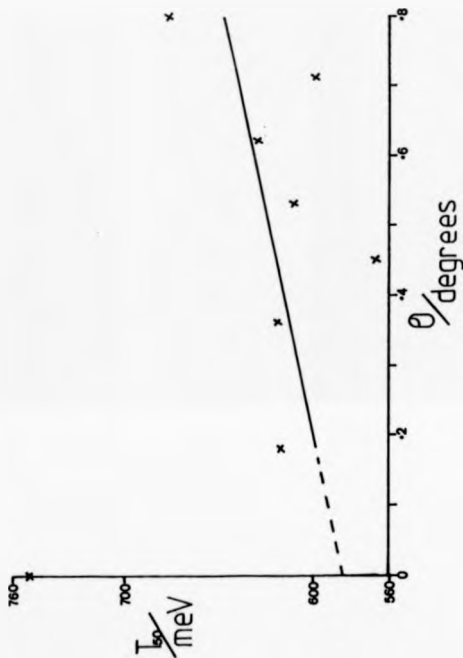


Figure 6.10 T_{50} as a function of θ for $[\text{CH}_3\text{OH}]^+ + [\text{HCO}]^+ + \text{H}_2\text{O}$.

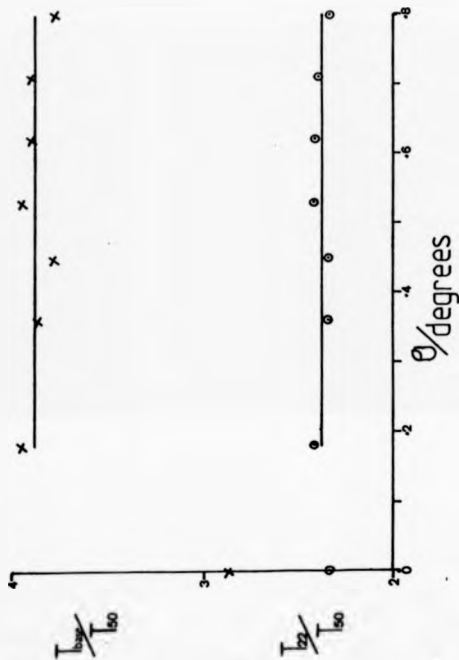


Figure 6.11 T_{000}/T_{∞} and T_{22}/T_{∞} as a function of θ for $[\text{CH}_3\text{OH}]^+ = [\text{HCO}]^+ + \text{H}_2$.

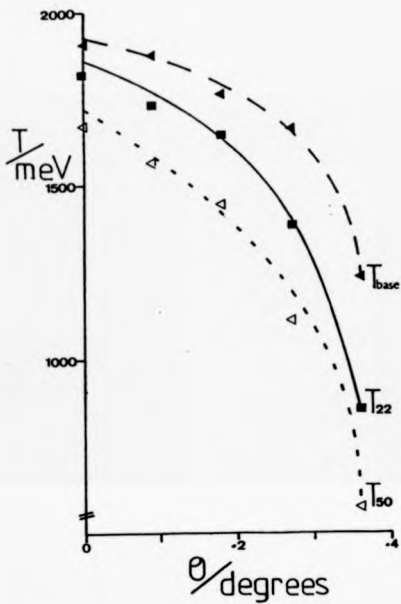


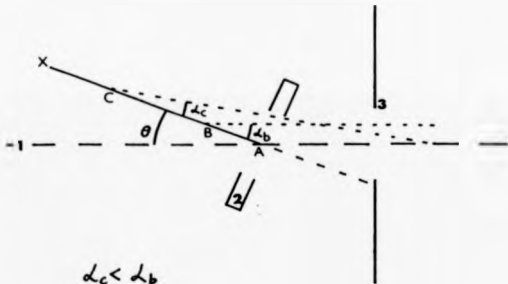
Figure 6.12 T_{base} , T_{22} and T_{50} as a function of θ for the unimolecular reaction: $[CH_2OH]^+ + [HCO]^+ \rightarrow H_2$.

CHAPTER 6

kinetic energy relative to the parent ion have been detected. For these fragment ions $\alpha = 0^\circ$ (see Figure 6.6) i.e. v_i acts in the same direction as v_0 , either adding to or subtracting from it. The fragment ions detected at the centre of the peak are those for which $\alpha = \pm 90^\circ$. Figure 6.13 shows the swinging source at an angle θ with respect to the the central ion optical axis of the spectrometer. Fragment ions produced while an ion is moving along XA, will not be detected if $\alpha = 0$ because they will not pass through the source z-restrictor. Obviously α for a fragment ion formed at point C must be smaller than for fragment ions formed at points A and B if it is to be detected. Hence the detection of fragment ions produced outside the collision chamber, will increase the intensity of the fragment ion peak more at its centre than at its edges. As θ increases the range of θ_i values which result in fragment ions being detected decreases and therefore the fragment ion peak becomes narrower. This discrimination effect will only be noticeable in ARMS studies of collisional activation if an appreciable percentage of the fragment ions are formed outside the collision chamber and could be ignored if the collision chamber were floated (see Chapters 7 and 8 of this thesis).

6.2.3 FRAGMENT ION ABUNDANCES AS A FUNCTION OF COLLISION GAS PRESSURE

A number of groups (15,16) have developed methods of calculating fragment ion yields as a function of collision gas pressure and compared the results with experimental data on the

**KEY**

- 1) Central ion optical axis of the mass spectrometer.
- 2) Collision chamber.
- 3) Source z-restrictor.

Figure 6.13 Schematic diagram of the swinging source at an angle θ , showing how fragment ions produced by parent ions decomposing along XA will not be detected if $\alpha = 0^\circ$. The maximum possible value of α which will produce fragment ions that are detected increases on moving from X to A.

CHAPTER 6

collision induced decomposition of e.g. methane. A detailed discussion of the methods used is not relevant to this study but the general conclusions are of interest. As the pressure inside a collision chamber increases, the probability that ions will undergo multiple collisions increases. In reference 17, Kim calculates that for ions of collision-cross section $5 \times 10^{-16} \text{ cm}^2$, traversing a 1cm collision cell, if the collision gas pressure is set to give 90% transmission of the incoming ion beam then 95% of these ions undergo single collisions. When the gas pressure is raised by a factor of five however, the beam is reduced to 60% of its original intensity and double and triple encounters then make up 20% and 5% of the collision events respectively. The best ARMS data will be obtained under single collision conditions since unless all collisions result in scattering in the same direction any relationship between scattering angle and energy deposition will be blurred by successive collisions.

Data were obtained on the pressure dependence of the parent and of some of the daughter ion abundances of methanol at $\theta = 0.09^\circ$ and $\theta = 0.53^\circ$ and these are presented as plots of $\log_{10} I$ vs P in Figures 6.14 to 6.17. The same scale is used in all four figures. Considering first the data in Figure 6.14 for the methanol molecular ion, the $\theta = 0.09^\circ$ data shows the expected exponential decrease in ion intensity with increasing gas pressure. The off-axis data is consistent with increasing the gas pressure making it more likely that ions will be scattered and the fall in the number of intact molecular ions detected at $P > 6.5 \times 10^{-7}$ torr suggests that:

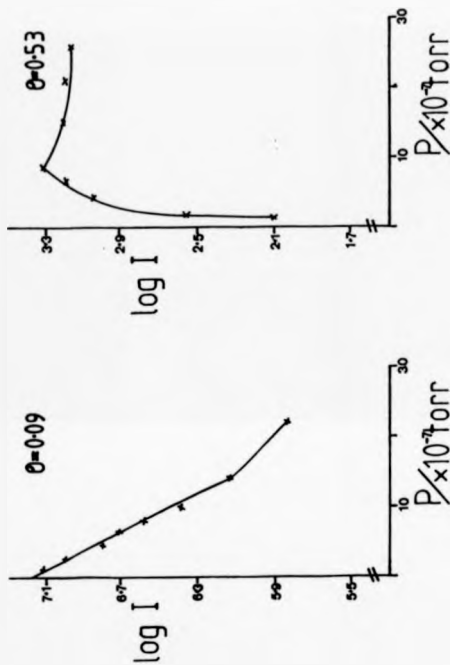


Figure 6.14 The log... of the abundance of the methanol molecular ion as a function of collision gas pressure at two different values of θ .

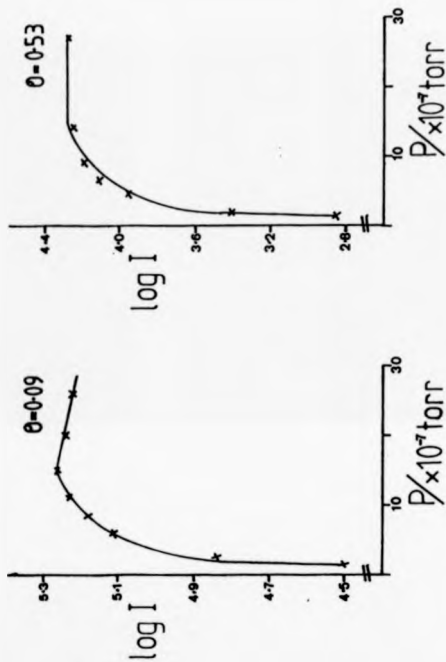


Figure 6.15 The \log_{10} of the abundance of m/z 32 = m/z 31 from methanol as a function of collision gas pressure at two different values of θ .

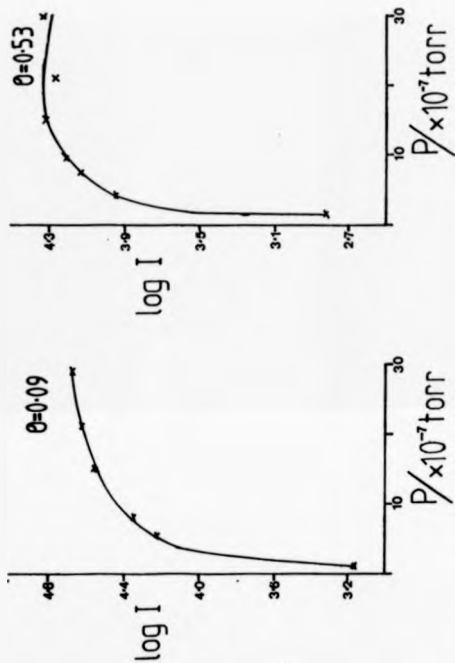


Figure 6.16 The \log_{10} of the abundance of m/z 32 = m/z 29 from methanol as a function of collision gas pressure at two different values of θ .

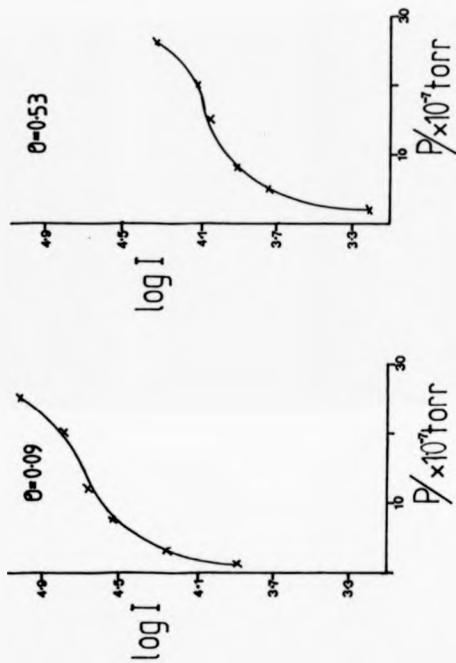


Figure 6.17 The \log_{10} of the abundance of m/z 31 = m/z 29 from methanol as a function of collision gas pressure at two different values of θ .

CHAPTER 6

- 1) More ions are being scattered to angles $> 0.53^\circ$.
- 2) More of the scattered ions are gaining enough energy during collisional activation to cause them to dissociate and are therefore being detected as daughter ions.

Both of these mechanisms are made more probable by the increasing number of multiple collisions which occur at high collision gas pressures. These data also make it unlikely that angle resolved mass spectra can satisfactorily be explained without allowing for scattering during collisional activation i.e. $\theta_0 \neq 0^\circ$. All the daughter ion pressure plots exhibit a steeper rate of increase of $\log_{10} I$ with P when θ is 0.53° , because collision gas is not only required to activate the parent ions so that they dissociate to the appropriate daughter, but also to scatter the parent ion. Therefore,

$$0.53^\circ = \theta_0 + \theta_0$$

(9)

Equating increasing collision gas pressure with increasing energy deposition during collisional activation i.e. E proportional to P , allows the other features of note in Figures 6.15 to 6.17 to be explained. From the breakdown curve for methanol (18) the fragmentation reaction of lowest activation energy is m/z 32 \rightarrow 31, and above a certain P , and therefore E , it is reasonable to expect that reactions of higher activation energy will cause m/z 31 to fragment further and therefore the intensity of m/z 31 will decrease. This drop in fragment ion intensity at high P is not observed however, when $\theta = 0.53^\circ$. Both plots in Figure 6.17

CHAPTER 6

exhibit an upward break in the intensity of m/z 31 \rightarrow 29 when $P > 2 \times 10^{-8}$ torr, presumably indicating the onset of a new process leading to the m/z 29 daughter ion (19).

6.3 o & p-XYLENES

The use of the kinetic energy release (T) associated with the formation of a particular fragment ion to distinguish between isomeric parent ions has been reported for a number of different organic chemicals (6,20). By studying T as a function of θ and therefore E it should be possible to identify processes which have identical T values when parent ions having a wide range of internal energies are sampled.

6.3.1 KINETIC ENERGY RELEASE FOR $M = (M-15)$ AS A FUNCTION OF θ

Raynon et al. (21) were able to distinguish between the three isomeric forms of xylene by measuring the kinetic energy released during photodissociation of the molecular ion to give $(M-15)^+$, as a function of photon energy. Plots of T (calculated using peak widths at 10% peak height) against photon energy show that $T_{10\%}$ for the para isomer falls rapidly as the photon energy is increased, making it easy to distinguish from the ortho and meta isomers. The plots for the latter isomers are very similar but, at the highest photon energy used for the experiments (3.47 eV), $T_{10\%}$ for the ortho isomer is significantly greater than for the meta. As the greatest differences had been observed between the para isomer and either the meta or ortho isomers, $T_{10\%}$ was determined for the ortho and para isomers as a function of θ

CHAPTER 6

and the results are plotted in Figure 6.18. In comparing this data with the photodissociation results in reference 21, the following is immediately apparent;

- 1) The ARMS data encompasses a wider range of T values and hence presumably a wider range of e^+ .
- 2) The kinetic energy release values increase with θ but decrease with increasing photon energy. The ARMS data are therefore consistent with those obtained for other fragmentations e.g. methanol, etc., and with the premise that increased energy deposition E with θ leads to a greater excess internal energy e^+ and therefore larger T^+ . Why a similar trend is not observed when the photon energy is increased is not commented upon by the authors of reference 21. The same group however have found that T for photoinduced methyl loss from the molecular ion of anisole decreases as the photon energy increases (20). This is explained either as resulting from increased retention of internal energy by the fragment ion or loss of energy by e.g. photon emission.
- 3) The ortho and para isomers cannot be distinguished from each other from the ARMS data.

The differences between the two data sets could be explained if the ARMS data had superimposed upon them an instrumental artifact which obliterated the different behaviours of the two isomers or if before or during collisional activation the ortho and para molecular ions were converted to a common structure.

Addressing the former point first, as mentioned earlier in this chapter, fragment ions formed either side of the collision chamber

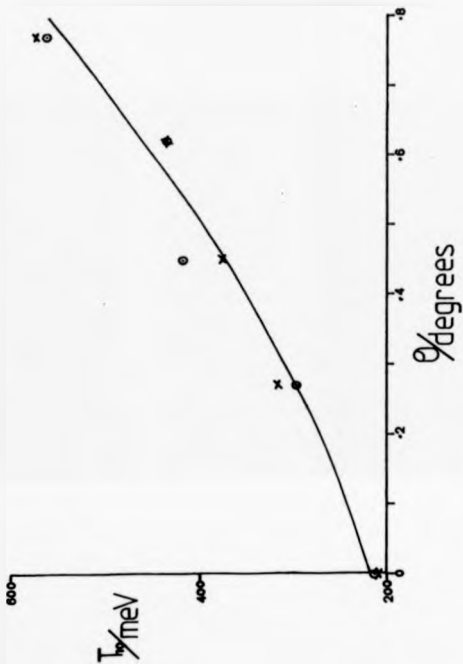


Figure 6.18 T_{100} for the fragment ion formed by loss of methyl from the molecular ions of ortho- (x) and para- (o) xylene as a function of θ .

CHAPTER 6

i.e. from unimolecular dissociations, are detected at low θ but not at higher values of θ . The ratio of metastable to collision induced fragment ions depends upon the system under study and is only likely to affect ARMS data if it is greater than eg 5:1 when $\theta = 0^\circ$. The ratio can be determined when the collision chamber is floated at a known voltage because this causes the products of unimolecular dissociations (occurring outside the collision chamber) and collision induced dissociations (occurring inside the collision chamber) to have different coordinates on the BE plane. Using a floating collision chamber on the swinging source is discussed in more detail in Chapters 7 and 8 and the m^*/CID ratio for p-xylene is plotted in Figure 6.19 as a function of θ . These data clearly show that at low values of θ the $T_{1,0}$ values reported in Figure 6.18 will contain significant contributions from unimolecular dissociations, for which $T_{1,0}$ is approx. 131meV (single determination at $\theta=0^\circ$). As θ increases the composite $T_{1,0}$ value will increase because of the decrease in the contribution made by fragment ions from unimolecular dissociations. This effect is not expected to be isomer dependent however and should not prevent isomer differentiation based upon different $T_{1,0}$ vs θ curves for the isomers.

Isomer conversion to a common structure may therefore be the explanation for the differences between the photodissociation and ARMS data. As the normal collision induced spectra for the isomers are identical (21), adding limited energy resolution to the method, i.e. ARMS, will only allow the isomers to be distinguished if E_{a-0} is $<$ the critical energy for isomerisation

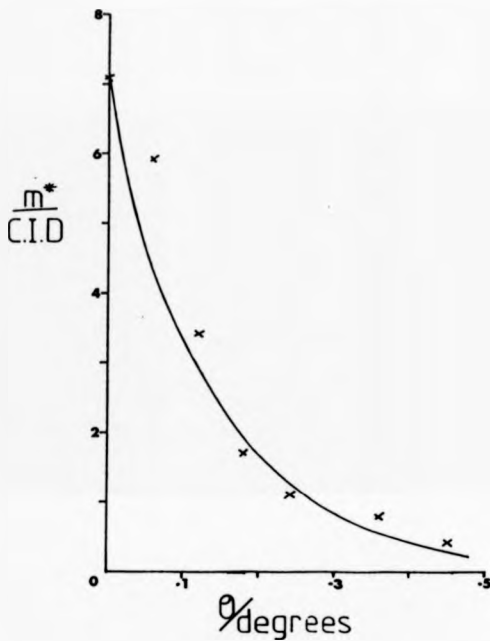


Figure 6.19 The m^*/CID ratio for methyl loss from the molecular ion of p-xylene as a function of θ .

of the isomers to a common structure.

6.4 BREAKDOWN CURVES OF C₂H₂ ISOMERS

One suggested use of ARMS is as a quick and easy means of obtaining breakdown curves which are plots of the relative abundances of the molecular and fragment ions as a function of internal energy. Convolution of the breakdown curves with the internal energy distribution gives the mass spectrum. A number of methods exist for obtaining breakdown curves, including:

- a) From electron impact mass spectra by calculating the second derivative of the ion current for each fragment ion as a function of the electron energy and normalising the individual curves (22).
- b) By direct calculation from QET (23,24).
- c) From the first derivative of the photoionization efficiency curve (25).
- d) From charge exchange mass spectra (26).
- e) From photoelectron-photoion-coincidence spectroscopy (27).

Comparisons between ARMS data and the results from the aforementioned techniques have often been used by Cooks and his numerous co-workers to try and establish a connection between 0 and E. Without exception the systems studied have contained at most only four fragment ions and therefore the number of fragment ion intensity crossover points in the curves has been limited. These crossover points can hopefully be used to calibrate the energy/angle scale of the ARMS data.

CHAPTER 6

6.4.1 CYCLOHEXANE

Breakdown curves for fourteen C_6H_{12} isomers have been published by Herman et al. (28), from their own charge exchange data. Initially ARMS data were obtained for cyclohexane and compared to these results. In Figure 6.20 the angle resolved mass spectra obtained when θ is 0° and 0.53° are compared to charge exchange mass spectra reconstructed from the breakdown curves in reference 28. Both methods yield data which exhibit the following trends:

- 1) As the internal energy of the molecular ion increases, the loss of alkyl groups by simple cleavage reactions predominates over rearrangement reactions involving alkene elimination, e.g. m/z 55 is more intense than m/z 56 and m/z 41 is more intense than m/z 42.
- 2) The abundances of the low mass fragment ions increase as the internal energy of the molecular ion increases.

One difference between CEMS and ARMS is that the former technique directly gives information about the energy dependence of the molecular ion abundance, which cannot be elicited from ARMS studies. The validity of breakdown curves generated from CEMS studies is not in doubt but a critical assessment of the ARMS results will now be undertaken.

When considering the complete breakdown curve, Figure 6.21, the first problem as mentioned above is to calibrate the E/θ axis. One possible method is to note E values at which two of the fragment ion abundances are equal in the CEMS data and find the corresponding values of θ from Figure 6.21. This is shown in

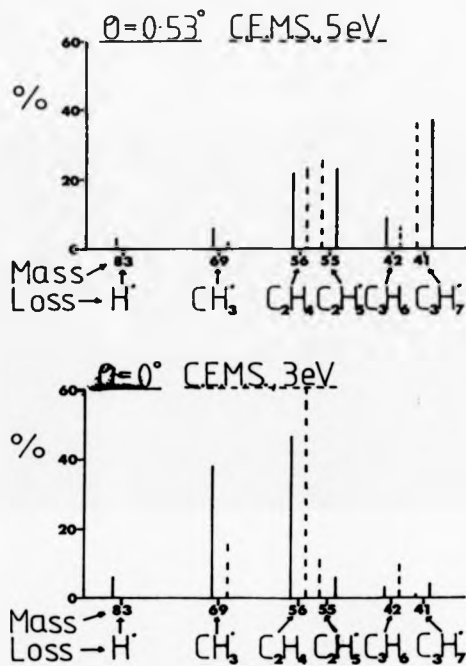


Figure 6.20 ARMS spectra at 0° and 0.53° compared to CEMS data obtained using internal energies of 3 and 5eV.

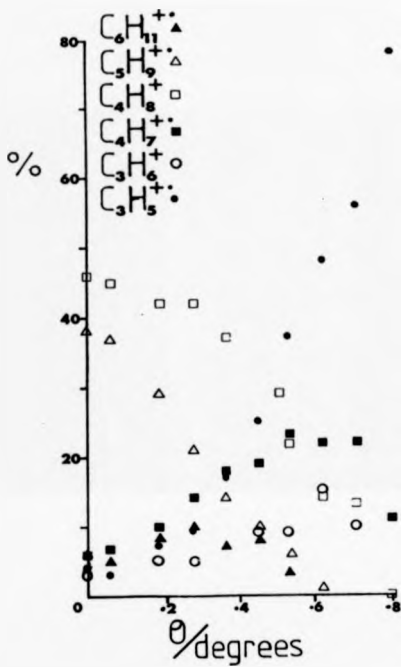


Figure 6.21 Fragment ion abundances of cyclohexane as a function of θ .

CHAPTER 6

Table 6.5 (peak height data).

TABLE 6.5 Comparison of fragment ion abundance crossover points in CEMS and ARMS results.

Fragment Ions	E/eV	$\theta/^\circ$	
		Pk. Ht.	Pk. Area
a) $[C_3H_6] \equiv [C_4H_7]$	2.75	0.77	0.77
b) $[C_6H_9] \equiv [C_4H_7]$	3.25	0.35	0.25
c) $[C_3H_6] \equiv [C_3H_6]$	3.7	0.08	<0 (1)
d) $[C_6H_9] \equiv [C_3H_6]$	3.75	0.48	0.34
e) $[C_4H_8] \equiv [C_3H_6]$	4.7	0.49	0.38
f) $[C_4H_8] \equiv [C_4H_7]$	4.85	0.57	0.47

Note: (1) If extrapolated to negative angles, the ion abundance curves would probably cross at approx. -0.1° .

Converting θ to E from the peak height data in Table 6.5 is obviously difficult, as some of the crossover points seem to contradict the others, however $\theta=0^\circ$ seems to correspond to an internal energy of approximately 3eV. As previously noted crossover points will be shifted if one of the two fragment ions contains a significant contribution from metastable decompositions e.g. b and d ($[C_6H_9]$ is formed mainly by unimolecular dissociations at low values of θ see Figure 8.3, Chapter 8).

Another factor which may have a large bearing on the angles at

CHAPTER 6

which crossover points are observed is the kinetic energy release which accompanies the formation of fragment ions and leads to ions which have been scattered to the same initial angle θ_u being detected over a range of angles given by $(\theta_u + \theta_{L_1}) \pm \delta$ ($\theta_u - \theta_{L_1}$) (Figure 6.6). The fragment ions can be thought of as being evenly distributed over a sector of a sphere. The surface area of this sector is a fraction of the surface area of the sphere proportional to θ_u . If two fragment ions have the same abundance but different values of θ_u then the ion's abundance per unit area of the sector will be different. As the ions being detected by the spectrometer are those which lie on a section of the sector produced by the projection of the slit dimensions onto it the heights of the peaks in a scan are not a measure of the ions' relative abundances, unless θ_u is the same for both fragments. If the peak heights are multiplied by θ_u , then the resulting intensity may be a better approximation to the desired quantity. Equation 9 can be used to calculate a maximum value of θ_{L_1} , although obviously a distribution of θ_u values exists since the kinetic energy release is not a single value for each fragmentation:

$$\tan \theta_{L_1, \max} = \left| \frac{(E_u - E_{L_1})}{E_p} \right|^{1/2} \left| \frac{T}{E_u} \right|^{1/2} \quad (9)$$

Before looking in detail at the cyclohexane results a few observations arising from the form of equation 9 will be discussed. Consider an ion of mass 100 daltons, having a kinetic energy of 7000 electron volts before it fragments. Using equation 9 $\theta_{L_1, \max}$ can be calculated as a function of T for losses

of for example 15, 29 and 43 daltons, i.e. loss of methyl, ethyl and propyl groups (Figure 6.22). It can be seen that for a given value of T , the smallest daughter ions are deflected the most and will, therefore, be observed at the largest angles. In Figure 6.23 the variation in θ_{max} as a function of m_2 is plotted for two different values of T , showing that for small fragment ions θ_{max} is strongly dependant upon the magnitude of T , but for large values of m_2 , changes in m_2 have the largest effect upon θ_{max} .

Graphs of T_{BO} vs θ were plotted (Figures 6.24 & 6.25) from single determinations of T_{BO} for the formation of the major fragment ions of cyclohexane at $\theta = 0, 0.18^\circ, 0.36^\circ, 0.53^\circ$ and 0.71° and used to estimate T_{BO} at the required values of θ . θ_{max} was then calculated using equation 9 (Table 6.6, overleaf).

When the ion abundance data in Figure 6.21 were multiplied by the appropriate θ_{max} values, the breakdown curves in Figure 6.26 were obtained. Figures 6.21 and 6.26 are qualitatively very similar, but not identical as shown by the differences in crossover points evident from Table 6.5. The 'peak area' data are more directly comparable to the CEMS results, but still contains sufficient differences to make calibrating θ directly in terms of E , very difficult.

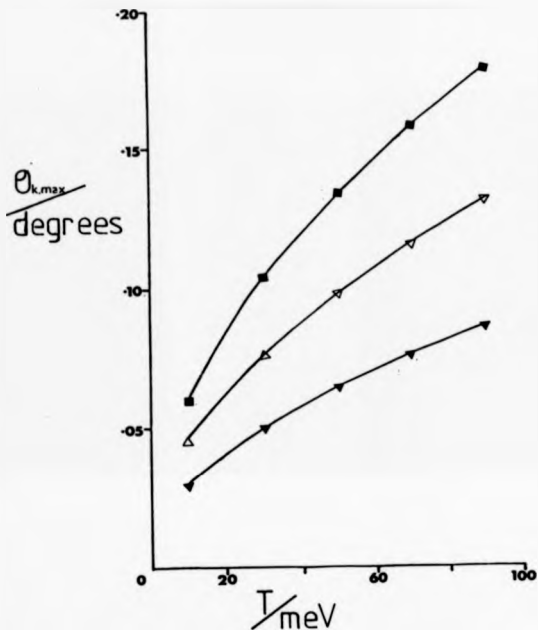


Figure 6.22 $\theta_{k,max}$ as a function of T for a parent ion of mass 100 mass units losing 43 (top trace), 29 (middle trace) and 15 mass units (bottom trace).

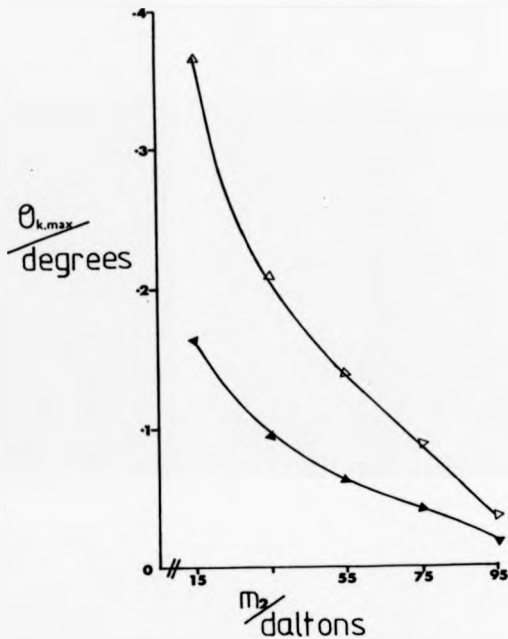


Figure 6.23 $\theta_{k,max}$ as a function of daughter ion mass for a parent ion of 100 mass units with T fixed at 10 meV (lower trace) and 50 meV (upper trace).

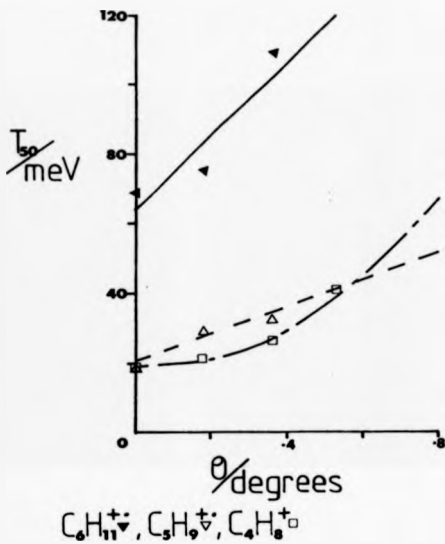


Figure 6.24 $T_{0.5}$ as a function of θ for three fragment ions from cyclohexane.

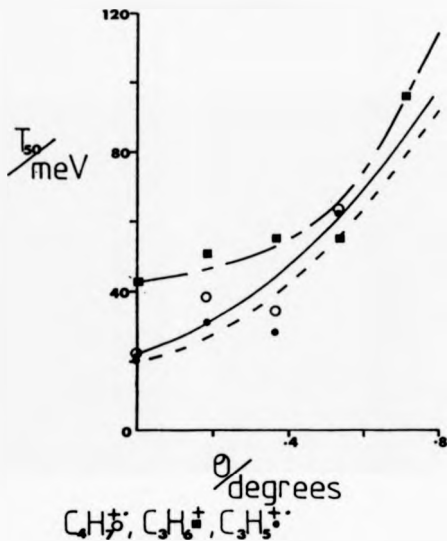


Figure 6.25 T_{90} as a function of θ for three more fragment ions from cyclohexane.

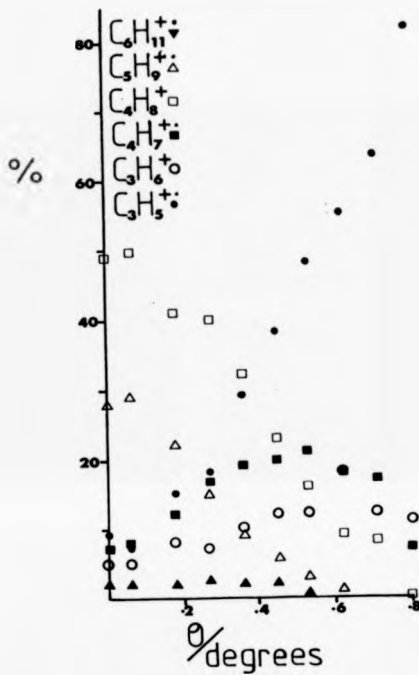


Figure 6.26 Corrected (as described in the text) fragment ion abundances of cyclohexene as a function of θ .

CHAPTER 6

TABLE 6.6 T_{90} and θ_{90} for the major fragment ions of cyclohexane at different values of θ .

θ	$T_{90}(\text{meV})/\theta_{90} (^{\circ} \times 10^3)$					
m/z	83	69	56	55	42	41
0	64/ / 19	21/ / 46	19/ / 67	22/ / 74	20/ / 97	44/ /147
0.06	70/ / 20	23/ / 48	19/ / 67	23/ / 75	21/ / 99	45/ /148
0.18	83/ / 22	28/ / 53	20/ / 68	28/ / 83	24/ /106	47/ /151
0.27	92/ / 23	31/ / 56	23/ / 73	34/ / 92	28/ /115	49/ /155
0.36	102/ / 24	34/ / 59	27/ / 80	42/ /101	36/ /130	51/ /158
0.45	111/ / 25	38/ / 62	32/ / 87	51/ /112	47/ /148	55/ /164
0.53	120/ / 26	41/ / 65	38/ / 94	60/ /122	61/ /169	60/ /171
0.62		44/ / 67	46/ /104	70/ /132	77/ /190	71/ /186
0.71		48/ / 70	56/ /115	81/ /141	94/ /210	89/ /208
0.80		51/ / 72	66/ /124	91/ /150	111/ /228	114/ /236

CHAPTER 6

6.4.2 TWO ISOMERIC PENTENES

Data were also obtained on two other of the compounds studied by Herman et al. (28), namely 2-methyl-1-pentene and 2-methyl-2-pentene. The CEMS breakdown curves for them agree with metastable ion spectra and normal mass spectra in that the 1-olefin shows dominant fragmentation to $[C_4H_9]^+$, while the 2-olefin shows dominant fragmentation to $[C_3H_7]^+$. The large differences between the breakdown curves are also evident in the limited ARMS data in Table 6.7.

TABLE 6.7 Fragment ion ratios at three values of θ .

Isomer	Ratio of $[C_4H_9]^+$ to $[C_3H_7]^+$ to $[C_2H_5]^+$		
	$\theta = 0^\circ$	0.30°	0.59°
1-olefin	05:92:03	13:82:05	11:48:41
2-olefin	91:02:07	77:06:17	50:00:50

These data are qualitatively in good agreement with the CEMS breakdown curves but direct comparisons of crossover points is difficult e.g. when $\theta = 0.59^\circ$, the m/z 69 and 41 fragment ions are of equal intensity for the 2-olefin and therefore from reference 28 $E_{0.59} = 5$ eV. Turning to the 1-olefin, the m/z 56 and 41 fragment ions will be of equal abundance when θ is slightly $> 0.59^\circ$ i.e. at a larger value of E but the CEMS data has them of equal abundance at $E = 4.2$ eV.

Overall the ARMS data on the C_5H_{10} isomers can be used to produce

CHAPTER 6

'breakdown curves' whose major features qualitatively agree with data from other techniques, but for quantitative studies they are of limited value.

6.5 n-BUTYLBENZENE

As in the previous section, the rationale behind obtaining these results was to compare ARMS data with that obtained by an analogous technique i.e. photoexcitation. Beynon et al. (29), found that the kinetic energy released upon photoinduced fragmentation of a number of molecular ions was dependent upon the temperature of the ion source in which they were formed and that a change in ion source temperature of 100°C altered the average internal energy of n-butylbenzene molecular ions by = 0.27eV. In Figure 6.27 are data for the following reaction of n-butylbenzene molecular ions;



produced either in a 'cold' source, i.e. source heater off but still indirectly heated by the filament, or in a source at approximately 190°C. If this equates to a difference in source temperature of =100°C, the molecular ions before collisional activation will from reference 29, differ in internal energy by approximately 0.27eV and this will also be true after activation. Referring again to Figure 6.3 therefore:

$$E_{F, \text{high}} = E_{F, \text{low}} + 0.27\text{eV} \quad (11)$$

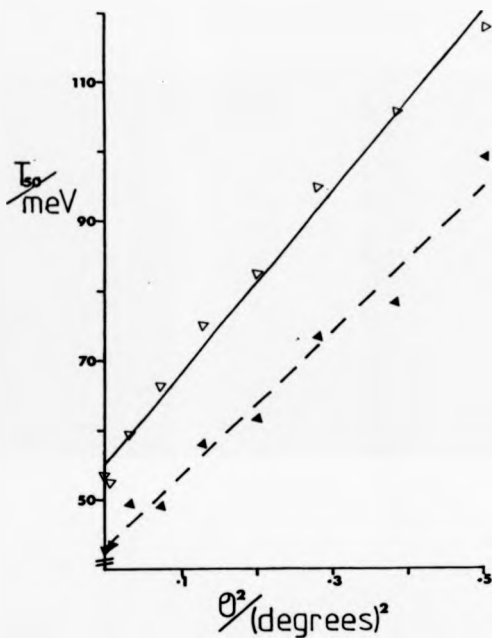


Figure 6.27 T_{50} as a function of θ for $(C_{10}H_{12})^+$ = $(C_{10}H_{11})^+$ +

$C_2H_5^+$. For parent ions produced either in a 'hot' source (top trace) or a 'cold' source.

CHAPTER 6

There are now two ways of looking at the relationship between ϵ'' and T'' . Firstly, when looking at a difference between two T values, one can write:

$$\epsilon''_{T_{\text{high}}} - \epsilon''_{T_{\text{low}}} = 0.27 = \Delta \epsilon'' \quad (12)$$

and if:

$$T''_{T_{\text{high}}} - T''_{T_{\text{low}}} = \Delta T'' \quad (13)$$

then the relationship of Haney and Franklin (7) referred to earlier predicts that:

$$\frac{\epsilon''}{T''} = 0.44 \times 10^{-5} \quad (14)$$

and therefore:

$$\Delta T'' = \frac{\Delta \epsilon''}{0.44 \times 10^{-5}} = \frac{\Delta \epsilon''}{28.6} = \frac{0.27}{28.6} = 9.4 \text{ meV} \quad (15)$$

The second approach to the problem is to estimate $\Delta T''$ from the measured difference in the kinetic energy release values. For a Gaussian peak T is approximately $2.16 \times T_{\text{so}}$ (30) and for a simple cleavage reaction ϵ''_0 is ≈ 0 , therefore $T = T''$ and T_{so} is approximately $T'' + 2.16$. It follows that:

$$\Delta T_{\text{so}} = \Delta T'' + 2.16 \quad (16)$$

CHAPTER 6

At $\theta=0^\circ$, ΔT_{20} is 12meV, rising to 25meV when $\theta=0.7^\circ$ and therefore from equation 16, ΔT^* is between 26 and 54meV i.e. between 2.8 and 5.7 times greater than predicted from equation 14. It is quite common for T^* values calculated using equation 14 not to agree with the experimentally determined values. In such cases it is interesting to determine the value of α needed to make the two sets of data agree, particularly since α has been shown to vary markedly for apparently similar reactions (20). For example, according to reference 20, α is 0.25 for NO_2 loss from 3-nitrobenzaldehyde and 0.87 for NO_2 loss from 2-fluoronitrobenzene. Rearranging equation 15 gives the following:

$$\alpha = \frac{\Delta E^*}{\Delta T^*} = 66 \quad (17)$$

$$\alpha = 0.16 \text{ at } \theta=0^\circ \text{ and } 0.08 \text{ at } \theta=0.7^\circ$$

These values for α are quite low, but as equation 7 is empirical this is not unexpected.

6.6 CONCLUSIONS

The fact that the 29/31 fragment ion ratio (R) of methanol is apparently proportional to $(E_w)^{2/3}$, should be investigated further for a wider range of E_w values than used in this study. It was interesting to find that the variation in R with θ could be correlated with the change in the kinetic energy release (T) for m/z 32 = 31 as a function of θ . The changing shapes of the fragment ion peaks and the increasing R and T values found as θ

CHAPTER 6

increased all support the idea that the internal energy deposited during CA (E) increases with θ . The pressure plots are also in agreement with this view of ARMS and more importantly demonstrate that ARMS cannot satisfactorily be explained by any theory which assumes that θ_0 is zero.

The qualitative nature of ARMS data is demonstrated by the results obtained on the isomeric xylenes and the $C_{10}H_{12}$ isomers, although the quantitative usefulness of the data may have been improved had the metastable ions been removed from the spectra. These data show that ARMS complements, but cannot replace, CEMS and photoexcitation of ions as tools for ion structure determination.

Finally, the n-butylbenzene results show that energy differences between molecular ions before CA also exist afterwards and can be measured.

Overall ARMS is a useful addition to the methods available for isomer differentiation and the study of the energetics of collisional activation.

CHAPTER 6

6.7 REFERENCES

- (1) J. A. Laramée, P. H. Hemberger, R. G. Cooks, *Int. J. Mass Spectrom. Ion Phys.*, **33**, 231 (1980)
- (2) A. R. Hubik, P. H. Hemberger, J. A. Laramée, R. G. Cooks, *J. Am. Chem. Soc.*, **102**, 3997 (1980)
- (3) P. H. Hemberger, J. A. Laramée, A. R. Hubik, R. G. Cooks, *J. Phys. Chem.*, **85**, 2335 (1981)
- (4) R. K. Boyd, E. E. Kingston, A. G. Brenton, J. H. Beynon, *Proc. R. Soc. Lond.*, **A392**, 59 (1984)
- (5) S. Varma, J. D. Ciupak, R. G. Cooks, A. E. Schoen, P. Dobberstein, *Int. J. Mass Spectrom. Ion Phys.*, **52**, 311 (1983)
- (6) J. H. Beynon, R. G. Cooks, R. M. Caprioli, G. R. Lester, *Metastable Ions*, Elsevier, Amsterdam, 1973
- (7) M. A. Haney, J. L. Franklin, *J. Chem. Phys.*, **48**, 4093 (1968)
- (8) C. E. Klotz, *J. Chem. Phys.*, **58**, 5364 (1973)
- (9) P. J. Todd, R. J. Wermack, E. H. McBay, *Int. J. Mass Spectrom. Ion Phys.*, **50**, 299 (1983)
- (10) D. S. Waddell, R. K. Boyd, A. G. Brenton, J. H. Beynon, *Int. J. Mass Spectrom. Ion Processes*, **68**, 71 (1986)
- (11) A. Maquestiau, R. Flammang, G. L. Glish, J. A. Laramée, R. G. Cooks, *Org. Mass Spectrom.*, **15**, 131 (1980)
- (12) M. Rabrenovic, A. G. Brenton, T. Ast, *Org. Mass Spectrom.*, **18**, 587 (1983)
- (13) R. J. Day, D. A. Krause, W. L. Jorgensen, R. G. Cooks, *Int. J. Mass Spectrom. Ion Phys.*, **30**, 83 (1979)
- (14) J. Berkowitz, *J. Chem. Phys.*, **69**, 3044 (1978)
- (15) S. H. Lee, M. S. Kim, J. H. Beynon, *Int. J. Mass Spectrom. Ion*

CHAPTER 6

Processes, 75, 83 (1987)

And earlier papers by M.S. Kim with various coworkers.

- (16) C.E.D. Ouwkerk, S.A. McLuckey, P.G. Kistemaker, A.J.H. Boerboom, *Int. J. Mass Spectrom. Ion Processes*, 56, 11 (1984)
- (17) M.S. Kim, *Int. J. Mass Spectrom. Ion Phys.*, 50, 189 (1983)
- (18) M. Vestal, G. Lerner, *Fundamental Studies Relating to the Radiation Chemistry of Small Organic Molecules*, Office of Aerospace Research, USAF, ARL 67-0114, 1967
- (19) R.G. Cooks, Ed., "Collision Spectroscopy", Plenum: New York, p386 (1978)
- (20) I.W. Griffiths, E.S. Mukhtar, F.M. Harris, J.H. Baynon, *Int. J. Mass Spectrom. Ion Phys.*, 38, 333 (1981)
- (21) E.S. Mukhtar, I.W. Griffiths, F.M. Harris, J.H. Baynon, *Org. Mass Spectrom.*, 16, 51 (1981)
- (22) W.A. Chupka, M. Kaminsky, *J. Chem. Phys.*, 35, 1991 (1961)
- (23) H.M. Rosenstock, M.B. Wallenstein, A.L. Wahrhaftig, H. Eyring, *Proc. Nat. Acad. Sci.*, 38, 667 (1952)
- (24) M.L. Vestal, A.L. Wahrhaftig, W.H. Johnston, *J. Chem. Phys.*, 37, 1276 (1962)
- (25) W.A. Chupka, J. Berkowitz, *J. Chem. Phys.*, 47, 2921 (1967)
- (26) E. Pettersson, E. Lindholm, *Ark. Fys.*, 24, 49 (1963)
- (27) B. Brehm, E.v. Puttkamer, *Z. Naturforsch.*, 22a, 8 (1967)
- (28) Jan. A. Herman, Yip-Hoi Li, A.G. Harrison, *Org. Mass Spectrom.*, 17, 143 (1982)
- (29) I.W. Griffiths, E.S. Mukhtar, F.M. Harris, J.H. Baynon, *Int. J. Mass Spectrom. Ion Phys.*, 43, 2639 (1982)

CHAPTER 6

- (30) J.L.Holmes, A.D.Osborne, *Int. J. Mass Spectrom. Ion Phys.*,
23, 189 (1977)

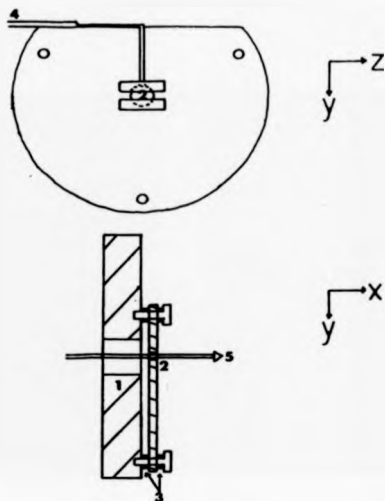
CHAPTER 7

7.1 INTRODUCTION

The method of mounting the collision chamber onto the swinging source was modified to allow a voltage to be applied to the collision chamber. This made it possible to separate collision induced fragment ions formed inside the chamber from the mixture of collision induced and unimolecular fragment ions formed outside the chamber.

7.2 THE MODIFICATIONS

Originally the collision chamber was screwed directly onto the stainless steel block on which the swinging source pivots are mounted. To insulate the collision chamber from the block, 1mm quartz spacers were placed between it and the block and between the screws and the collision chamber, see Figure 7.1. Also, because it is vital that the centre of the collision region is on the y-axis between the two pivots, 1mm was machined off the face of the block. The collision chamber voltage is supplied by a dedicated power supply Wallis Electronics Ltd, Model 5PMR2 via the feedthrough which had previously been used to ground the aperture plate externally. As a result, the aperture plate is now grounded inside the source housing. Although the power supply can provide any voltage between +5kV and -5kV, the collision chamber can only be floated at voltages between +2kV and -2kV because arcing occurs at higher voltages.



KEY

- | | |
|-----------------------|--------------|
| 1) Mounting block | 4) Gas inlet |
| 2) Collision chamber | 5) Ion beam |
| 3) 1mm Quartz spacers | |

Figure 7.1 Schematic diagrams of the mounting of the swinging source collision chamber, modified so that a potential can be applied to it.

CHAPTER 7

7.3 INITIAL RESULTS

Initially experiments were undertaken to answer the following questions:

- (1) Does the voltage on the collision chamber alter the range of angles observed at a particular scattering angle?
- (2) Does the fact that the first earth plate after the collision chamber is fixed to the back face of the source housing and does not therefore move with the source affect the relationship between micrometer setting and source housing?

In an attempt to answer these questions, the scattering of Ar^+ by argon atoms was studied as a function of scattering angle (see also Chapter 5). Four different sets of data were obtained using the source and collision chamber voltages given in Table 7.1.

TABLE 7.1 Source and collision chamber voltages used when acquiring the data in Figure 7.2

Data set	Source Voltage V	Collision Chamber Voltage V,
	/ Volts	/ Volts
1	+7000	-500
2	+7000	0
3	+7500	0
4	+7000	-500

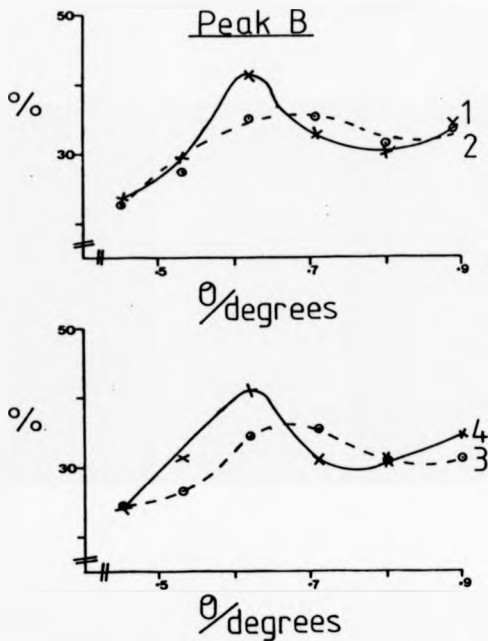


Figure 7.2a The intensity of the 'B' peak as a percentage of (A+B+C+D) for Ar^+ scattered by Argon atoms as a function of θ . The source and collision chamber voltages are given in Table 7.1.

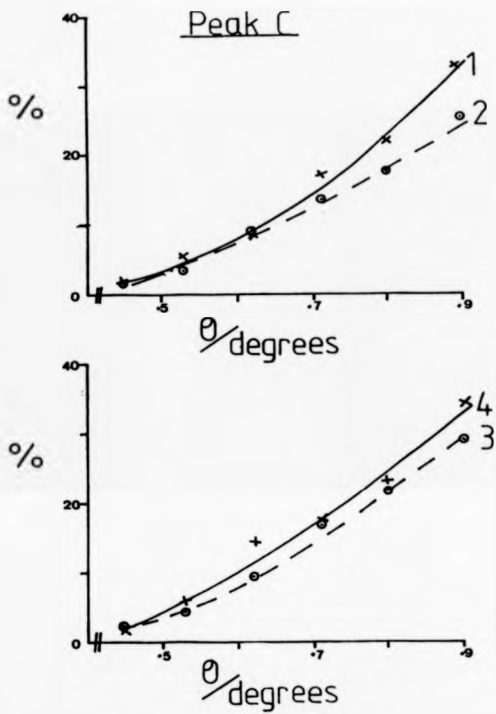


Figure 7.2b As Figure 7.2a, but for the 'C' peak.

CHAPTER 7

It was found that the collision chamber voltage affected θ_{scat} and as a result data were obtained, either;

a) When θ_{scat} had been determined with the collision cell at ground potential, then the desired voltage was applied to the cell and the collector signal optimised using the y- and z-deflectors on the swinging source e.g. curves 2,3 and 4 of Figure 7.2.

or

b) When θ_{scat} was determined with the collision cell at the required voltage, then the lens and deflector voltages were set as described earlier (page 74) e.g. curve 1 of Figure 7.2.

From these data in Figure 7.2 it is apparent that applying a potential to the collision chamber does alter the range of scattering angles observed at a particular θ because the differences between curves 1 and 2 cannot be explained by the different kinetic energies of the primary ion beam. If this were the case curve 2 would not be similar to curve 3. The results for peak C suggest that applying a negative potential to the cell enhances the detection of ions scattered through large angles. Overall, these data indicate that the usefulness of the source for studying scattering is not seriously affected by applying a voltage to the collision chamber.

The performance of the modified source was then investigated by measuring the kinetic energy released during the fragmentation of n-butylbenzene molecular ions to give the fragment ion $[\text{C}_6\text{H}_5\text{CH}_2]^+$ (1). When a voltage is applied to a collision chamber fragment ions formed inside it have different velocities from those formed

CHAPTER 7

outside it and therefore have different coordinates on the B/E plane. It follows therefore that for:

$$\begin{aligned} m_1 v_1 &= m_2 v_2 + m_3 v_3 \\ E_1, B_1 & \quad E_2, B_2 \end{aligned} \quad (1)$$

where;

E_1 = electric sector voltage to pass m_1 ions

B_1 = magnet current to pass m_1 ions

If the ion source voltage is V and the collision chamber is held at a potential V_1 , then when $V_1 = 0$,

$$E_2 = E_1 \times m_2/m_1 \quad \text{and} \quad B_2 = B_1 \times m_2/m_1 \quad (2)$$

but if $V_1 \neq 0$ then,

$$E_2 = E_1 \times [m_2/m_1 \times (1 - (V_1/V)) + V_1/V] \quad (3)$$

$$B_2 = B_1 \times m_2/m_1 \times [(1 - (V_1/V)) + m_1 V_1 / m_2 V]^{1/2} \quad (4)$$

The derivation of equations 3 and 4 is explained in Appendix II together with the formula used to calculate T_{EO} values.

When the relative abundances of fragment ions were to be measured, the daughter ions were allowed to reach the detector by manually setting the appropriate value of E on the decade box and doing a small magnet scan about the required value of B . The resulting peak profiles were acquired into a signal averager to

CHAPTER 7

improve the S/N ratio. For peak width measurements E and B were set in the same way, but peak profiles were obtained by a small scan of V . In this way the source tuning conditions and the kinetic energy of the precursor ion before fragmentation were kept constant for all fragment ions. Data from Holmes et al. (2) have shown that significant differences in metastable peak intensities occur if V is not a constant for all the fragment ions.

In Figure 7.3, the results obtained in this study are compared to earlier results (see page 137) obtained with the collision chamber at ground potential. Singh et al. (3), have also used a floating collision chamber when determining kinetic energy release values as a function of θ . They found that T_{max} values were reduced by 40% at all angles when a voltage was applied to the collision chamber, but the polarity of the voltage and the formula used when calculating T_{max} are not reported. In contrast to their findings, the results in Figure 7.3 show that T_{so} was increased when the collision chamber was at -500V (7kV primary ion beam). This is not unexpected since by floating the collision chamber the metastable contribution to the fragment ion peak is removed and as T_{so} for the unimolecular fragmentation is usually less than for the collision induced fragmentation, its removal will increase the measured value of T . It is also to be expected that the difference between $T_{\text{so}}(V_i=0)$ and $T_{\text{so}}(V_i \neq 0)$ will decrease as θ increases and this is what was found. Even more importantly, floating the collision chamber does not destroy the previously observed linear relationship between T_{so} and θ^2 .

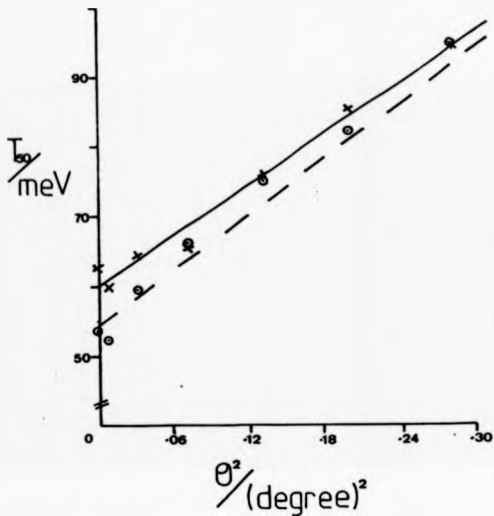


Figure 7.3 T_{50} for propyl loss from n-butylbenzene molecular ions as a function of θ . Data obtained with the collision chamber either at ground potential 0 or at a potential of -500V.

CHAPTER 7

7.4 CONCLUSIONS

Modifying the swinging source so that fragment ions arising from unimolecular fragmentation reactions can be excluded from angle resolved mass spectra has been easy to implement and has not adversely affected the quality of ARMS data which can be obtained within the source.

7.5 REFERENCES

- 1) S.Singh, M.S.Thecker, F.M.Harris, J.H.Beynon, *Org. Mass Spectrom.*, 20, 156 (1985)
- 2) J.L.Holmes, J.K.Terlouw, *Org. Mass Spectrom.*, 15, 383 (1980)
- 3) S.Singh, F.M.Harris, R.K.Boyd, J.H.Beynon, *Int. J. Mass Spectrom. Ion Processes*, 66, 151 (1985)

CHAPTER 8

8.1 INTRODUCTION

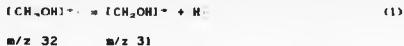
ARMS data which exclude metastable ions are compared with published data which do not. The results of the comparison necessitate a reinterpretation of the published data.

8.2 I₁₀₀/I₁₀₀₀ RATIOS

The rate at which the observed abundance of a fragment ion varies with the collision gas pressure depends upon a number of factors, which include:

- 1) The collision cross-section for the fragmentation.
- 2) The design of the collision chamber and ion optics of the mass spectrometer.
- 3) The collision gas.

In Figure 8.1, the log of the intensity of the fragment ion signal for the process:



is plotted as a function of the collision gas pressure (Argon). Data were acquired when θ was 0° (upper two traces) and 0.53° (lower two traces) for fragment ions formed inside (I_{in}) and outside (I_{out}) the collision chamber. The figures in brackets show how the ratio I_{in}/I_{out} varied with the collision gas pressure.

Assuming that all the fragment ions produced inside the cell are the result of collision induced dissociations (the validity of

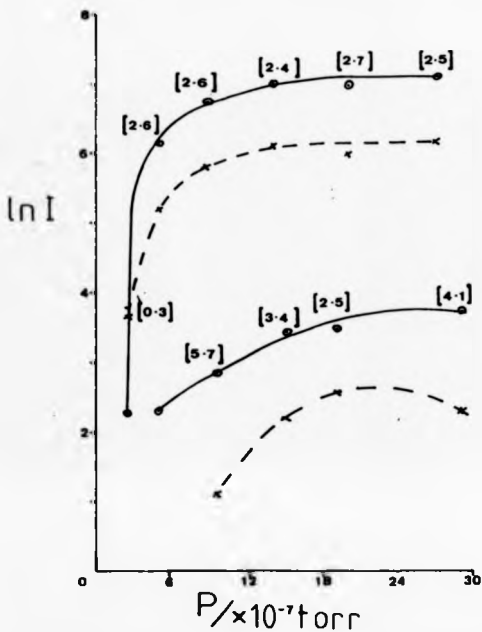


Figure 8.1 The abundance of m/z 31 as a function of Ar collision gas pressure when $\theta=0^\circ$ (upper two traces) and $\theta=0.53^\circ$ (lower two traces) for fragment ions produced inside and outside π of the cell. ($I_{\text{ion}}/I_{\text{max}}$)

CHAPTER 8

this assumption increases as the collision gas pressure increases) and that all the fragment ions produced outside the cell are the result of unimolecular fragmentation (valid at low collision gas pressures), then, at zero scattering angle, I_{1n} should be more cell pressure dependent than I_{0n} and the data in Figure 8.1 lends credibility to this assumption. At pressures $> 13 \times 10^{-7}$ torr the fragment ion intensity and I_{1n}/I_{0n} (CID/ m^+) ratio is effectively constant (the results discussed in Chapters 4 and 6 were obtained at this pressure). The data obtained with $\theta = 0.53$ degrees differ from these data in that:

- 1) The fragment ion abundances are more strongly dependent upon collision gas pressure (I_{0n} is indistinguishable from the background at pressures below 9.5×10^{-7} torr).
- 2) I_{1n} is always altered when the collision gas pressure changes.

When the experiments were repeated using Helium as the collision gas the data plotted in Figure 8.2 were obtained. The major difference between the two sets of data is that less scattering occurs when Helium is the collision gas (1). When comparing Figures 8.1 and 8.2 the pressures should be adjusted to allow for the different response of an ion gauge to Helium and Argon. The data seems to suggest that the collision cell is not very efficient, but given that the cell is only 0.4mm long and that there are long field free regions on either side of it, a mean CID/ m^+ ratio of ≈ 2.6 is satisfactory. These results demonstrate the advantages of using a floating collision chamber when studying the pressure dependence of a collision induced dissociation (2).

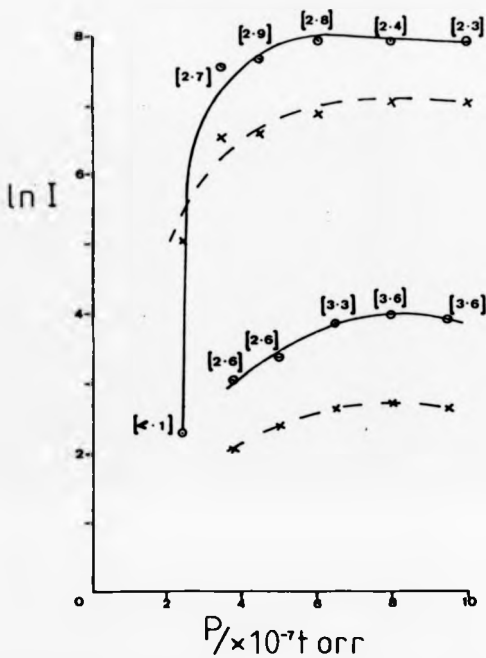
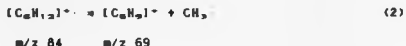


Figure 8.2 The abundance of $z=29$ as a function of He collision gas pressure when: $\theta=0^\circ$ (upper two traces) and $\theta=0.53^\circ$ (lower two traces: for fragment ions produced inside and outside of the cell. (I/I_{max}))

Using a short collision cell gives good energy (3) and angular resolution, as well as reducing the effect of unimolecular fragmentation on the total fragment ion abundance. The latter effect is particularly noticeable in the data in Figure 8.3, for the unimolecular reaction;



$I_{1,n}$ is $\approx I_{0,n}$ ($\theta=0^\circ$) in the absence of any collision gas but as collision gas is introduced the unimolecular part of $I_{0,n}$ is attenuated exponentially and the small unimolecular contribution to $I_{1,n}$ is overshadowed by the increasing number of collision induced dissociations. Considering the results obtained at $\theta=0.3^\circ$, we find that $I_{1,n}$ is still marginally $< I_{0,n}$. This is because when the swinging source is not at its zero angle position, fragment ions formed in the first field free region, i.e. between the ion source and the collision chamber, are prevented from reaching the detector by the slits of the mass spectrometer. These fragment ions will only be detected if they undergo non-dissociative scattering in the collision chamber.

The methanol and cyclohexane systems therefore represent two extremes of behaviour found in ARMS studies. If the $I_{1,n}/I_{0,n}$ ratio maximises at low collision gas pressures and is larger for scattered ions, then the fragment ions are mainly the result of collision induced dissociations. Alternatively, if the $I_{1,n}/I_{0,n}$ ratio is very small, increases exponentially as collision gas is

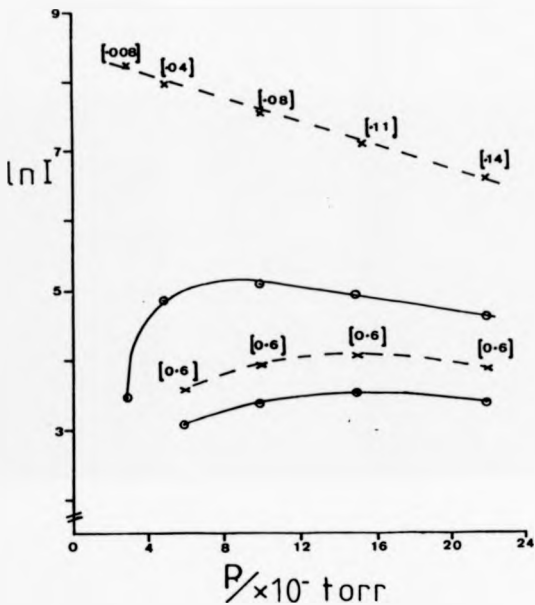


Figure 8.3 The abundance of m/z 69 as a function of Ar collision gas pressure when $\theta=0^\circ$ (upper two traces) and $\theta=0.27^\circ$ (lower two traces) for fragment ions produced inside θ and outside θ of the cell. $[I_{\theta=0}/I_{\theta=0.27}]$

CHAPTER 8

introduced and is smaller for scattered ions, then fragment ions are mainly the result of unimolecular dissociations. In both cases the measured total fragment ion abundances, i.e. $I_{100} + I_{101} + I_{102} + \dots$, will change with θ but this will not necessarily indicate that the precursor ion fragmentation rate depends upon θ .

8.3 FRAGMENT ION RATIOS

8.3.1 n-BUTYLBENZENE

The use of the 91/92 fragment ion ratio to estimate the internal energy of n-butylbenzene molecular ions stems from the photodissociation studies of Beynon and co-workers (4+6). Although the quantitative results of these studies have recently been questioned by Welch et al. (7) and Dunbar et al. (8), the qualitative conclusion that the 91/92 ratio increases with the internal energy of the parent ions remains undisputed. The results obtained by various mass spectrometric techniques on n-butylbenzene have been assessed in a paper by Boyd et al. (9) which also attempts to rationalise the quantitative differences between the data sets.

Data on the variation in the 91/92 ratios of substituted aromatic compounds as a function of scattering angle have been reported by a number of workers (10+12) but these data were not adjusted to take account of metastable contributions to the fragment ion abundances. With the collision chamber at a potential of -500V (+6000V accelerating voltage on the ion source), data comparable to those reported by other groups were obtained when total

fragment ion abundances i.e. $I_{m^+} + I_{CID}$ and $m^+ + CID$ were used in the calculation of the 91/92 ratios, as shown in Figure 8.4. Very different results are obtained however, if only I_{m^+} values are used in the calculation of the 91/92 ratios, (Figure 8.5). The possible effect of metastable ions on ARMS data for *n*-butylbenzene has been discussed by Harrison et al. In reference 13 they report 91/92 ratios of 1.2 ($m^+ + CID$) and 2.7 (CID only) obtained on a ZAB-2F mass spectrometer using Helium collision gas and a source potential of 8000V. These ratios are for a mixture of scattered and unscattered ions as the spectrometer had not been modified to collect ARMS data. If these values are compared to the zero angle data in Figure 8.5, the CID only ratios are identical, within experimental error, but the ($m^+ + CID$) ratio is considerably larger. This is because of the large number of unimolecular decompositions occurring before and after the swinging source collision chamber. N.B. Cyclohexane data in Figure 8.3. Although Harrison et al. realise that the ratios reported in references 11 and 12 are probably erroneous, because the ARMS data is in general agreement with their charge exchange results, they conclude that the main reason for the increase in the 91/92 ratio with scattering angle is increased energy deposition. They had reached a similar conclusion in an earlier comparison of charge exchange, field ionization kinetics and ARMS data on 3-penten-2-ol (14). In a later paper (15) other examples of the influence of metastable ions on ARMS data are given and these results are discussed later.

In Figure 8.6, the CID/ m^+ ratios of the two fragment ions are

on of 8.

swinging

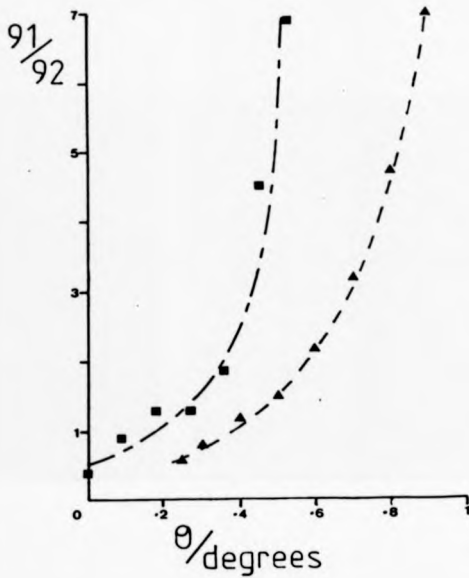


Figure 8.4 The 91/92 ratio for n-butybenzene as a function of θ . Total fragment ion abundance data from the swinging source ■ compared with data from reference [2] ▲.

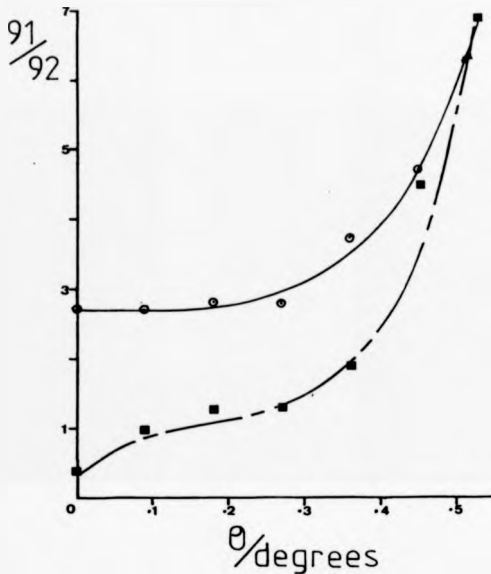


Figure 8.5 The 91/92 ratio for n-butylbenzene as a function of θ . Ratios calculated from total fragment ion abundance data from the swinging source ■ compared with fragment ion abundance ratios from inside the collision chamber ○.

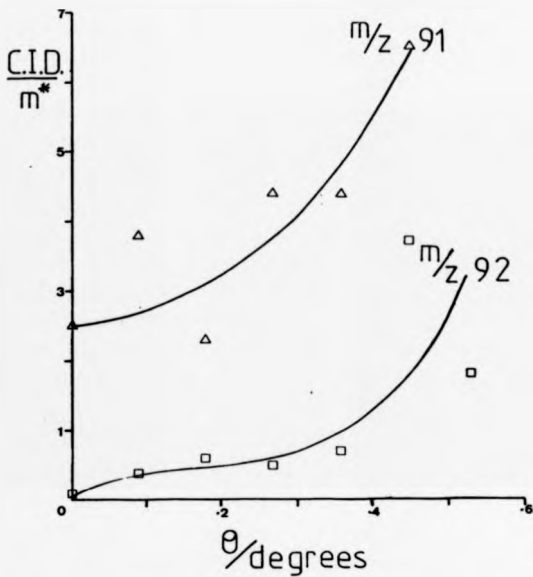


Figure 8.6 The C.I.D./ m^* ratios of two n-butylbenzene fragment ions as a function of θ .

plotted as a function of θ . From these data it can be seen that if the 91/92 ratio is computed from the sum of the metastable and collision induced fragment ion abundances, it will increase with θ , NOT because of any change in the internal energy of the parent ion, but because the metastable contribution to the m/z 92 fragment decreases as θ increases.

As shown in Figure 8.7, similar results to those in Figure 8.5 have been obtained by Beynon et al. (16) using a floating collision chamber on a modified ZAB-2F mass spectrometer. The differences between the two data sets are probably a consequence of the different angular resolutions of the spectrometers. Using an extended version of a calculation originally reported by Todd (17), Beynon et al. compare their results with fragment ion distributions calculated from the kinetic energy released during fragmentation. The method assumes that scattering is negligible and that a fragment ion has an angular distribution which reflects the magnitude and orientation of the kinetic energy released during its formation. For two fragment ions of approximately equal mass therefore, the most abundant ion at high angles will be the one whose formation involves the greatest release of kinetic energy. If $T_{\text{c.m.}}$ values of 70meV and 150meV for $134 \rightarrow 92$ and $134 \rightarrow 91$ respectively are used, the calculated variation in the 91/92 ratio is similar to that obtained experimentally when the collision chamber is at ground potential. The good agreement between the theoretical and practical results may be fortuitous however, as the experimental variation may simply be a product of the discrimination effect explained above. In reference 16, the

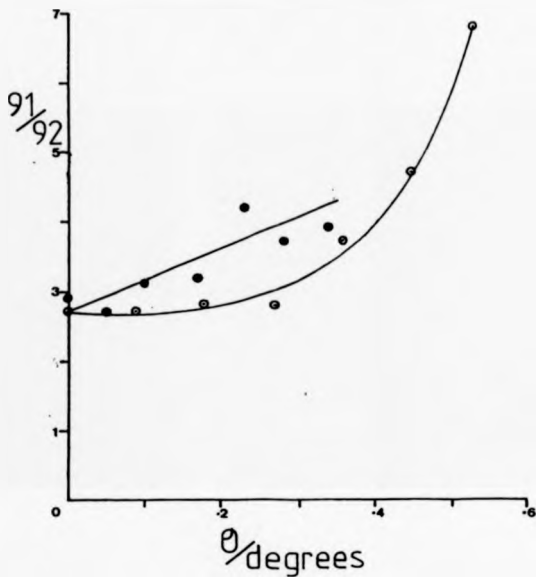


Figure 8.7 The 91/92 ratio for *n*-butylbenzene as a function of θ . Ratios calculated from CID only fragment ion abundance data from the swinging source θ compared with ratios from reference 16.

kinetic energy releases for $134 \rightarrow 92$ and $134 \rightarrow 91$ inside the cell are reported as being 120meV and 140meV respectively. If these values had been used in the calculation of the ratio, then similar data to that obtained experimentally with the floated cell would have been produced, a result which does support Todd's view of ARMS data.

8.3.2 BENZYL METHYL ETHER

In reference 12, Cooks et al. report ARMS data on benzyl methyl ether which seem to be difficult to rationalise if one considers kinetic energy releases alone. As mentioned earlier (Chapter 4), the 91/92 fragment ion ratio increases with θ , but for this ion the kinetic energy release for $M^+ \rightarrow 92$ is \approx for $M^+ \rightarrow 91$. When the 91/92 fragment ion ratio for benzyl methyl ether was measured using the swinging source, the data plotted in Figure 8.8 were obtained. Once again, if total fragment ion abundances are used the results are comparable to those obtained by the z-deflection method, but when $I_{m,n}$ values are used the 91/92 ratio is constant over the range of angles $\theta=0$ to 0.5° . ARMS data for benzyl methyl ether which exclude metastables have not been published by other groups, but Harrison et al. (15) reported 91/92 ratios of 0.4 ($m^+ + CID$) and 0.8 (CID only), i.e. considerably lower than those reported here.

The 91/92 fragment ion ratios measured using the swinging source are compared to charge exchange data from Harrison and various co-workers (15,18,19) in the table below.

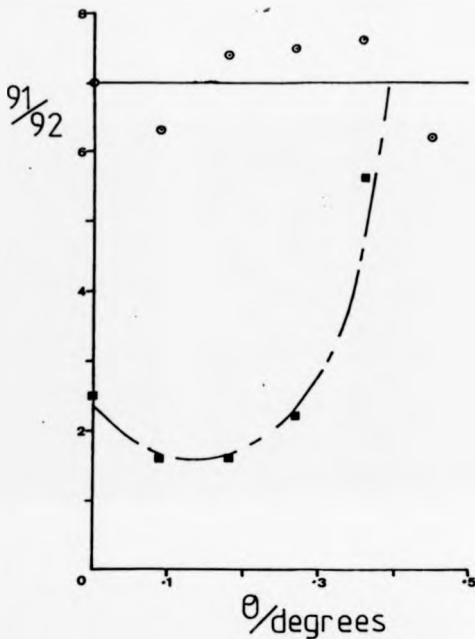


Figure 5.8 The 91/92 ratio for benzyl methyl ether as a function of θ . Ratios calculated from total fragment ion abundance data from the swinging source \circ compared with C10 only ion abundance ratios \blacksquare .

CHAPTER 8

TABLE 8.1 E_{ion} values obtained by comparing 91/92 ratios in ARMS data with CEMS data.

COMPOUND	91/92 RATIO		E_{ion} (eV)	
	(a)	(b)	(a)	(b)
n-butylbenzene	2.7	0.4	4.6	2.8
benzyl methyl ether	7.3	2.5	4.2	2.5
2-phenylethanol	0.6	0.2	3.4	2.5

(a) CID only and (b) $m^+ + CID$ Both (a) and (b) for $\theta=0^\circ$

The comparison illustrates one problem which can occur when data from collisional activation experiments are compared with results obtained by other techniques. Unless the metastable contribution to the fragment ion abundances is removed, the observed fragment ion ratios will depend upon the m^+/CID ratio of the data, e.g. when estimating E_{ion} for n-butylbenzene molecular ions, values between 4.6 and 2.8eV may be inferred from the above data, and the m^+/CID ratio will depend upon the ion optics of the mass spectrometer.

8.4 GENERAL CONCLUSIONS

The data on n-butylbenzene and benzyl methyl ether highlight an important problem in the interpretation of ARMS data

CHAPTER 8

which include metastable ions. If one considers the following fragmentation reactions of a molecular ion M^{+} :



The ratio of the two fragment ion abundances $([A]/[B])$, will depend upon the internal energy of M^{+} (E), because the rates of reactions 3 and 4 depend upon E . If the rates of the two reactions were plotted as functions of E , then curves like those in Figure 8.9 would be obtained. The general shape of these curves can be predicted using the Rice, Ramsperger, Kassel and Marcus theory (RRKM, reference 20) or the Quasi-Equilibrium theory (QET, reference 21). According to simple QET, the rate constant, k , of a unimolecular reaction can be calculated from the following expression :

$$k(E) = \nu (E - E_0)/E^{s-1} \quad (5)$$

where :

E is the ion's energy

E_0 is the activation energy for the reaction

ν is a frequency factor

s is the effective number of oscillators

For a simple cleavage reaction the activation energy is quite large, therefore $(E - E_0)$ is small and k increases rapidly with E .

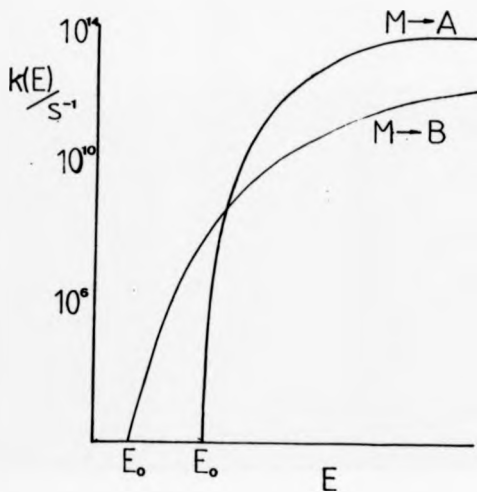


Figure 8.9 Theoretical rate constants k as a function of parent ion internal energy E for two hypothetical reactions of parent ion M^+ giving fragment ions A^+ and B^+ .

CHAPTER 8

Rearrangement reactions generally have lower activation energies (energy is released when new bonds are formed in the transition state) but because a specific molecular orientation is required for the reaction, ν is reduced which limits the ultimate rate. Also, the freezing out of rotational degrees of freedom during the formation of the transition state reduces the rate of increase of k with E . As can be seen from Figure 8.9 therefore, at low E the ratio $[A]/[B] < 1$, but as E increases this ratio also increases until it is > 1 . It follows therefore that if E increases with θ then so will $[A]/[B]$. Unfortunately, rearrangement reactions generally give rise to intense metastable ions and the efficiency with which these ions can be collected decreases rapidly as θ increases. One can therefore predict that if $[A]/[B]$ is calculated from total fragment ion abundances, it will increase with θ irrespective of any change in the internal energy of the parent ion. Although this effect is not dominant in all ARMS studies so far reported, it is important that it should be allowed for. From references 12,13,14,17 and the data reported in this thesis, systems studied by ARMS which may be prone to this problem are:

- 1) n-butylbenzene
- 2) benzyl methyl ether
- 3) cyclohexane
- 4) 3-pentan-2-ol

8.5 REFERENCES

- (1) P.H. Hemberger, J.A. Laramée, A.R. Mubik, R.G. Cooks, *J. Am. Chem. Soc.*, **85**, 2335 (1981)
- (2) S. Howells, A.G. Brenton, J.H. Beynon, *Int. J. Mass Spectrom. Ion Phys.*, **32**, 379 (1980)
- (3) J.H. Beynon, R.G. Cooks, T. Kao, *Int. J. Mass Spectrom. Ion Phys.*, **13**, 437 (1974)
- (4) W. Griffiths, E.S. Mukhtar, R.E. March, F.M. Harris, J.H. Beynon, *Int. J. Mass Spectrom. Ion Phys.*, **39**, 125 (1981)
- (5) E.S. Mukhtar, I.W. Griffiths, F.M. Harris, J.H. Beynon, *Int. J. Mass Spectrom. Ion Phys.*, **37**, 159 (1981)
- (6) I.W. Griffiths, E.S. Mukhtar, F.M. Harris, J.H. Beynon, *Int. J. Mass Spectrom. Ion Phys.*, **43**, 283 (1982)
- (7) M.J. Welch, D.J. Pareles, E. White, *Org. Mass Spectrom.*, **20**, 425 (1985)
- (8) J.H. Chen, J.D. Hays, R.C. Dunbar, *J. Phys. Chem.*, **88**, 4759 (1984)
- (9) R.K. Boyd, F.M. Harris, J.H. Beynon, *Int. J. Mass Spectrom. Ion Processes*, **66**, 185 (1985)
- (10) E.E. Kingston, A.G. Brenton, R.K. Boyd, J.H. Beynon, *Int. J. Mass Spectrom. Ion Phys.*, **47**, 117 (1983)
- (11) S. Varma, J.D. Cupek, R.G. Cooks, A.E. Schoen, P. Dobberstein, *Int. J. Mass Spectrom. Ion Phys.*, **52**, 311 (1983)
- (12) S.A. McLuckey, S. Varma, R.G. Cooks, M.J. Ferncombe, R.S. Mason, K.R. Jennings, *Int. J. Mass Spectrom. Ion Phys.*, **48**, 423 (1983)

CHAPTER 8

- (13) S. Nascon, A.G. Harrison, *Int. J. Mass Spectrom. Ion Processes*, **63**, 325 (1985)
- (14) J. Zwinselman, A.G. Harrison, *Int. J. Mass Spectrom. Ion Processes*, **62**, 187 (1984)
- (15) J. Zwinselman, S. Nascon, A.G. Harrison, *Int. J. Mass Spectrom. Ion Processes*, **67**, 93 (1985)
- (16) S. Waddell, R.K. Boyd, A.G. Brenton, J.H. Beynon, *Int. J. Mass Spectrom. Ion Processes*, **68**, 71 (1986)
- (17) P.J. Todd, R.J. Wermack, E.J. McBay, *Int. J. Mass Spectrom. Ion Phys.*, **50**, 299 (1983)
- (18) A.G. Harrison, M.S. Lin, *Int. J. Mass Spectrom. Ion Phys.*, **51**, 353 (1983)
- (19) E. Wager, K. Levsan, J. Zwinselman, A.G. Harrison, *Int. J. Mass Spectrom. Ion Processes*, **65**, 231 (1985)
- (20) R.A. Marcus, *J. Chem. Phys.*, **20**, 399 (1952)
- (21) H.M. Rosenstock, M.B. Wallenstein, A.L. Wahrhaftig, H. Eyring, *Proc. Natl. Acad. Sci. USA*, **36**, 667 (1952)

APPENDIX I

A1.1 INTRODUCTION

As the main advantage of the swinging source over other ways of obtaining ARMS data is repeatability of angle selection irrespective of daughter and parent ion masses, the relationship between the micrometer setting x and θ is very important.

For any given value of x , ions scattered over a range of scattering angles will be collected i.e. $\theta \pm \Delta\theta$. The value of $\Delta\theta$ can be estimated from the slit widths and the distances between them using basic trigonometry.

A1.2 CALCULATION OF θ

Figure 1.1a is a schematic diagram of the main parts of the angle selection mechanism of the swinging source and is a section through the centre of the source cradle on the zx plane, assuming that $\theta=0^\circ$. Ions travel along OE to the centre of the collision chamber at point E. Not shown are the electrical focus and deflector plates contained within the source cradle ABCD. The two pivot assemblies which allow the source to move in a zx plane orthogonal to the plane of the paper. The central axis of the micrometer shaft IH is connected via the link arm GH to the side of the swinging source cradle at point G. A perpendicular from G to the ion optical axis of the source EO, meets the axis at F_0 and the angle GEO is denoted by α . Similarly, the perpendicular from H_0 to a line through G running parallel to EO meets it at P_0 . When the source is not at zero angle (Figure 1.1b) then H is moved towards I along IP. As HG is a constant length with pivots at G and H,

APPENDIX I

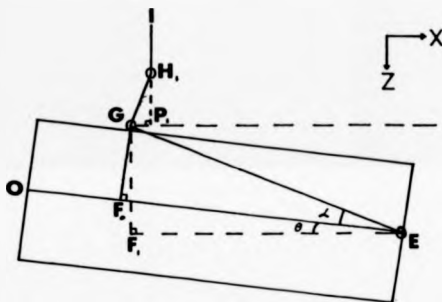
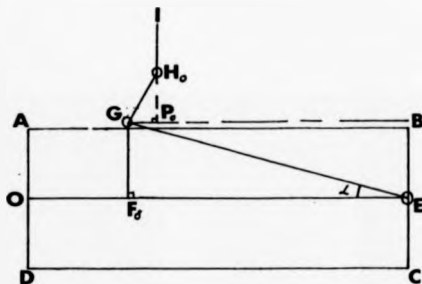


Figure 1.1a Schematic diagram of the source when $\theta=0^\circ$.

Figure 1.1b Schematic diagram of the source when $\theta \neq 0^\circ$.

APPENDIX I

the source cradle pivots about point E until the ion beam is at an angle θ with respect to its original position. Then F_1 corresponds to F_0 and $EF_1 < EF_0$, but GE is constant. Also, P_0 becomes P_1 , and GP_1 is $< GP_0$. To be exact,

$$GP_0 - GP_1 = EF_0 - EF_1 \quad (1)$$

and H_0 moves along HI to position H_1 so that HP_1 is $> HP_0$. The indicated micrometer movement x is therefore given by:

$$x = (GF_1 - GF_0) - (H_1P_1 - H_0P_0) \quad (2)$$

Using the trigonometric formulae given below the value of x has been calculated for angles between 0 and 1.5° in steps of 0.1° , Table I.1.

$$\tan \alpha = GF_0/EF_0 = 53/205 = 0.258 \quad (3)$$

$$\therefore \alpha = 14.5^\circ$$

$$\cos \alpha = EF_0/EG \quad (4)$$

$$\therefore EG = EF_0/\cos \alpha = 205/0.968$$

$$= 211.7 \text{ mm}$$

When $\theta = 1.0^\circ$,

$$\sin(\alpha+\theta) = GF_1/GE \quad (5)$$

APPENDIX I

$$\Sigma GF_1 = \sin(\alpha+\theta) \times GE$$

$$= 56.55 \text{ mm}$$

From the source plans, $GP_0 = 6 \text{ mm}$ and $EF_0 = 205 \text{ mm}$, so if ,

$$\cos(\alpha+\theta) = EF_1 / GE \quad (6)$$

$$\therefore EF_1 = GE \times \cos(\alpha+\theta)$$

$$= 204.05 \text{ mm}$$

From equation 1,

$$6 - GP_1 = 205 - 204.04$$

$$\therefore GP_1 = 5.05 \text{ mm}$$

Now using,

$$GM^2 = GP^2 + NP^2 \quad (7)$$

$$H_0P_0 = (729 - 36)^{\frac{1}{2}}$$

$$= 26.3 \text{ mm}$$

$$H_1P_1 = (729 - 25.5)^{\frac{1}{2}}$$

$$= 26.5 \text{ mm}$$

Finally from equation 2,

$$x = (56.55 - 53) - (26.5 - 26.3) \text{ mm}$$

$$= 3.35 \text{ mm}$$

APPENDIX I

TABLE I.1 The micrometer reading x needed to give θ values between 0 and 1.5° in increments of 0.1°.

θ°	x/mm	θ°	x/mm	θ°	x/mm	θ°	x/mm
0.1	0.313	0.5	1.660	0.9	3.008	1.3	4.358
0.2	0.649	0.6	1.997	1.0	3.346	1.4	4.696
0.3	0.986	0.7	2.334	1.1	3.683	1.5	5.034
0.4	1.323	0.8	2.671	1.2	4.041		

As expected there is a linear relationship between x and θ . When the above data are recorded graphically (Figure I.2) a straight line of slope $3.372 \text{ mm deg}^{-1}$ and intercept $-.0026 \text{ mm}$ is obtained with a correlation coefficient of 0.999.

A1.3 CALCULATION OF θ_0

The apertures which change the divergence of the ion beam in the xz plane are listed in Table I.2, together with their possible lengths along the z -axis.

APPENDIX I

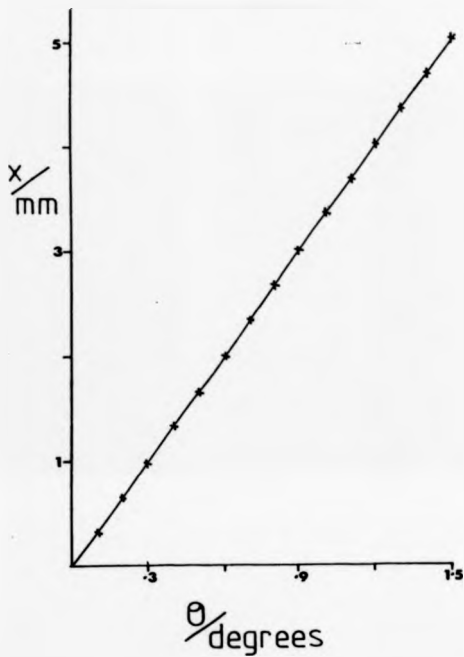


Figure I.2 The linear relationship between x (the micrometer setting) and θ .

APPENDIX I

TABLE I.2 The possible lengths of the apertures which alter the size of the ion beam in the xz plane.

APERTURE	LENGTH / mm
(1) First aperture plate	2.54, 0.5
(2) Adjustable z-restrictor	5.08, 2.54, 0.508
(3) Source z-slit	2.54, 1.27, 0.508
(4) Collector z-slit	5.08, 2.54, 0.508

As can be seen from Figure I.3, the divergence half-angle of an ion beam (α) passing through two slits can be calculated using the relationship,

$$\tan \alpha = \frac{WAB + WCD}{XY} \quad (8)$$

On the swinging source XY is 226mm when calculating α for the primary ion beam (Aperture 1 = 2) and 1960mm when calculating the α for the fragment ion beam (Aperture 3 = 4). It was by using equation 1 and the above dimensions that the data given in Tables 5.2 and 5.3 in Chapter 5 were calculated.

APPENDIX I

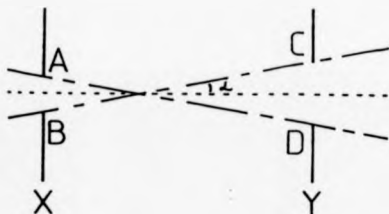


Figure I.3 Two slits of length AB and CD, separated by the distance XY will transmit an ion beam having a divergence half-angle of α .

APPENDIX II

A2.1 INTRODUCTION

Applying a potential to a collision chamber, so that the daughter ions produced inside it can be distinguished from those formed outside it, is a well known technique (1,2). It has generally only been used however, with mass spectrometers which separate the daughter ions using an electric sector i.e. by a MIKES or IKE scan (2+4). When the collision chamber is in the first field free region of a conventional geometry mass spectrometer, i.e. EB configuration, then daughter ions are usually separated by one of a number of linked scans (5), but the relationships from which the scan laws are derived do not apply if the collision chamber is not at ground potential. Equations which define the position of daughter ions on the BE plane when the collision chamber is floated at a potential V_c are derived below.

The measurement of the kinetic energy released when the parent ion fragments is also affected by V_c and therefore equations which allow for this effect have also been derived.

A2.2 DAUGHTER ION COORDINATES ON THE BE PLANE

Consider a positive ion m , accelerated out of an ion source to a velocity v_0 by a potential V . The kinetic energy of m , is given by:

$$KE = eV = \frac{1}{2}mv_0^2 \quad (1)$$

If this ion then enters a collision chamber at a potential V_c , it

APPENDIX II

will be accelerated (V_1 is negative) or decelerated (V_1 is positive) to a velocity v_1 and its kinetic energy will then be:

$$KE = e(V-V_1) = \frac{1}{2}m_1 v_1^2 \quad (2)$$

When this ion then fragments inside the collision chamber to a daughter ion m_2 and other products, the velocity of m_2 will be v_2 and its kinetic energy will be:

$$\frac{1}{2}m_2 v_1^2 = \frac{m_2}{m_1} e(V-V_1) \quad (3)$$

On leaving the collision chamber the ion's velocity will change to v_2 where:

$$\frac{1}{2}m_2 v_2^2 = \frac{m_2}{m_1} e(V-V_1) + eV_1 \quad (4)$$

For a given mass spectrometer an ion will be transmitted by the electric sector if:

$$\frac{mv^2}{E} = \text{constant} \quad (5)$$

In this case:

$$m_1 v_0^2/E_1 = m_2 v_2^2/E_2 \quad (6)$$

$$\therefore E_2 = E_1 = \frac{m_2 V_0^2}{m_1 v_0^2} \quad (7)$$

Substituting equations 1 and 4 into 7:

$$\therefore E_2 = \frac{v_1}{v_2} = \frac{m_2/m_1 e(V-V_1) + eV_1}{eV} \quad (8)$$

APPENDIX II

Define V_n as V_1/V and m_n as m_2/m_1 .

$$\therefore E_2 = E_1[m_n(1-V_n) + V_n] \quad (9)$$

Similarly, an ion will be transmitted by the magnetic sector if:

$$mv/B = \text{const.} \quad (10)$$

In this case:

$$m_1 v_0/B_1 = m_2 v_2/B_2 \quad (11)$$

From 1:

$$v_0 = [2eV/m_1]^{1/2} \quad (12)$$

From 4:

$$v_2 = [2e(V-V_n)/m_1 + 2eV_1/m_2]^{1/2} \quad (13)$$

$$\therefore B_2 = B_1 m_n [(1-V_n) + V_n/m_n]^{1/2} \quad (14)$$

When these formulae were derived, they were not available in the literature, but since then similar equations have recently been published by Boyd et al. (6) for use with a ZAB-4F (7) (BEEB sector configuration, with floatable collision chamber in the

APPENDIX II

third FFR).

A2.3 CALCULATION OF THE KINETIC ENERGY RELEASE

The kinetic energy released when an ion fragments in a F.F.R. can often be calculated from the width of the peak in the daughter ion spectrum, the formula depending upon the type of mass spectrometer scan used when recording the spectrum. Published formulae, however, assume that the collision chamber is at ground potential and therefore the following equations were derived. From reference 8:

$$v_1 = v_1 \pm \left| \frac{2m_2 I}{m_1 m_2} \right|^{1/2} \quad (15)$$

From equation 3:

$$v_1 = \left| \frac{2e(V-V_1)}{m_1} \right|^{1/2} \quad (16)$$

Substitute equation 16 into 15:

$$v_1 = \left| \frac{2e(V-V_1)}{m_1} \right|^{1/2} \pm \left| \frac{2m_2 I}{m_1 m_2} \right|^{1/2} \quad (17)$$

Then, from equation 13:

$$v_2 = \left| \frac{2e(V-V_1)}{m_1} \right|^{1/2} \pm \left| \frac{2m_2 I}{m_1 m_2} \right|^{1/2} + \left| \frac{2eV_1}{m_2} \right|^{1/2} \quad (18)$$

If the collision chamber is held at a negative potential then equation 18 becomes,

$$v_2 = \left| \frac{2e(V+V_1)}{m_1} \right|^{1/2} \pm \left| \frac{2m_2 I}{m_1 m_2} \right|^{1/2} - \left| \frac{2eV_1}{m_2} \right|^{1/2} \quad (19)$$

APPENDIX II

The maximum and minimum kinetic energies of m_1 ions are therefore given by:

$$KE_{MAX} = \frac{1}{2} m_2 \left| \left\{ \frac{2e(V+V_1)}{m_1} \right\}^2 + \left\{ \frac{2m_1 T}{m_1 m_2} \right\}^2 - \left\{ \frac{2eV_1}{m_2} \right\}^2 \right|^{1/2} \quad (20)$$

$$KE_{MIN} = \frac{1}{2} m_2 \left| \left\{ \frac{2e(V+V_1)}{m_1} \right\}^2 - \left\{ \frac{2m_1 T}{m_1 m_2} \right\}^2 - \left\{ \frac{2eV_1}{m_2} \right\}^2 \right|^{1/2} \quad (21)$$

Fragment ions will be transmitted through the electric sector if they have the same kinetic energy as parent ions. Let V'' and V' be the accelerating voltages required to allow fragment ions of low and high kinetic energy to be transmitted to the detector. Then:

$$\begin{aligned} \frac{1}{2} m_2 \left| \left\{ \frac{2e(V''+V_1)}{a} \right\}^2 + \left\{ \frac{2m_1 T}{b} \right\}^2 - \left\{ \frac{2eV_1}{c} \right\}^2 \right|^{1/2} \\ = \frac{1}{2} m_2 \left| \left\{ \frac{2e(V'+V_1)}{d} \right\}^2 - \left\{ \frac{2m_1 T}{b} \right\}^2 - \left\{ \frac{2eV_1}{c} \right\}^2 \right|^{1/2} \quad (22) \end{aligned}$$

Substitute a, b, c and d for the terms in equation 22 and it can then be rewritten as:

$$(a + b - c)^2 = a^2 + b^2 + c^2 + 2(ab - bc - ac) \quad (23)$$

$$(d - b - c)^2 = d^2 + b^2 + c^2 + 2(-db - dc + bc) \quad (24)$$

$$\therefore a^2 + 2(ab - bc - ac) = d^2 + 2(-db - dc + bc) \quad (25)$$

$$a^2 - d^2 = -2ab + 2bc + 2ac - 2db - 2dc + 2bc \quad (26)$$

$$a^2 - d^2 = 2ac - 2dc - 2ab + 4bc - 2db \quad (27)$$

APPENDIX II

$$b(2c - a - d) = (a^2 - d^2)/2 + c(d - a) \quad (28)$$

$$\Delta b = \frac{0.5(a^2 - d^2) + c(d - a)}{(2c - a - d)} \quad (29)$$

Equation 29 must now be modified so that it only contains variables which can be measured directly in an accelerating voltage scan. If V_a is defined as the accelerating voltage required to transmit the centre of the fragment ion peak and ΔV as the measured peak width, then:

$$V^{+2} = V_a + \Delta V/2 \text{ \& } V^{-2} = V_a - \Delta V/2 \quad (30 \& 31)$$

Also let:

$$V_a = V_a + V_i \quad (32)$$

Then:

$$a = \left| \frac{2e(V_a + \Delta V/2)}{m_1} \right|^{1/2} \text{ and } d = \left| \frac{2e(V_a - \Delta V/2)}{m_1} \right|^{1/2}$$

Equation 30 can therefore be written as follows:

$$\left| \frac{2m_2 I}{m_1 m_2} \right|^{1/2} = \frac{0.5(a^2 - d^2) + c(d - a)}{(2c - a - d)} \quad (33)$$

$$\Delta T = \left| \frac{0.5(a^2 - d^2) + c(d - a)}{(2c - a - d)} \right|^{1/2} \times \frac{m_1 m_2}{2m_2} \quad (34)$$

When the collision chamber is at ground potential then V_i is zero and consequently c is zero. Equation 34 therefore becomes:

$$\Delta T = \left| \frac{0.5(a + d)(a - d)}{-1(a + d)} \right|^{1/2} \times \frac{m_1 m_2}{2m_2} \quad (35)$$

$$= \left| -0.5(a - d) \right|^{1/2} \times \frac{m_1 m_2}{2m_2} \quad (36)$$

APPENDIX II

If (a-d) can be evaluated, then obtaining a formula for T is easy. First let V_a replace V_w in the formulae for a and d:

$$a = \left| \frac{2e(V_a + \Delta V/2)}{m_1} \right|^m \quad \text{and} \quad d = \left| \frac{2e(V_a - \Delta V/2)}{m_1} \right|^m$$

Then a and d can be expanded using the following binomial expansion:

$$(a+x)^m = \left| 1 + \frac{1}{2} \frac{x}{a} + \frac{3}{4} \left(\frac{x}{a} \right)^2 \right| \times a^m \quad (37)$$

Using a similar expansion for $(a-x)^m$, gives the following:

$$(a-d) = (a+x)^m - (a-x)^m \quad (38)$$

$$(a-d) = \left| 1 + \frac{1}{2} \frac{x}{a} + \frac{3}{4} \left(\frac{x}{a} \right)^2 \right| \times a^m - \left\{ \left| 1 - \frac{1}{2} \frac{x}{a} + \frac{3}{4} \left(\frac{x}{a} \right)^2 \right| \times a^m \right\} \quad (39)$$

$$= \frac{x}{a} \times a^m \quad (40)$$

$$= \left| \frac{2e\Delta V}{2m_1} \times \frac{m_1}{2eV_a} \right| \times \left\{ \frac{2eV_a}{m_1} \right\}^m \quad (41)$$

Substituting equation 41 into equation 36 gives:

$$T = \frac{1}{4} \times \frac{\Delta V^2}{4V_a^2} \times \frac{2eV_a}{m_1} \times \frac{m_1 m_2}{2m_1} \quad (42)$$

$$T = \frac{m_2 e V_a}{16 m_1} \left\{ \frac{\Delta V}{V_a} \right\}^2 \quad (43)$$

This is the same formula that is given on page 62 of reference 8 and this proves the general applicability of equation 36. A basic program was written for a Sinclair Spectrum computer to calculate T from equation 34.

APPENDIX II

A2.4 REFERENCES

- 1) T. Wechs, C.C. Van de Sande, F.W. McLafferty, *Org. Mass Spectrom.*, **11**, 1308 (1976)
- 2) J.H. Beynon, R.G. Cooks, *Int. J. Mass Spectrom. Ion Phys.*, **19**, 107 (1976)
- 3) R.P. Morgan, J.H. Beynon, R.H. Bateman, B.N. Green, *Int. J. Mass Spectrom. Ion Phys.*, **28**, 171 (1978)
- 4) M.L. Gross, E.K. Chess, P.A. Lyon, F.W. Crow, S. Evans, H. Tudge, *Int. J. Mass Spectrom. Ion Phys.*, **42**, 243 (1982)
- 5) K.R. Jennings and R.S. Mason in *Tandem Mass Spectrometry*, John Wiley and Sons, 1983, Chapter 9.
- 6) R.K. Boyd, D.J. Harven, J.R. Mass, *Int. J. Mass Spectrom. Ion Processes*, **65**, 273 (1985)
- 7) R.K. Boyd, P.A. Bott, J.H. Beynon, D.J. Harven, J.R. Mass, *Int. J. Mass Spectrom. Ion Processes*, **66**, 253 (1970)
- 8) R.G. Cooks, J.H. Beynon, R.M. Caprioli, G.R. Lester, *Metastable Ions*, Elsevier, Amsterdam, 1973.

THE BRITISH LIBRARY DOCUMENT SUPPLY CENTRE

TITLE

Angle Resolved Collision Induced Decomposition
of Gaseous Ions

AUTHOR

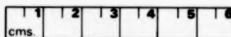
Colin Moore

INSTITUTION
and DATE

University of Warwick 1987

Attention is drawn to the fact that the copyright of
this thesis rests with its author.

This copy of the thesis has been supplied on condition
that anyone who consults it is understood to recognise
that its copyright rests with its author and that no
information derived from it may be published without
the author's prior written consent.



THE BRITISH LIBRARY
DOCUMENT SUPPLY CENTRE
Boston Spa, Wetherby
West Yorkshire
United Kingdom

20

REDUCTION X

CANADA

5

D900072